UNIVERSITY OF CALIFORNIA

Santa Barbara

Chronology and Recurrence of High-Magnitude Debris Flows in the Santa Barbara and Montecito, California Areas

A Thesis submitted in partial satisfaction of the

requirements for the degree Master of Science

in Earth Science

by

Chandler Jean Adamaitis

Committee in charge:

Professor Edward A. Keller, Chair

Professor Kristin Morell

Professor Alex Simms

September 2020

The thesis of Chandler Jean Adamaitis is approved.

_____

Kristin Morell

_____

Alex Simms

_____

Edward A. Keller, Committee Chair

September 2020

Chronology and Recurrence of High-Magnitude Debris Flows in the Santa Barbara and Montecito, California Areas

by

Chandler Jean Adamaitis

ACKNOWLEDGEMENTS

My sincere thanks are extended to the many people whose time, knowledge, and support made this project possible. I owe a lot of gratitude to my advisor, Ed Keller, for introducing me to and guiding me through this project. His wisdom and expertise have pushed me to always stay curious and have helped me become a better researcher and scientist. I would also like to thank my committee member Alex Simms, who graciously allowed me to use his lab to perform radiocarbon processing and provided valuable feedback throughout this process, as well as my committee member Kristin Morell for her helpful discussions on both this project and future careers. Also, I would like to thank the many undergraduate students who helped me with fieldwork; without their help, I would probably still be out there measuring boulders.

I am very grateful for the funding for this research, which came from a fellowship from the Earth Research Institute of UC Santa Barbara, as well as an extremely generous donation from John MacFarlane, a resident of the Montecito community. Additionally, thank you to the many Santa Barbara and Montecito residents for allowing me to come onto their properties to measure boulders.

Lastly, I would like to acknowledge the support and encouragement from my family and friends. To my fellow graduate students, the last two years have generated wonderful friendships and memories that I will carry with me for a lifetime. Thank you for providing a community that balanced work and play. To my officemate and friend, Paul Alessio, thank you for being an ear to my complaints, providing an unending supply of funky jams, and letting me take Bandit on walks when I needed a break. Thank you to my partner, Ryan Reish, who always knows exactly what to say when things get tough. Finally, thank you to my family, particularly my Mom, who has been my biggest supporter since day one.

ABSTRACT

Chronology and Recurrence of High-Magnitude Debris Flows in the Santa Barbara and Montecito, California Areas

by

Chandler Jean Adamaitis

Massive debris flows devastated Montecito, California, USA on January 9th, 2018. The damage from the flows resulted in 23 deaths and greater than $200 million in property damage. Given this destruction, the community fears the possibility of another event. Prior to this study, the recurrence interval of high-magnitude debris flows in the Santa Barbara, California area was unknown despite evidence of them in nearly every canyon. Certainly small to moderate flows following wildfire are common and very large events are rare, but approximately how rare? The evidence of past debris flows occurs as large boulder fields and boulder levees along the banks of the streams that flow out of the canyon mouths and into the city. A major limitation to understanding how often these events happen is the applicability of traditional dating methods. In order to assess the viability of alternative dating methods, data were collected on four different weathering indicators to be used as potential proxies for the time since deposition. These weathering indicators included weathering rind thickness, boulder compressive strength, clast roundness, and clast color. It is hypothesized that the boulders of the debris flow deposits have increased in weathering rind thicknesses, decreased in compressive strength, increased in roundness, and become redder in color with increased weathering time at rates that can be calibrated to numerical ages. To test these hypotheses, the data of each weathering indicator were correlated to a series of numeric ages based on

radiocarbon analyses, soil chronology, ^{21}Ne exposure dating, and incision rates. In the end, although the hypotheses for weathering rind thickness, boulder compressive strength, and clast color were accepted, weathering rind thickness was concluded to be the most successful relative age dating method as it has the highest R^2 value when calibrated to numeric age - a value of 0.80.

The calibrated rate of weathering rind thickness development linked to numerical dates is used to estimate the amount of time since the deposition of boulders through debris flow processes. The equation that estimates the rate of weathering rind development is $t=0.012(w^{3.80})$, where t is the predicted age in thousands of years and w is the mean weathering rind thickness of the boulders within the deposit in millimeters. This analysis served to test the overarching hypothesis for this study that high-magnitude debris flows (on the relative order of magnitude as the 2018 Montecito event) occur once every 1 to 2 thousand years. Results of statistical paired tests and geospatial analyses of the weathering rind data and their respective predicted ages indicate that at least 17 distinct high-magnitude debris flow events are represented in the 30 measured deposits of our study area. These events are estimated to have occurred over the span of the last ~96 ky, indicating a maximum recurrence interval of 5.6 ky. However, since the age control is much better for the younger events, using the last ~9 ky instead, in which there have been at least 5 events, the resulting recurrence interval is ~1.7 ky, confirming the hypothesis that high-magnitude events occur on the order of every 1 to 2 ky. Based on these values, probability estimations suggest that there is approximately a 6% chance of another high-magnitude event happening in the next 100 years. Overall, this study has improved the understanding of the chronology of high-magnitude debris flows and the general understanding of the geomorphic history of the area.

TABLE OF CONTENTS

LIST OF FIGURES & TABLES

Figures

Tables

1. Introduction

1.1 Research Problem

Several high-magnitude debris flows devastated Montecito, California, USA - a town neighboring the larger city of Santa Barbara, California - on January 9th, 2018 (Fig. 1). The damage from these flows resulted in 23 deaths, and damaged or destroyed hundreds of homes and buildings (County of Santa Barbara, 2018b; Fig. 1). A debris flow is a type of mass movement composed of a mixture of water, mud, sediment, and debris such as boulders and trees (USGS, 2016). This mass movement process usually occurs on steep hillslopes after intense precipitation events, particularly if that precipitation event follows a wildfire (USGS, 2016). These flows move through the canyons and channels, further entraining material as they go, moving at speeds that can reach over 40 km/h (25mph). These events can be incredibly destructive when they encounter developed areas, as was seen in the Montecito event (Fig. 1). Additionally, since the wildfire potential appears to be increasing in Southern California as the climate warms and dries, the risk of debris flows is likely to increase and expand in this and similar regions, as wildfire and debris flows are closely linked (Cannon et al., 2008; Santi et al., 2008; Kean et al., 2011; Staley et al., 2014, 2017; McGuire et al., 2017; Addison et al., 2019; Keller et al., 2019, 2020). Given this information and the damage from the 2018 event, the community fears the possibility of another event in the near future. Understanding how events like this happen in the future can be better understood in terms of their behavior in the past.

Prior to this study, the recurrence interval of large-scale debris flows in Santa Barbara, California and the surrounding areas was unknown despite evidence of past flows in

nearly every canyon in the area. This evidence occurs as large boulder fields, as seen in areas like Rocky Nook Park, located near the Santa Barbara Mission, as well as boulder levees along the banks of the streams that flow out of the canyon mouths and into the suburban areas of Santa Barbara and Montecito (Fig. 2). A major limitation to understanding how often these events happen is the applicability of traditional dating methods to deposits such as these. For example, the high erosion rates of mountainous areas can make the residence time of datable material for radiocarbon analysis low and there is a high possibility that the datable material is recycled. Additionally, the application of luminescence techniques is inappropriate due to the limited light exposure of the fine-grained sediment during transport or due to movement at night, which restricts it from being fully bleached prior to deposition – a necessary component for this dating method (McKeever, 2015). However, deciphering the chronology of these events is important because knowledge of the timing of the repeated incidence of these past flows will improve the general understanding of the geomorphic history of the area and potentially improve risk assessment moving forward.

1.2 Research Objectives and Hypotheses

The main objective of this research is to gain a better understanding of the chronology and recurrence of high-magnitude debris flows in Santa Barbara and Montecito, CA and the surrounding areas. Here, high-magnitude is defined as a greater than magnitude-five (M5) event, where magnitude is determined by the volume of the flow on a logarithmic scale (e.g. M5=10^5 m^3 of moved material) (Keaton et al., 1988). This thesis presents the analysis of four different dating methods of boulders in debris flow deposits and explores which is best suited for the purposes of formulating the chronology of these events. Certainly small to moderate flows following wildfire are common and very large events are rare, but approximately how

rare? Our hypothesis is that the recurrence interval of high-magnitude debris flows is on the order of 1-2 ky. This hypothesis is based on the conditional probability (product of two probabilities) of wildfire and intense precipitation events coinciding. For example, if the average return period of a wildfire in the area is assumed to be 25 years (annual probability of p=0.04) and a 75-year rainstorm (intense rainfall over 15–30 min) in the first year following the fire is also assumed (annual probability of p=0.013), then the resulting conditional probability for the first year after the fire is about 0.0005, or a recurrence interval of 2000 years (Mensing et al., 1999; County of Santa Barbara, 2019; Keller et al., 2019). If the required storm is to occur in the first two years following fire, then the conditional probability increases to 0.001, or an average recurrence interval of 1000 years. This estimation is certainly an oversimplification and variable intensity-duration thresholds of both fire and rainfall can initiate debris flows and is a subject of ongoing research, but the estimation gives an idea of the order of magnitude of the recurrence of these high-magnitude debris flows.

The methods employed to test this hypothesis include dating via weathering rind thickness, boulder compressive strength, clast roundness, and clast color. All of these methods are hypothesized to assess the degree of weathering of the boulders within debris flow deposits, which gives an indication of the relative amount of time since deposition (e.g. Colman and Pierce, 1981; Liebens and Schaetzl, 1997; Boelhouwers et al., 1999; Yoshida et al., 2011; Ffoulkes and Harrison, 2014). This practice of dating boulders these ways has been previously referred to as boulder geomorphology (Keller et al., 2019). With increased weathering time, it is hypothesized that boulders of the debris flow deposits will increase in weathering rind thicknesses, decrease in compressive strength, increase in roundness, and be

redder in color. When matched with an independent numeric dating method, empirical best-fit models can be created to quantify and calibrate the rate of weathering development for particular climates and lithologies (e.g. Knuepfer, 1988; Sak et al., 2004; Engel et al., 2016). This calibration tests which weathering indicator varies at a predictable rate and is best suited to assess the age of the events that created the deposits. In doing so, the selected alternative dating method can be used as a strategy to enhance other traditional numeric dating methods or provide age estimates when numeric dating methods cannot be applied. In turn, these methods seek to improve the previously poor understanding of how often these events happen and test the overall hypothesis for this research that the average recurrence interval of high-magnitude debris flows is on the order of 1-2 ky. In doing so, we are able to improve the understanding of the geohazard presented by high-magnitude debris flows in the area and the general geomorphic history of the area.

1.3 Previous Work

1.3.1 Relative Chronology Studies

Previous studies have utilized similar methods to the ones used in this study to assign ages to various geomorphic features not suitable for traditional dating methods such as debris flows or glacial moraines. The most popular of which appears to be the use of weathering rind thickness as an indication of age (e.g. Colman and Pierce, 1981; Knuepfer, 1988; Boelhouwers et al., 1999; Sak et al., 2004; Engel et al., 2016). A weathering rind is an identifiable layer that has undergone more weathering than the material beneath it (Burbank and Anderson, 2012). The thickness of this layer is an indication of the extent of mineral oxidation and reaction below the surface of a clast (Gellatly, 1984). The weathering rind becomes thicker the longer the rock surface is exposed to weathering processes through time,

making it an effective tool for determining the relative age of surficial deposits (Chinn, 1981; Sak et al., 2004). Chemical exchanges and mineral dissolution processes acting on rocks cause the rinds to form, but the extent of the rind thickness is limited by the permeability of the rock and the dissolution reaction rates acting upon it (Reeves and Rothman, 2014). A review study of weathering rind development compiled information on the subject and found that the major influences on weathering rind development are rock type, specifically the grain size and the permeability thereof, and ambient, climatic conditions (Hunt, 2015). Empirical best-fit models can be created by matching thickness to a numeric age to quantify and calibrate the rate of rind thickness development for particular climates and lithologies (Chinn, 1981; Knuepfer, 1988; Ricker et al., 1993; Sak et al., 2004; Oguchi, 2013). In doing so, weathering rinds can be used independently to assign ages to deposits and geomorphic features. Similar methods were applied to the deposits of Santa Barbara, California and the surrounding areas to pilot a more comprehensive understanding of the high-magnitude debris flow event history of the area.

Other studies have implemented the use of the Schmidt Hammer to assess the compressive strength of rocks of varying lithology or weathering state (e.g. Matthews and Shakesby, 1984; Boelhouwers et al., 1999; Duvall et al., 2004; Keller et al., 2015). This is an instrument that measures the rebound of a spring-loaded mass impacting the surface of a sample. The hammer hits the sample at a defined energy and the rebound is dependent on the rock hardness of the sample. As such, the rebound value (R) can be used to determine the compressive strength of the sampled material (Day, 1980). The use of the Schmidt Hammer on varying lithologies provides an attribute to make relative distinctions between compressive strength, which has implications of slope stability and how readily the rock

erodes (i.e. Duvall et al., 2004; Keller et al., 2015). It has also been found that rock strength decreases with increasing weathering time, making it a viable indicator of the relative age of deposits or geomorphic features composed of the same lithology (Matthews and Shakesby, 1984; Boelhouwers et al., 1999).

1.3.2 Numeric Ages of Geomorphic Features within the Santa Barbara, CA Area

Previous to the current study, others have worked toward the goal of assigning numeric ages to various geomorphic features around the Santa Barbara, California area. One such study pertinent to the present one was performed in the Master's work of Best (1989) where he investigated the sediment storage and routing in the steep, bedrock channel of Rattlesnake Creek – a watershed on the south flank of the Santa Ynez Mountains above the city of Santa Barbara, CA. Within this study, he used soil chronosequences and rates of pedogenesis to estimate the age of a debris flow deposit that presently exists as a boulder levee above a well-exposed soil profile along the edge of a channel, and determined it to be 15 to 30 ka (Best, 1989). Soil chronosequence dates are based on calibrated rates of soil development (Bierman and Montgomery, 2014). The thesis work of Urban (2004) also sought to decipher the geomorphic history of the area by investigating the failure of a landslide dam and associated debris flow events. In this process, he used radiocarbon analysis to estimate the age of the debris flow deposit within Rocky Nook Park, near the Santa Barbara Mission. In this work, he concluded that this deposit likely originated from episodic landslide dam failure sometime between 530 and 670 AD (Urban, 2004). Another important study is the work of Landis et al. (2002) where researchers performed a series of six cosmogenic ^{21}Ne exposure dates on the alluvial fan folded over the western portion of the Mission Ridge Anticline (Fig. 3). These dates resulted in estimated ages between 93 and 139

ka (Landis et al., 2002). Though these studies have aimed to assign numeric ages to the geomorphic features of Santa Barbara, California, many gaps in the understanding of the geomorphic history of the area remain, particularly pertaining to the debris flow chronology, and this study aims to fill some of those gaps.

1.3.3 Numeric Ages of Debris Flows

Examples of methods used in attempts at dating debris flows include dendrochronology and lichenometry, radiocarbon analysis, and exposure dating. Studies pertaining to dating via dendrochronology and lichenometry include the works of Hupp et al., 1987; Winchester and Harrison, 1994; and May and Gresswell, 2004. These techniques offer an easily applied, inexpensive method of dating, but are limited to certain settings and the short temporal extent they record, which largely depends on the species used, but is on the order of centuries (Bierman and Montgomery, 2014). Alternatively, charcoal and other carbon-rich material found in the matrix of debris flow deposits can be dated through radiocarbon analysis to estimate the ages of events (e.g. Florsheim et al., 1991; Cabré Cano et al., 2017; Fath et al., 2018). Radiocarbon analyses offer a method to date relatively young to intermediate aged flows; however, these methods are limited by the high erosion rates of the mountainous areas where these deposits are often found, making the residence time of the datable material low. Additionally, due to the relatively short half-life of ^{14}C, this method is not suitable for events older than ~50 ka (Bierman and Montgomery, 2014). Finally, methods using various cosmogenic radionuclides to estimate exposure ages of boulders have been used to date debris flows (e.g. Bierman et al., 1995; Cerling et al., 1999; Dühnforth et al., 2007; Youberg et al., 2014). This type of dating, in its simplest form, estimates the amount of time a clast has been exposed at Earth's surface to cosmic ray bombardment (Bierman, 1994).

This method can be applied to a more extensive range of ages (i.e. 10^3-10^5 years) (Bierman and Montgomery, 2014). These clasts, however, likely have been exposed to cosmic rays before they are entrained and redeposited through debris flow processes, thus accumulating cosmogenic nuclides before deposition, creating issues of inheritance and affecting the apparent age estimation (Bierman et al., 1995). Corrections can be made to limit these effects, but this often requires many samples per boulder (Youberg et al., 2014). Overall, all the aforementioned studies demonstrate the trickiness of dating past debris flows and how each method presents its own strengths and limitations.

1.3.4 Comparing Uplift and Incision Rates

Previous studies have investigated how rates of uplift are comparable to rates of incision and erosion (i.e. Rockwell et al., 1984; Lavé and Avouac, 2001; Pazzaglia and Brandon, 2001; Finnegan et al., 2008; Larsen and Montgomery, 2012; Melosh and Keller, 2013). One such study pertinent to the current study area includes the work of Melosh and Keller (2013). Using the age estimations of the alluvial fan folded over the Mission Ridge Anticline estimated by Landis et al. (2002) in conjunction with the average vertical relief, Melosh and Keller (2013) estimated the minimum uplift rate of western Mission Ridge to be 0.8 +/- 0.1 m/ka. This is a minimum rate because there is no way to constrain the position of the pre-folded alluvial fan relative to the geoid during deposition. In this study they also calculated incision rates by dividing the vertical incision distance by the age of the surface and concluded stream incision ranges from 0.4±0.1 m/ka to 1.2±0.04 m/ka, although structural position and climate change can affect these rates through time. Overall, though, this study concluded that, at steady state conditions, stream incision keeps pace with uplift, assuming constant rates through time (Melosh and Keller, 2013). Other studies have come to

similar conclusions, such as the work of Pazzaglia and Brandon (2001). In this study, they found that, at long time scales (>10-100 ky), bedrock incision rates appear to be a reasonable proxy for rock uplift rates in the Olympic Mountains in northwestern Washington, USA. Additionally, Rockwell et al. (1984), concluded that there is an approximate balance during tectonic deformation between the rate of uplift due to faulting and folding and the rate of downcutting of the fluvial system while researching terraces of the Ventura River in California, USA. This study also used the vertical displacement of a stream terrace to estimate its age using the slip rate of the nearby Arroyo Parida – Santa Ana Fault (Rockwell et al., 1984). These studies provide evidence for the assumption that uplift rates are comparable to incision rates and how that assumption can be further applied.

2. Background

Santa Barbara is located on the coastal plain of California, about 100 km northwest of Los Angeles, on an east-west trending segment of the coastline (Fig. 1). The city is relatively low in elevation (150 to 300 m) with a low to moderate relief piedmont that slopes gently seaward, juxtaposed against the steep Santa Ynez Mountain range to the north. The Santa Ynez Mountains are the westernmost part of the greater Transverse Ranges. The Santa Ynez Mountain range is a topographically rugged, south-dipping anticlinorium that reaches an elevation of about 1400 m (Duvall et al., 2004). Shortening across this western portion of the Transverse Ranges is a result of convergence at an estimated rate of 5 to 20 mm/yr associated with the “Big Bend” of the San Andreas Fault (SCEC, 1995). North-south convergence near Santa Barbara produces east-west reverse faults and folds and this strain drives the tectonic forces creating the Santa Barbara Fold Belt (SBFB). The coastal plain surface contains

several linear mesas and hills that represent geomorphic expressions of potentially active folds and partially buried oblique and reverse faults that transect the area (Fig. 4). The fold belt is bounded to the north by the strike-slip Santa Ynez Fault (Fig. 4).

2.1 Geologic Setting

The south flank of the Santa Ynez Mountains is comprised of locally overturned sandstones and shales of pre-Quaternary strata that record a complex history of transitions to and from deep-water and subaerial depositional environments (Minor et al., 2009; Fig. 3). From oldest to youngest of ages the units are as follows: early to middle Eocene Juncal Formation; middle to late Eocene Matilija Formation; middle to late Eocene Cozy Dell Formation; late Eocene Coldwater Sandstone; Oligocene Sespe Formation; early Miocene Vaqueros Sandstone; early Miocene Rincon Formation; early to late Miocene Monterey Formation; and late Miocene Sisquoc Formation (Dibblee, 1966; Minor et al., 2009; Fig. 3). The differences in resistance to weathering and erosion of these different units produce distinctive topographic expressions of high and low relief.

The Quaternary stratigraphy of the SBFB consists of a sequence of strata originating in both marine and non-marine depositional environments (Minor et al., 2009). These strata can be found on the lower flanks of the Santa Ynez Mountains and underlie much of the low-lying coastal plain area. From oldest to youngest, these units are the early Pleistocene Santa Barbara Formation, middle to late Pleistocene Casitas Formation, and late Pleistocene-Holocene marine terrace deposits, fanglomerate deposits, and other alluvium and colluvium (Dibblee, 1966; Keller and Gurrola, 2000; Minor et al., 2009; Fig. 3). Alluvial fans cover most of the coastal piedmont of Santa Barbara, originating from the south-flowing streams from the Santa Ynez Mountains (Fig. 3). Fanglomerate deposits on these fans are generally

composed of coarse boulders and gravels (Gurrola et al., 2014). More specifically, these fans are the ultimate sink of the high-magnitude debris flows originating from the canyons.

The following section will focus predominantly on the pre-Quaternary Matilija and Coldwater Formations, as well as brief overviews of the formations they are in contact with. These are the likely source regions for the boulders of the debris flow deposits around the areas of Santa Barbara and Montecito.

2.1.1 Juncal Formation

The Juncal Formation is an early to middle Eocene aged unit of shale and sandstone, with shales predominating in the regions around the study area (Fig. 3). The shale layers readily weather into small pieces when exposed to surficial weathering processes and erode to low and recessive relief (Dibblee, 1966; Best, 1989).

2.1.2 Matilija Formation

The sandstone of the middle to late Eocene aged Matilija Formation is described by Stauffer (1967) as rather homogenous, buff colored, massive sandstone with minor interbeds of mudstone. This sandstone is composed of well sorted, sub-rounded, highly feldspathic, and non-micaceous grains (Stauffer, 1967). Grain size ranges from very fine to coarse grained sands, but the average sandstone of this unit is medium grained (Link, 1975). Grains are reported as both textually and chemically mature, indicating that they are a product of considerable abrasion, likely in a shelf area experiencing longshore movement and moving periodically into deeper water by grain flow (Stauffer, 1967). The cause of the flows may have been due to shoaling of the shelf, allowing strong currents to sweep coarse material over the edge of the shelf (Stauffer, 1967). The sandstone beds are hard, well cemented with

calcite, and resistant to weathering, which allows high relief cliffs and steep dipslopes to form and maintain (Best, 1989; Link, 1975). As such, it is this highly resistant to erosion rock that forms the highest part of the Santa Ynez range (Best, 1989).

Best (1989) observed that large boulders weather *in-situ* from exposure along less resistant fracture and bedding planes in the cliffs and enter the channel through rockfall processes. Due to their large size and high resistance to erosion, these boulders are not transported downstream via fluvial processes such as river transport or weathered into smaller particles such that channels within the Matilija Sandstone are clogged with more boulders and bedrock is less frequently exposed compared to canyons underlain by the Coldwater Formation (Best, 1989). Robert Norris (2003) reported that the Matilija Sandstone is the dominant source of the large boulders found around the city of Santa Barbara brought to their present locations through debris flow processes.

2.1.3 Cozy Dell Formation

The middle to late Eocene aged Cozy Dell Formation consists of highly micaceous, well stratified shales. Due to its weak nature, it readily disintegrates into small fragments and forms topographic lows relative to the adjacent areas underlain by stronger Matilija and Coldwater Sandstone units. Strata dip to the south, and due to the preferential erosion of these shales, the more competent sandstone that sits upon it is left as large unsupported strike ridges (Dibblee, 1966).

2.1.4 Coldwater Formation

The Coldwater Formation is the uppermost Eocene unit of the Santa Ynez Mountains, with a loosely constrained middle to late Eocene age. This sandstone is typically pale grey to

greenish grey on fresh surfaces, but weathers to pale shades of buff, yellowish-tan, tan, and brown (Minor et al., 2009). Where cemented and well-lithified, this sandstone creates the prominent ridges and peaks seen at the base of the south side of the Santa Ynez Mountains (Gurrola, 2006). This sandstone is fine to coarse-grained, well-sorted, non-micaceous, feldspathic and partly-arkosic, and weakly lithified with calcium carbonate (Stauffer, 1967; Minor et al., 2009). In the upper and middle sections of this formation, sparse to abundant mollusks shells can be found, generally culminating as beds of oyster shells, indicating a shallow marine depositional environment (Stauffer, 1967). The fossiliferous beds are predominantly in the transition zone between the Coldwater and Sespe Formations. Although these beds are hard, they are calcareous and more readily weather by solutional processes (Best, 1989).

2.1.5 Sespe Formation

The Sespe Formation is a non-marine, Oligocene-aged interbedded shale and sandstone formation that readily erodes to form low relief areas (Minor et al., 2009). The Sespe's most distinguishing feature is its prominent red color. The lower part of the formation is a 30 m thick, generally coarse bed of basal sandy conglomerate and pebbly arkosic sandstone. This conglomerate grades upwards to a series of interbedded coarse and fine-grained red sandstone, with some silty shale beds. The upper part of the formation is predominantly thick shale beds. These shales are compact, but still readily disintegrate into smaller pieces, forming low-relief hillslopes mantled with Pleistocene boulder gravels (Minor et al., 2009).

2.2 Tectonic Setting

The dominant source of seismicity on the coastal piedmont of the Santa Barbara-Montecito, CA area is the 70km long, south-dipping, reverse Mission Ridge Fault System (Keller and Gurrola, 2000; Fig. 4). This fault system creates prominent and extensive topographically expressed folds. The Mission Ridge Fault System has been segmented based on unique geometric, geomorphic, and structural characteristics. The three main segments of the Mission Ridge Fault system are the More Ranch, Mission Ridge, and Arroyo Parida segments (Keller and Gurrola, 2000; Fig. 4). The segments are dominantly south-side up, partially blind, reverse fault segments and anticlinal uplifts that deform units as young as the late Pleistocene (Minor et al., 2009). The resulting surface expression of this deformation is subtle in some places and dramatic in others. Growing anticlines are uplifted in response to reverse faulting and create the linear hills and sea cliffs found in the area. In contrast, low-lying areas characterized by subsidence are faulted synclines and create the salt marshes and sloughs of the area (Gurrola et al., 2014; Simms et al., 2016). This section will mainly focus on the Mission Ridge segment, which dominantly passes through the study area.

The Mission Ridge segment strikes through the community of Santa Barbara and dips south beneath the urban region of the coastal piedmont (Fig. 4). The Mission Ridge Anticlinal fold extends westward from Montecito to Santa Barbara for most of the fault segment's 17km length (Fig. 4). The anticline varies in elevation from 25m to 200m on its most westward end with about 100m of relief (Keller and Gurrola, 2000; Minor et al., 2009). The anticline uplifts and folds late Pleistocene alluvial deposits and fanglomerates and pre-Quaternary strata (Fig. 3). Various outcrops and investigations of the deposits of Mission Ridge suggest that it is a hanging-wall anticlinal fold (Keller and Gurrola, 2000). The highest

areas of this ridge sit approximately 2 km north of downtown Santa Barbara. Commonly anticlines occur as elongate ridges or hills and synclines appear as valleys or swales. In the case of this area, the western portion of Mission Ridge is coincident with an anticline and is paired with a syncline along its north side that produces a roughly linear valley.

Based on geomorphic evidence, it has been inferred that the anticline has propagated west due to westward propagation of a blind strand of the Mission Ridge fault segment (Keller et al., 1999; Keller and DeVecchio, 2013). This propagation has resulted in a continued westward deflection of Mission Creek (Keller et al., 1999; Keller and DeVecchio, 2013). Evidence for this lateral propagation includes the presence of wind gaps on the western side of Mission Ridge where uplift was greater than incision, resulting in Mission Creek abandoning its channel and diverting farther west to its present location.

2.3 Climate

The present climate of Santa Barbara is Mediterranean, characterized by warm, dry summers and cool, wet winters (County of Santa Barbara, 2018a). The proximity to the Pacific Ocean helps induce a moderation in temperature; however, the proximity to the steep mountain ranges produces a significant orographic effect (County of Santa Barbara, 2018a). Storms approaching the coastal plain from the ocean are rapidly forced upward, occasionally resulting in short duration, high-intensity rainfall events. As a result, in conjunction with short, steep watersheds of the Santa Ynez Mountains, episodic, torrential discharges in the region's streams and rivers can occur, sometimes leading to flash flooding (Warrick et al., 2004). However, the rivers and streams of the area remain at low flow to dry conditions for most of the year (Warrick and Mertes, 2009). Average annual precipitation in the downtown

area is 47 cm, but, historically, it has ranged from 16 to 119 cm; however, rainfall at the crest of mountains can be several times that of the city (County of Santa Barbara, 2018a).

Over the time period of interest for this study (last ~100 ky), the local climate has fluctuated with glacial-interglacial cycles. During interglacial periods, like now, the climate was predominantly warm and arid; during interglacial periods, the climate was comparatively cooler and less arid (Heusser, 1995; Behl and Kennett, 1996).

2.4 Vegetation

Presently, chaparral is the dominant vegetation type found on the Santa Barbara coastal plain and throughout the canyons (Dennison and Roberts, 2003). This type of vegetation is supported by a Mediterranean climate and is composed of a combination of species such as oak, ceanothus, purple sage, and manzanita plants (Mensing, 1998; Dennison and Roberts, 2003). In the past 100 ky, the dominant vegetation type has changed with the regional climatic variations. Pollen assemblage within glacial-aged sediments indicate that the vegetation was mainly dominated by coniferous taxa, while interglacial sediments show dominance of coastal oak woodland, chaparral, and coast sage scrub (Heusser, 1995; Mensing, 2015).

2.5 Wildfire

Wildfires are a natural phenomenon in the California chaparral environment. The main mechanism for natural wildfire ignition is lightning; however, anthropogenic interactions greatly exacerbate fire likelihood (Lavé and Burbank, 2004). Although it remains a topic of continued debate and the impacts of climate change will potentially increase the recurrence, scholars report the average recurrence interval of large wildfires of this area to be

20 to 100+ years (Florsheim et al., 1991; Mensing et al., 1999; Ejarque et al., 2015). These fires typically happen at the end of the wet season and the beginning of droughts. The immediate effects of wildfire are increased runoff and sediment supply because the vegetation that previously stabilized the slopes has been removed (Florsheim et al., 1991). Post-wildfire debris flows demonstrate that wildfire and debris flows are intimately linked by intense precipitation. This relationship is such that when wildfire followed by intense precipitation occurs, extensive rilling on hillslopes produces mud that coalesces in boulder-rich channels, creating debris and mud flows, and then further precipitation after flows can flush even more sediment (Keller et al., 2019).

3. Methods

Approximately 50km^2 of the coastal plain, with an elevation change of about 200m, around the Santa Barbara and Montecito, CA areas were traversed to identify deposits of past debris flows (see Fig. 1 for specific study area). These deposits appear as boulder fields, levees, and noses (terminus of debris flow lobe) (Fig. 2). At each deposit site, data pertaining to the boulder geomorphology - weathering rind thickness, rock compressive strength, clast roundness, and boulder surface color - were collected. Each of these metrics gives an indication of the degree of weathering the boulder has undergone, therefore the amount of time it has undergone weathering processes. Due to the boulders of the 2018 Montecito flow deposits having dominantly fresh, unweathered surfaces, we assume that the movement down the canyon in the debris flow process removes the outer layers that record previous weathering. This fresh surface minimizes the effects of inherited weathering features, which

permits the measurement of the various weathering features to be considered a proxy for the amount of time since the last distal movement of the boulder.

The major influences of weathering development are rock type, specifically the grain size and the permeability thereof, and ambient, climatic conditions (Hunt, 2015). Robert Norris (2003) reported that the Matilija Sandstone is the dominant source of the large boulders found around the city of Santa Barbara, brought to their present locations by debris flow processes. As such, it is assumed that all the measured boulders are similar in origin and composition; however, in-depth grain size and lithologic analyses were not performed for this study. Additionally, since the study area is restricted to a relatively small area, it is assumed that the same overall Mediterranean climatic conditions are presently acting upon the different deposits. The potential effects of microclimate (moisture levels, nearby vegetation density, aspect, etc.) were not assessed. Additionally, through time, the older deposits will have experienced more phases of climate change than the younger ones, but overall, climate conditions throughout time have affected all the represented deposits at that time. For example, the oldest debris flow deposits (100ka) all went through the same cycles of climate (2 glacial and 3 interglacial periods), as did the intermediate deposits (1 glacial and 2 interglacial), and the youngest deposits all only went through 1 interglacial. With this information, it was assumed that the climatic and lithologic factors are uniform throughout the study area, which helps provide constraints to reduce any further variables that could influence differences in weathering development between deposits besides time and makes the comparison of the different sites more feasible.

All measurements were made on the same set of boulders at any given site. At each site, a sample set of up to twenty boulders was measured. Care was taken in sampling to

avoid boulders with obvious signs of recent disturbance or non-natural movement (i.e. for building or development purposes). Additionally, sampling was biased toward measurements on larger boulders (>1m on the intermediate axis) to assure that other processes, such as river transport, were not responsible for the transportation to their measured location.

Where possible, datable material was collected to establish a numeric age for that site. Readily available datable material was scarce though, which resulted in targeting sites close to road cuts and outcrops.

Sampling was repeated at site 4 to ensure measurement methods had not changed or become skewed over the two years that data were collected.

3.1 Weathering Rind Measurements

In order to test the hypothesis that weathering rind thickness can be calibrated to numeric age and increase in thickness at a predictable rate as clasts weather, two measuring methods were employed. The predominant method of collecting weathering rind thicknesses was carried out by measuring along the edge of an intact piece of weathering rind, adjacent to where a piece of rind had flaked off, exposing the fresh, non-weathered rock beneath. This measurement was made using digital calipers with a precision of 0.01 mm to the top of the parent rock, normal to the boulder surface (Fig. 5A). In some cases, the boulder was cracked in such a way that the weathering rind thickness was measured using the color contrast between weathered and unweathered rock. In this case, the prominent red color due to the increased concentration of immobile oxides relative to the unweathered parent rock depicts the thickness to be measured (Fig. 5B). At each site, twenty thickness measurements per boulder were made.

3.2 Compressive Rock Strength

Compressive strength of the debris flow boulders was measured using a Schmidt Hammer to test the hypothesis that rock hardness can be calibrated to numeric age and decreases with increasing weathering time. The Schmidt Hammer is an instrument that measures the rebound of a spring-loaded mass impacting the surface of a sample. The hammer hits the sample at a defined energy and the rebound is dependent on the rock hardness of the sample. As such, the rebound value (R) can be used to determine the material's compressive strength (Day, 1980). Twenty Schmidt Hammer measurements were taken per measured boulder at each site. Each measurement, where possible, was taken on intact, relatively flat surfaces around the surface of the boulder.

3.3 Roundness

Preliminary field assessment of the boulders of the 2018 Montecito event indicated that they were very angular and the boulders of deposits presumed to be much older were rounder in shape. These observations led to the hypothesis that the boulders become increasingly rounder as they weather and, therefore, roundness can be calibrated to numeric age. To test this hypothesis, roundness was estimated by comparing each boulder at a given site to the Krumbein (1941) roundness chart (see Appendix Fig. A1 for chart). This chart assigns a value between 0 and 1 based on the relative roundness of clasts, 0 being extremely angular and 1 being extremely rounded. A single roundness value was assigned to each measured boulder at every site.

3.4 Color Index

Based on preliminary field observations, I hypothesized that the boulders of the debris flow sites become progressively more red on the outer layers of the clasts as they undergo weathering through time. This observation suggested that color could be a potential metric to assign relative age. In support of this hypothesis, Colman (1981) found that immobile oxides, such as Fe_3O_2, are often concentrated on the outer layers relative to the core as weathering penetrates deeper into the core of the clast through time. To test this hypothesis, color was measured by comparison with Munsell Soil Color charts. Charts were held against the boulder surface to find the closest color match of the distinguishing features of the boulder. A single hue, chroma, and value were assigned to each boulder that was representative of its overall weathered state. This process was repeated for every boulder on which other measurements were taken.

The Hurst Index was used to convert the signified color from the Munsell Chart into a single number to better compare the colors between boulders and sites (Hurst, 1977). The Munsell chart uses a number and capital letters to signify hue, a separate number for chroma, and another number for value. The Hurt Index quantifies the hue (i.e. 10R=10, 5YR=15, 7.5YR=17.5, 10YR=20, 5Y=25), and multiplies it by the value/chroma fraction. As such, a lower number indicates a redder surface. Originally this number was intended to be used as a crude proxy for the total amount of iron in a soil, therefore its degree of weathering. For our purposes, it was similarly used as an indication of the extent of weathering the boulders have undergone through time.

3.5 Numeric Age Controls

Numeric age controls for this study come from four different dating methods, performed both in this study and in previous ones. The first method used was radiocarbon analysis of charcoal inclusions within the debris flow deposits. This form of numeric dating was only attempted for deposits assumed to be young to intermediate in age (<50ka). Because wildfire and debris flows are closely coupled, I assumed that the charcoal within the fine-grained matrix of the flow deposits originates from a wildfire event close enough in time to the debris flow to accurately approximate the age of the event (Kean et al., 2011). However, due to the possibility of recycling of previous wildfire material, the ages represent a maximum potential age.

Charcoal samples were collected at two field locations. To limit modern contamination, these samples were collected by first excavating 10-15 cm into the unconsolidated matrix surrounding the boulders. A bulk sample of material was collected from behind this cleared material. The bulk sample was sieved using a set of sieves with openings of 2000 μm, 500 μm, 250 μm, 125 μm, and 63 μm to remove any pebbles or silt and very fine sized particles to isolate the charcoal from the sediment. Stainless steel forceps were used to extract any charcoal pieces found in the remaining material. These samples were sent to the DirectAMS laboratory in Bothell, WA, USA for radiocarbon analysis. There, prior to analysis using an accelerator mass spectrometer, they underwent a chemical pretreatment protocol to remove any adsorbed carbon compounds that could alter the apparent age. Radiocarbon ages collected during this study were calibrated using the Calib program v7.1 (Stuiver and Reimer, 1993; Stuiver et al., 2017) with the IntCal13 curve (Reimer et al., 2013). Collection, analysis, and calibration methods, as well as sample site

descriptions of the radiocarbon analysis for the age from a previous study, can be found in Urban's (2004) thesis.

Two numeric ages came from previously published work on two deposits with intermediate to older ages (>20ka). These dates are from soil chronosequences and rates of pedogenesis and cosmogenic radionuclides (Best, 1989; Landis et al., 2002). The soil chronosequence estimates the age of a debris flow deposit that presently exists as a boulder levee above a well exposed soil profile along the edge of the channel (Best, 1989). The cosmogenic radionuclide dates provide an age estimation for a large alluvial fan that is presently folded over the Mission Ridge Anticline (Landis et al., 2002; Fig. 3). Further site descriptions and sample collection, analysis, and calibration methods can be found in the body of these works.

Ages of deposits assumed to be from events that occurred a few ka to 100 ka were estimated using site elevations relative to the elevation of the channel bottom (relief) using an appropriate incision rate. Assigning age based on an incision rate is based on the assumption that, at steady state conditions and assuming constant rates through time, the uplift rate is equal to the incision rate (Melosh and Keller, 2013). Therefore, if the uplift rate is known, the age of the debris flow deposit site surface can be back calculated using the depth of incision. A minimum uplift rate for the western portion of Mission Ridge was estimated to be 0.8 +/- 0.1 m/ky based on the age of an alluvial fan folded over the anticline and the relief of that anticline (Landis et al., 2002; Melosh and Keller, 2013), and it is this rate that was used to estimate the deposit ages for this study. These methods are similar to how Rockwell et al. (1984) used the slip rate of a nearby fault to estimate the age of a stream terrace using its vertical displacement. Relative elevations were estimated using a 2018 LiDAR dataset of the

area (DOC/NOAA/NOS/OCM, 2018); an average of three to five relative elevations near the site surface was used to estimate the amount of incision.

Estimation of numeric ages using incision rates was incorporated due to the other methods only providing five numeric ages. The ages provided by incision rates contribute a larger and more continuous data set of numeric age, however, it must be addressed that these only provide rough estimates. For example, larger flow depths that create higher terraces would presumably give older apparent ages as the surface will be relatively higher, insinuating more incision than actually occurred. However, the flow depths are not so variable that this limitation would skew or overwhelm the results of the ages. For example, the depth of the flow deposits from the 2018 Montecito were estimated to be up to 5 m along San Ysidro Creek based on DEM to DEM (digital elevation model) differencing of Lidar-derived topography datasets collected in 2015 and 2018 (Keller et al., 2019). Additionally, (Kean et al., 2019) estimated the average peak flow depths throughout all the affected channels during the 2018 event to be between 3 and 5 m. This range in depth would only create a 2 to 3 ky difference in the apparent age if dated by incision rates. Additionally, this experimental dating method appears to function well enough such that when it is compared to the calibration curve of the ages obtained solely via radiocarbon analysis, soil chronosequence, and cosmogenic radionuclide exposure dating, they largely coincide. See Appendix Fig. A2 for the chart that compares these calibration curves.

The ages received from each of these numeric dating methods were correlated with the average of each of the four weathering indicators of the respective debris flow deposit sites to assess which indicator varied the most succinctly with time.

3.6 Geospatial Data

Locations of each measured boulder were taken using a Trimble Geo 7X handheld device with sub-meter accuracy. The device was placed on each boulder for at least 60 seconds before being moved to the next location. These data were plotted on a hillshade relief map created from a 2018 airborne LiDAR bare-earth DEM of the Santa Barbara coastal plain (DOC/NOAA/NOS/OCM, 2018).

3.7 Statistical Analyses

Five different statistical metrics were applied to the data sets. First, all the data from the four relative dating methods per site were compiled and frequency histograms of each data set were plotted for preliminary visual identification of their distributions. Normality was tested using one-sample Kolmogorov-Smirnov (K-S) tests. These exploratory methods helped indicate that a parametric paired test was better suited for the data than nonparametric as was used in the study of Boelhouwers et al. (1999).

Two methods were used to better assess the trends of how the different sites grouped together. Preliminary assessments were made using the Jenks Natural Breaks algorithm to better identify the overall trends in the data. This algorithm separates data into groups such that it minimizes the deviation from the class mean within a group while maximizing the deviation from the means of the other groups (North, 2009). Further statistical analyses using Student's t paired tests were performed to analyze the relationships between the weathering rind thickness data between sites in more detail. This test compares the means of two data sets with normal distributions and assesses whether their means differ significantly. A probability value (p-value) of greater than 0.05 provides strong evidence to accept the null hypothesis that the two sites' data are from the same population (Gauthier and Hawley,

2007). In order to ensure sampling methods had not changed in the two years of data collection, sampling was repeated at site 4 and a paired test was performed. The second round of data collection at this site is indicated as site 7 (Table 1; Fig. 6).

In order to assess which of the measured weathering metrics best correlated with time, the numeric ages were plotted against the respective average of each of the four indicators of the degree of weathering for those sites. This regression analysis indicated which attribute had the highest R^2 value, therefore, which attribute was best suited to assign ages. That is, we interpret the highest R^2 value to be the attribute that most succinctly represents the amount of time that the boulders have undergone weathering in their present location, and therefore the time since deposition. Multiple regression analysis was also attempted but ultimately not pursued – this is further addressed in the Discussion section.

3.8 Recurrence Interval and Future Event Probability Estimations

The recurrence interval was estimated using the number of events that happened in the past in a given time period. The sites deemed to be statistically similar to one another were subdivided by their geographic location to indicate the number of individual events. For example, if two sites have been deemed to have statistically similar weathering rind thicknesses, but are located in two separate canyons, they were counted as two distinct events. In contrast, if two or more sites are located in the same canyon and are statistically similar, they were counted as a single event. Then, using the predicted ages of these events, recurrence intervals were calculated.

The probability of another event happening in the future can be estimated using recurrence intervals and statistical probability equations. One of the models the United States Geological Survey uses, and the one used in this study, is the Poisson Model. This model was

constructed to estimate the probability of future landslide events but it was concluded that it is applicable to other mass movements and natural hazards (Crovelli, 2000). In this model, the probability of one or more landslides during a specified time period is estimated with the equation: $P\{N(t) > 1\} = 1\text{-}e^{(-t/\lambda)}$, where P is the probability, t is the time interval of interest, and λ is the recurrence interval (Crovelli, 2000). This equation was used to estimate the percent chance of another high-magnitude flow happening over different future time intervals.

4. Results

In total, 30 debris flow deposits were sampled (Table 1). The weathering rind thickness is the weathering indicator most highly correlated to age (Table 2), suggesting it varies at the most predictable rate. The R^2 value for numeric age and weathering rind thickness is highest at 0.80, followed by age and color at 0.70, age and Schmidt hammer rebound values at 0.56, and finally, age and roundness is 0.11. Further distinction is found using the coefficient of variation (CV), which is the standard deviation divided by the mean. This statistic helps compare the spread of data sets that have different units of measurement. In this instance, the average CV is 20.2% for the weathering rind thickness data, 22.9% for the Schmidt hammer rebound values, 9.1% for the roundness values, and 30.6% for the color index values. Despite the low CV for the roundness values, there is little to no substantial change from site to site, making it difficult to decipher relative distinctions. The Schmidt Hammer and color index values have a relatively large spread in the data within sites and high degrees of overlap between sites, seen in the respective box plots and histograms of the data from each dating method (Fig. 7A-7D & 8A-8D). As such, weathering rind thickness

has been deemed the best-suited method to assign relative ages, and therefore, more in depth analysis was proceeded with this dating method than the others. Raw data of all attempted dating methods and coordinates of each measured boulder can be found in the Appendix (Table A2).

4.1 Weathering Rind Thickness

Upon compiling the weathering rind thickness measurements, frequency histograms indicate unimodal, predominantly normal distributions for each measured site (Fig. 8A). Results of the K-S normality test also indicate a majority of the sites have normally distributed weathering rind data (Table 3). Preliminary assessment using the Jenks Natural Breaks algorithm broke the weathering rind thickness measurements into three subgroups, from here referred to as relatively thin, intermediate, and thick. The site numbers for these subgroups are sites 1 to 9, 10 to 23, and 24 to 30, respectively, and represent debris flow deposits of relatively young, intermediate, and old ages. The thin weathering rind subgroup site means range in average thickness from 4.156 mm to 5.673 mm (4.619 mm subgroup average), intermediate range from 6.677 mm to 8.434 mm (7.546 mm subgroup average), and thick range from 9.139 mm to 10.761 mm (9.824 mm subgroup average) (Table 1). Figure 6 shows the locations of the sites and their respective subgroup based on the weathering rind thickness class. This figure illustrates how sites of similar rind thickness, and therefore age, can be traced throughout the canyons.

When compared to the numeric age of the respective deposit, the weathering rind thicknesses data show that they increase at a predictable rate. The 0.80 R^2 value between weathering rind thickness and numeric age illustrates that the correlation between these two variables is relatively strong. This strong correlation confirms the hypothesis that weathering

rind thickness increases at a predictable rate as clasts undergo weathering processes. Since weathering rind thickness had the strongest correlation to age, weathering rind thickness was the weathering indicator that was calibrated to numeric age and used for continued analysis.

4.2 Schmidt Hammer Rebound Values

Despite the Schmidt Hammer malfunctioning in the field, 26 of the 30 sites were measured for rock compressive strength. Of the data collected, frequency histograms indicate predominately unimodal, non-normal distributions (Fig. 8B). Using the same subgroup separations as the weathering rind thickness groups, the range of average rebound values for the sites deemed to be of younger, intermediate, and older ages are 31.5 to 40.4 (35.8 subgroup average), 25.8 to 35.5 (30.8 subgroup average), and 23.6 to 31.6 (27.1 subgroup average) (Table 1). These averages indicate that the overall trend is of decreasing rebound values with increasing weathering time.

Graphically, an overall trend of decreasing rebound value with increasing site number was observed (Fig. 7B); however, it is not very pronounced. This trend is further illustrated when rebound values are plotted against weathering rind thickness (Fig. 9A). In this instance, weathering rind thickness can be considered the proxy for time and the negative slope for the trend line of the data indicates compressive strength decreasing with increased weathering time. However, the R^2 value of 0.22 indicates that this correlation between weathering rind thickness and compressive strength is relatively weak (Fig. 9).

The viability of calibrating compressive strength to numerical age to use it as an independent chronometer is moderately strong as reported with the R^2 value of 0.56 (Table 2). This R^2 value, along with the graphical evidence, indicates that compressive strength doubtlessly decreases with increased weathering time, confirming the original hypothesis, but

the high variability within a given site makes it less practical of a method to independently assign ages to debris flow deposits by calibrating it to numeric age.

4.3 Roundness Values

Very little difference was observed in the roundness values among the 30 sites. Using the same subgroup separations as the weathering rind thickness groups, the range of average roundness values for the sites deemed to be of younger, intermediate, and older ages are 0.500 to 0.583 (0.547 subgroup average), 0.405 to 0.585 (0.542 subgroup average), and 0.450 to 0.604 (0.528 subgroup average), respectively (Table 1). The average roundness for each of these groups overlaps. These data demonstrate a trend of very little variability in the roundness values between each site and their respective subgroup.

To further illustrate this idea graphically, the box plots and frequency diagrams of the roundness values show little variation from site to site (Fig. 7C and 8C). Additionally, the average weathering rind thickness was plotted against the assigned roundness value for each measured boulder (Fig. 9B). Again, rind thickness is representing weathering time. The nearly flat trend line and very low R^2 value of 0.013 indicates that there is nearly no correlation between the roundness values and weathering rind thickness.

In addition to the low R^2 value of 0.11 between numeric age and roundness (Table 2), these data provide further evidence that roundness of boulders does not change in a predictable manner with respect to weathering time. As such, the original hypothesis that the roundness value would increase with increased weathering time and could be calibrated to numeric age is rejected and roundness was deemed an ineffective tool to distinguish the age of debris flow deposits.

4.4 Color

Using the subgroup separations, the range of average color index values for the sites deemed to be of younger, intermediate, and older ages are 87.9 to 169.3 (120.2 subgroup average), 71.3 to 109.7 (91.7 subgroup average), and 66.3 to 93.3 (79.0 subgroup average), respectively (Table 1). These data indicate that the color index value is decreasing, therefore the boulders are becoming redder, from site to site.

Graphically, however, this trend of decreasing color index is shown to be less pronounced. The frequency diagrams of the color indices of the boulders for each site have no apparent distinctive distribution and, in many instances, are highly spread (Fig. 8D). The box plots for each site do show an overall decrease in color index as site number increases, but the large spread of the data for each site overwhelms the trend (Fig. 7D). Additionally, when the color index is correlated to the average weathering rind thickness measurement for each measured boulder, an overall trend of decreasing index, indicating increasing redness, with increased rind thickness appears; however, the correlation is relatively weak, as indicated by an R^2 value of 0.15 (Fig. 9C).

Overall, the R^2 value of numeric age and color index of 0.70 confirms the original hypothesis that the clasts generally become redder with increased weathering time (Table 2). However, although this is a high R^2, there is a large spread in the data, making it a less effective tool to be calibrated to numeric age and independently assign ages to debris flow deposits.

4.5 Numeric Ages

The compiled numeric ages of the debris flows studied range from the historic event in 2018 to about 116 ka (Table 4). These estimates include one historic age, one soil

chronosequence (site 17), one exposure age (site 30), three radiocarbon ages (sites 2-4), and eighteen ages based on incision rate (sites 1, 5-9, 10, 12, 15, 18-22, 24, 26, 27, 29) (Table 4; Fig. 6). Uncalibrated radiocarbon ages can be found in the Appendix (Table A1).

4.6 Calibration Curve and Predicted Ages

Weathering rind thickness had the highest R^2 value when correlated to numeric age, therefore, it is this calibrated weathering indicator that was used to predict ages. Previous studies (Chinn, 1981; Knuepfer, 1988; Hunt, 2015), have shown the relationship between weathering rind thickness development and time are best represented with a power function. The results presented in this study are consistent with that idea. Upon correlating the numeric ages to the respective mean weathering rind thickness for those sites (Fig. 10), the equation that estimates the rate of weathering rind development is $t=0.012(w^{3.80})$, where t is the predicted age in thousands of years and w is the mean weathering rind thickness in millimeters. When the mean weathering rind thickness for each site was input into this equation, the resulting 30 predicted ages ranged from the present to ~96 ka. However, since this is a power law equation, sites with larger weathering rind thickness, therefore older age, have larger variability in their predicted age, making the equation better suited for predicting ages of young to intermediated aged events. Figure 11 shows all 30 of those predicted ages and their respective error ranges graphically; Table 5 indicates the predicted age and the respective possible age range. Figure 12 shows how well the predicted ages correspond to the respective numeric age. If the numeric ages were predicted perfectly to their respective numeric age, the regression line for this correlation would fall on the y=x line. However, the regression line below the y=x line indicates that the predicted values are systematically lower

than their actual numeric ages. Nonetheless, the R^2 value of 0.82 between predicted age and numeric age provides further evidence that there is a coherent relationship between the two.

4.7 Paired Tests

Student's t paired tests were only performed on the weathering rind data as they most highly correlated with age. K-S tests indicate that the weathering rind thickness data are of predominantly normal distributions, allowing for the parametric paired test to be used (Table 3). Table 6 indicates whether the null hypothesis that the data are from each pair of sites has means that are statistically similar is rejected or accepted. To accept the null hypothesis signifies that the data for the two sites are from the same population, in other words, of being the result of similarly aged events. The paired test offers a way to group sites together with more detail and precision than was done with the Jenks Natural Breaks algorithm method. The paired test of the repeated sampling at site 4 indicated that the data from the two sampling occasions that occurred about two years apart are statistically similar, implying that the measurement methods were consistent throughout the study time– the repeated sampling has been labeled as site 7 (Table 1; Fig. 6). The following section indicates the results of further analysis using the results of these paired tests.

4.8 Recurrence Interval and Probability of Future Events

Results of the combined statistical and geospatial analysis of the weathering rind thickness data indicate that, including the Montecito 2018 event, there are at least 17 high-magnitude debris flow events represented in the studied area. These distinct events are distinguishable on the map of Figure 13, and Table 5 indicates which site numbers belong to the distinct events. This number of distinct events indicates that, over the entire proposed

range of predicted ages of approximately 96 ky, a high-magnitude debris flow has occurred at least once every 5.6 ky, on average. However, since the age control is much better for the younger events as the margin of error is smaller, if we instead use the last 8 to 9 ky, in which there has been at least 5 events, the average recurrence interval is 1.7 ky. Though, it must be acknowledged that due to the resolution of our measurement methods, this is a minimum number of events, therefore maximum recurrence interval.

Upon deciphering the average recurrence intervals of high-magnitude debris flows within the study area, further estimation can be made. With this recurrence interval of 1.7 ky, the Poisson Model estimates the probability of another event happening in this study area in the next 100 years is 5.78%. Table 7 gives more estimates of the percent chance of another high-magnitude flow happening over different future time intervals.

5. Discussion

5.1 Sources of Error in Field Measurements

A potential sources of error that could have affected the results of the field measurements arises from the possibility of non-uniform boulder lithology. Although the predominant rock type of the boulders is likely Matilija Sandstone, some fossiliferous boulders have been seen in the field, indicating Coldwater Sandstone compositions are represented in the debris flow sites. The mud source of the debris flows is likely from the Juncal Formation shale (Paul Alessio, University of California Santa Barbara, personal communication, 2020; Fig. 3), therefore, during debris flow initiation, the mud picks up boulders from the Matilija Sandstone unit below and then further passes through areas

underlain by the Coldwater Sandstone. Despite both units being sandstones, this mixture of lithologies likely had an effect on the assessment of the weathering behavior of the measured boulders. However, without the fossils (which is also possible for Coldwater Sandstone boulders), it is extremely difficult to distinguish between the two sandstones without doing an in-depth grain size or geochemical analysis, which are outside the scope of this study, making it nearly impossible to say to what extent this mixture of lithology affected the results. Future research could further explore to what extent the difference in rock types affects the rate of weathering rind development.

Another potential source of error that may bias the development of the weathering indicators comes from the differences in microclimate amongst the different deposit sites. Microclimate includes facets such as aspect, local vegetation, proximity to water sources and moisture conditions, shade, etc. These attributes likely differ between sites and even between boulders and have effects on the rate of weathering thereof. Future research could use these attributes to investigate the influencing factors on weathering rind development with higher detail.

5.1.1 Decreased Rind Development through Time

Variability in weathering rind thickness potentially arises from a change in apparent weathering rate through time. As seen in the graph illustrating predicted age vs weathering rind thickness (Fig. 11), the rate of rind development decreases through time. Similar to this study, several other studies have found there is a power law relationship between weathering rind thickness of clasts and the age of those clasts (Chinn, 1981; Knuepfer, 1988; Hunt, 2015). Gordon and Dorn (2005) suggest that the reduced humidity levels within the deeper parts of a clast could result in a decreased weathering penetration depth, thereby decreasing

the weathering rind development through time. An alternative hypothesis from that study is that weathering rind development may still progress into the rock but simultaneous microerosions are occurring on the outermost parts of the rinds such that the apparent thickness is lower than it would be otherwise (Gordon and Dorn, 2005). As such, for this study in particular, the implications of these findings suggest that the sites with thinner rinds, therefore younger, have better defined ages than those with the intermediate and thicker rinds as the margin of error is much smaller for the younger deposits.

Another source of error for the weathering rind thickness data stems from the field method of measurement. Other studies that used weathering rind thickness as a proxy for time since deposition have used cores of the studied clasts or have split open the entire clast to decipher thickness, sometimes in conjunction with laboratory methods such as electron microscopy and x-ray diffraction (Sak et al., 2004; Yoshida et al., 2011; Dorn and Jeong, 2018). For our purposes, we wanted to explore methods of measurement that were quick and readily applied in the field, with little disturbance to the deposits themselves. Unfortunately, with this type of efficiency comes limitations of accuracy and precision. Measuring along the edge of weathering rinds adjacent to where spalling has occurred could be underrepresenting the total weathering rind thickness on any given boulder. Since there is no way to definitively say when the rind separated from the clast and exposed the new surface, the weathering front could be below where it was deemed a "fresh surface." In the field, this issue was exemplified on a small fraction of the boulders where it was observed that multiple weathering rinds were inset within each other (see Fig. 14 for example). In an effort to diminish the effect of these potential sources of error, thickness measurements were taken primarily along the less rounded edges, as this gives a relative indication that the weathering

rind edge has not been exposed to erosional processes, implying it has more recently broken off. In the instance of embedded rinds, a composite measurement was taken to account for the total weathering rind thickness. Additionally, we used a high number of measurements, up to 400 in any given site, to better ensure the average would largely outweigh these effects. However, despite these attempts to limit the associated error of in-field measurement, it is likely that the methods used in this study systematically underestimate the weathering rind thickness on any given clast.

5.1.2 Reliability of Schmidt Hammer Data

In contrast to this study, previous studies that utilized similar methods have found the use of Schmidt Hammer tests to be a better indication of relative age than weathering rind thickness. Boelhouwers et al. (1999) found that Schmidt Hammer tests of the compressive strength of debris flow deposit boulders were a less biased, more consistent approach to deciphering relative age. However, in the present study, we found that compressive strength tests often were highly variable for any given measured deposit (Fig. 7B). This discrepancy could be because they only took fifteen measurements per boulder, calculated a mean and then removed the 5 values that deviated from this mean the most, and then recalculated the mean, whereas this study had a higher sample number and did not do any form of data smoothing.

Another potential source for the variability present in the Schmidt Hammer data of this study could be from difficulties making measurements in the field. The Schmidt Hammer was originally designed for testing the hardness of flat, smooth, concrete surfaces. Although efforts were made to measure the flatter surfaces of the boulders, the irregular surface morphologies are almost ubiquitous, which could have an effect on the measured rebound

values. Additionally, any lichen present on the boulders' surface would dampen the initial pulse of energy with which the Schmidt Hammer strikes the surface, further skewing the compressive strength results.

5.1.3 Roundness Data Uniformity

There are a few potential reasons why the roundness data shows little to no distinction from site to site. Firstly, the methods of assigning a roundness value using the Krumbein (1941) chart could be too low in resolution to decipher relative differences. In contrast, other methods could give a more detailed idea of the morphology of each boulder. For example, the Cailleux roundness index takes the individual convexities of a clast to assign a value of roundness (Rodriguez et al., 2013). Another alternative method could be using Fourier shape analysis (Schwarcz and Shane, 1969). Using methods such as these could give a more detailed estimation of the clast roundness, which could lead to a greater distinction among sites.

Another potential reason that the roundness data is fairly uniform between sites is that the roundness may not be indication of weathering time at all, but rather, could indicate the travel distance of the clasts (Rodriguez et al., 2013). Nearly all of the measured sites were on the coastal plain, 4 km to 8 km away from the source area. As such, if roundness is a metric of travel distance rather than weathering time, it makes sense that they would all be very similar to one another, regardless of the time since deposition. These reasons provide explanations as to why the results of the roundness data were deemed essentially useless for the purposes of this study.

5.1.4 Color Data Variability

Error in the color index data arises from the difficulty in assigning one color representative of the entire boulder. Often there could be many different colors present on the boulder surface, therefore a more in depth analysis of the various colors present within a site could result in a better indication of how color varies with weathering time. However, for the purposes of this research that was not feasible.

5.2 Bias Toward the Recent Geologic Past

Since the weathering rinds are removed during transport, the present weathering rind thickness represents the last distal movement of the boulders, biasing the debris flow record toward the more recent past. In other words, if a boulder from a deposit is re-entrained in another event, the weathering rinds thickness will only be indicative of the second, relatively younger event. Therefore, since older events have a higher chance of being recycled, it is likely that the debris flow history does not sufficiently represent the older events. This bias toward the present could explain why the record of predicted ages is more populated by events that occurred within the last ~30 ky (Table 5). It seems likely that extreme events such as the 2018 Montecito event or other very large Holocene and Upper Pleistocene events would tend to rework deposits from previous high-magnitude events or even smaller magnitude events, thus obscuring their occurrence in the record until longer term changes in base level or climate isolate and preserve the deposits. In the field, this phenomenon was observed at an uplifted marine terrace along the coast near site 2 (Fig. 15). In this terrace, a matrix-supported layer of large cobbles and pebbles can be seen below the surface layer. It is hypothesized that this layer is a debris flow deposit from an event that occurred prior to the one preserved at the surface; however, there is no surface evidence for this older event (see

Keller et al., 2020 for more information on this site). These observations provide evidence for high-magnitude events that are not recorded in the surface deposits examined by this study. These observations are consistent with the idea that the numerical components of diverse geomorphic and tectonic process rates are not independent of the measured time interval and that direct comparison of rates over variable time intervals may not be valid in some instances (Gardner et al., 1987). For example, results indicate that at least 17 events have occurred over the last approximately 96 ky, indicating a high-magnitude debris flow has occurred at least once every 5.6 ky, on average. However, if we instead look at the more recent past of the last 8 to 9 ky, in which there have been at least 5 events, results indicate that the average recurrence interval is 1.7 ky. These results imply not that the rate has nearly tripled in the recent past, but rather, the evidence for recent events has been better preserved, biasing the results toward the recent geologic past.

5.3 Multiple Regression Analysis

Due to the high R^2 values between numeric age and weathering rind thickness, compressive strength, and clast color, a multiple regression analysis was performed in an attempt to improve the correlation between the extent of weathering of the boulder and numeric age, therefore improving the ability to predict their age based on those features. Ultimately, this analysis indicated that the combination of weathering rind thickness and clast color best improves the correlation to numeric age, with an R^2 value of 0.86, compared to the R^2 values of 0.80 between weathering rind thickness and numeric age alone, and 0.70 for color and numeric age alone. As such, the equation for predicted age that uses both weathering rind thickness and color index is $t = 7738.97 \cdot w^{2.59} \cdot c^{-2.43}$, where t is the predicted age in thousands of years, w is the mean weathering rind thickness in millimeters, and c is

the mean color index for the deposit. However, when the predicted ages calculated from this equation were matched with their respective numeric age, the R^2 is 0.81, compared to the R^2 of 0.82 for the predicted ages using the equation using just weathering rind thickness and numeric age. Although these values are essentially the same, future applications of the methods for the former would require more field data collection and time for only a small improvement in correlation, therefore age prediction. Additionally, as previously mentioned, it can be difficult to determine a single color representative of the entire boulder, which lowers the precision of this weathering indicator. It is for these reasons that the age prediction equation that only uses average weathering rind thickness was used rather than the multiple regression analysis.

5.4 Tracing Debris Flow Paths Through Time

The predominant path that past debris flows followed can be traced using the geographical locations of boulders with weathering rinds of similar thickness. For example, the similarity in weathering rind thickness among sites 2, 3, and 6 show that debris flows can extend from their source area in the mountains to the ocean (Fig. 6). This is a phenomenon that was also observed during the Montecito events (Kean et al., 2019; Keller et al., 2020) but the path of these sites provides evidence that this also happened in the past. Additionally, sites 1, 4, 5, 7, and 8 have similarly thin weathering rind thicknesses and follow a path down Mission Canyon, along the present channel of Mission Creek (Fig. 6). According to their predicted ages (Table 5), these deposits are from events that occurred within about 2 ky of each other. This grouping of debris flow deposits also indicates that this path has been the flow path for both Mission Creek and debris flows alike for at least the last ~4 ky.

Additionally, weathering rind thickness can also give insight into how the dominant paths of debris flows have changed over time. For example, deposits within the thick subgroup of weathering (therefore relatively older ages) at sites 25, 26, 28, 29, and 30, follow a path that crosses what is now Mission Ridge (Fig. 6). Mission Ridge is a growing anticline that uplifts and folds a very large debris flow fan, has a local relief of about 100 m, and is part of the Mission Ridge fault system of Santa Barbara (Fig. 4). It can be inferred that the flows that created the deposits at these sites presently reside in a paleochannel of Mission Creek and happened in events prior to uplift dominating this area. According to the predicted ages of these deposits, this debris flow path was active from about 55 ka to 96 ka (Table 5). Relative to the aforementioned group of younger sites with thin rinds, these older sites reside farther to the east. The path of the intermediate aged sites in this area is much less pronounced. Overall though, the trend of decreased rind thickness, therefore younger flow age, moving from east to west could be due to the westward propagation of Mission Ridge. As uplift outcompetes the incision of Mission Creek, the channel moves farther to the west, along with the likely path of debris flows. This trend would imply that the present debris flow hazard is smaller for the area surrounding the older subgroup of sites and is increasing toward the west.

More generally, this assessment illustrates how weathering rinds can be used independently of numeric age to give an indication of the debris flow history of an area, as it pertains to the dominant flow paths within a relative time period. Furthermore, with numerical ages and calibrated rind development, weathering rind thickness could indicate how long that flow path was sustained.

5.5 Implications of Debris Flow Recurrence and Hazard

Upon deciphering the average recurrence intervals of high-magnitude debris flows within the study area, further implications can be assessed. The recurrence interval of 1.7 ky indicated that the probability of another high-magnitude event happening in this study area in the next 100 years is 5.78% (Table 7). However, as previously mentioned, it is highly likely some events have not been accounted for due to the possibility of reworking previous deposits. Yet, in a hypothetical instance of there being twice as many events present in the record, probability calculations indicate a ~1% chance of another event happening in the next 10 years (Table 7). Of course, these probabilities do not rule out the possibility for two events to occur closer in time to one another, but rather, indicates that it is unlikely.

Also, this low probability of high magnitude events does not mean that smaller, but still destructive events, cannot happen on shorter time scales. The historical record for this area includes three smaller events that occurred in 1914, 1964, and 1969 that caused considerable damage to the community. In January of 1914, the Santa Barbara area received intense rainfall of approximately 23 cm within 48 hours, with some areas receiving 10 cm within only a two-hour period (State of California, 2013). This precipitation resulted in debris-laden flash flooding that destroyed 12 homes and 6 bridges in the Mission Creek area and caused 22 deaths (US Army Corps of Engineers Los Angeles District, 1999; State of California, 2013). Another damaging historical event includes the debris-laden floods of 1964 that followed the Coyote Fire. During this event, it was reported that boulders moved down streambeds, plugged bridges, and altered stream channels, causing mudflows over several residential areas of Montecito (US Army Corps of Engineers Los Angeles District, 1999). Only a few years later, a major flood occurring in January 1969 reportedly caused

considerable damage to the Montecito area. Luckily a debris dam had been put in place after the flooding in 1964, which prevented potentially more substantial damages for some residents along Cold Spring Creek, but the residents near Montecito Creek were not so fortunate. Montecito Creek crested its banks during this event and destroyed houses with its boulder-laden, muddy load (Santa Barbara County, 1969). Present research by Gurrola and Rogers (2020) investigating the flood and landslide history of the Montecito watersheds indicates that there have been at least eleven debris flow and debris laden flood events in the area since 1825. With the exception of the 2018 event, these events have been relatively small in magnitude, affecting one or two watersheds. This number of events indicates an average recurrence interval of about 17 years, or using the Poisson event probability equation, a 5.5% chance of an event happening in any given year. The history of these events demonstrates that although the present study has concluded that the recurrence interval of high-magnitude, Montecito 2018-sized events is on the order of 1 to 2 ky, smaller events happen much more often and can still be destructive to the community.

Overall, the magnitude and frequency of these mass wasting events are likely most related to the sediment and boulder supply in the source area channels. Research has shown the timing and magnitude of debris flows following wildfire is dominantly controlled by short duration, high-intensity rainfall capable of producing overland flow (Cannon et al., 2008; Kean et al., 2011; Staley et al., 2013, 2017; McGuire et al., 2017). However, post-fire sediment production is also largely dependent on the availability of sediment (Keller et al., 1997). The amount of time necessary to build up sufficient material to produce another large, boulder-rich debris flow after one has occurred is largely unknown. However, if a channel is lacking large amounts of loose sediment, boulders, and debris, fluvial flushing of sediment is

probably the more likely sediment transport process to occur following wildfire in a chaparral environment (Florsheim et al., 1991; Keller et al., 1997, 2019). These assessments could indicate why the recurrence interval of these very high-magnitude events are on the order of thousands of years – this could be the amount of time needed to fully load the channel.

Additionally, the recurrence interval estimate is for the entire study area, therefore, although it is outside the scope of this research, further research could make distinctions for individual catchments and canyons to better assess the present risk and exposure to high-magnitude debris flows. Overall, the recurrence interval for any one canyon is likely longer than the 1.7 ky estimated for the entire study area, but individual canyons may have higher or lower likelihoods than one another. Large tributary basins may have a greater probability of experiencing a debris flow after a storm event because there is a larger source area (May and Gresswell, 2004). A contrasting hypothesis, however, is that smaller watersheds are more susceptible to high-magnitude mass movements because larger ones are less likely to experience burning of the entire catchment, which would dampen sediment transport processes in the more extended fluvial network (Lavé and Burbank, 2004). However, events in these smaller catchments are still a function of the amount of readily moveable debris stored in the channels, which is likely lower than the larger catchments. Other factors such as catchment slope, shape, and drainage density would have varying effects on individual debris flow susceptibility and the recurrence interval thereof. Further research could explore how these different factors affect the resulting number of past high-magnitude debris flow deposits in any one canyon.

6. Conclusions

Conclusions from this study are:

1. The hypotheses that the boulders of debris flow deposits will increase in weathering rind thicknesses, be redder in color, and decrease in compressive strength as they age were accepted based on their respective R^2 values of 0.80, 0.70, 0.56 when compared to numeric age. The hypothesis that the boulders will become rounder was rejected due to the R^2 values of 0.11 when compared to numeric age. Based on these R^2 values, weathering rind thickness was concluded to be the most reliable calibrated dating method for estimating the age of debris flow deposits.
2. The paths of past debris flows can be traced using the relative distinctions of the boulders within deposits based on their weathering rind thicknesses. These methods indicate that the exposure to the debris flow hazard in Mission Canyon has moved west ~1 km due to lateral propagation of the Mission Ridge Anticline.
3. In our study area, the equation that estimates the rate of weathering rind development is $t=0.012(w^{3.80})$, where t is the predicted age of the deposit in thousands of years and w is the mean weathering rind thickness in millimeters.
4. Using this calibrated rate, weathering rinds provide a readily applied field method to estimate the age of past debris flow events. However, it is best suited for younger to intermediate aged events because the variability is greater with increasing age.
5. Results of statistical paired tests and geospatial analysis indicate that the age of flows range from the present to ~96 ka and at least 17 high-magnitude flow deposits were identified in the study area. These results indicate a recurrence interval of 5.6 ky for the entire time period. However, a more probable recurrence interval is 1.7 ky when

using the history of the last ~9 ky, which gives a 5.78% probability of another event happening in the next 100 years. Due to the possibility of re-entrained older events or missed deposits, these represent the minimum number of events, therefore maximum recurrence intervals. Additionally, these estimates do not mean that two events cannot happen closer in time, but rather, these numbers give an indication that the likelihood of another event in the next 100 years is low.

6. Small to moderate flows (M3-4) are possible after every wildfire event and have the ability to cause damage, but this research focused on channel-clearing, very large-sized flows (M5+). Understanding the mechanisms of these past high-magnitude flows can provide insight into the frequency and risk of large events in the future. In summation, the data support the hypothesis that debris flows the size of the Montecito 2018 event occur once every 1 to 2 ky, on average.

7. Figures & Tables

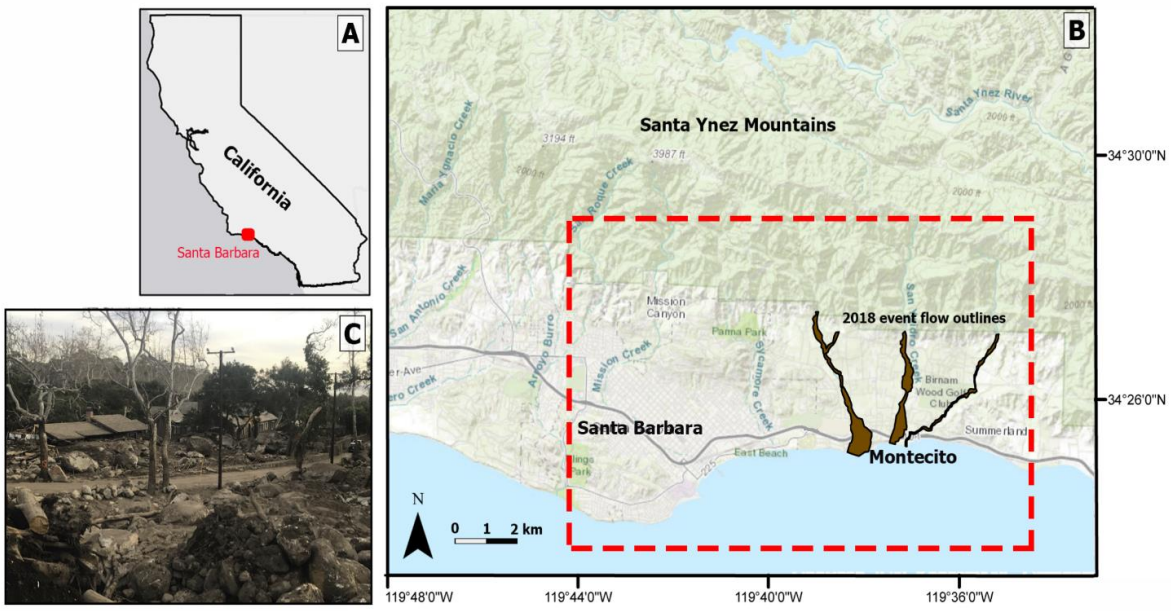

Figure 1: (A) Study location in California, USA. (B) Overview of the area, with the specific study area outlined in the red dashed box and the approximate flow area of the 2018 Montecito debris flow events shown in brown. Basemap provided by Esri. (C) Photo showing a home inundated with mud, boulders, and debris, illustrating the kind of damage the 2018 event caused.

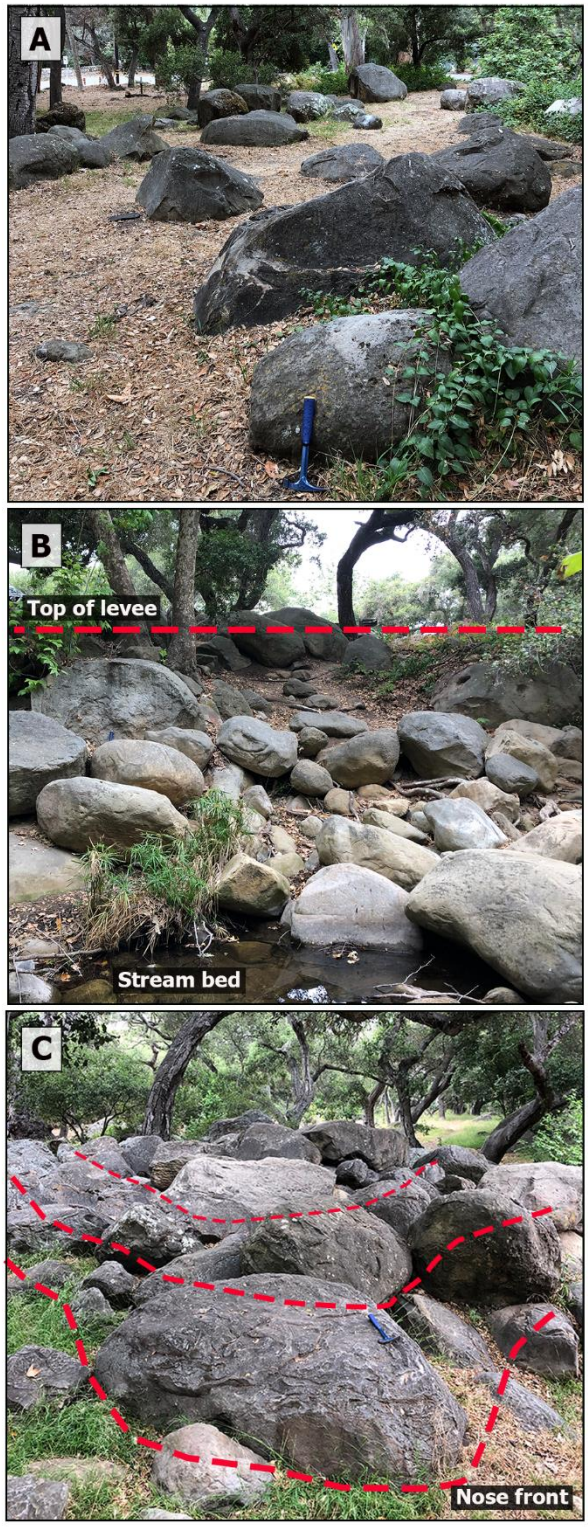

Figure 2: Photos A, B, C show debris flow deposits as a boulder field, levee, and nose, respectively. Rock hammer for scale. Photos were taken at Rocky Nook Park, Santa Barbara, CA (site 4).

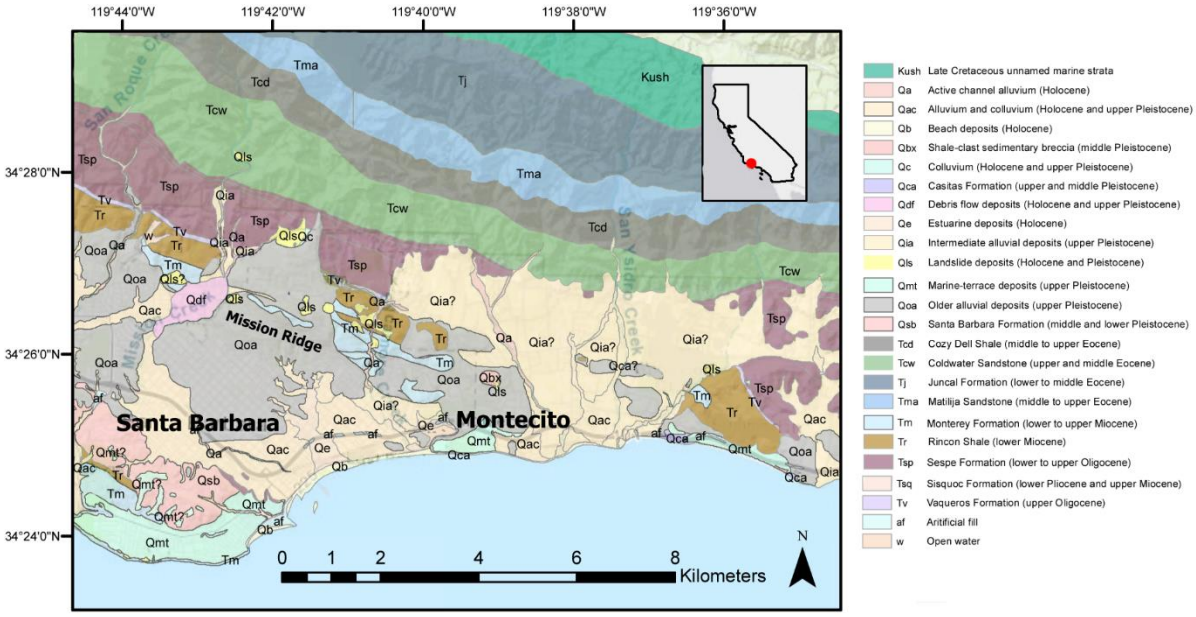

Figure 3: Simplified geologic map of the study area. Shows likely source areas of boulders (Tma and Tcw) within the debris flow deposits, along with all other Pre-Quaternary and Quaternary deposits in the area. The question makes next to labels on map signify a degree of uncertainty. Basemap provided by Esri. Geologic units modified from Dibblee 1986a & 1986b.

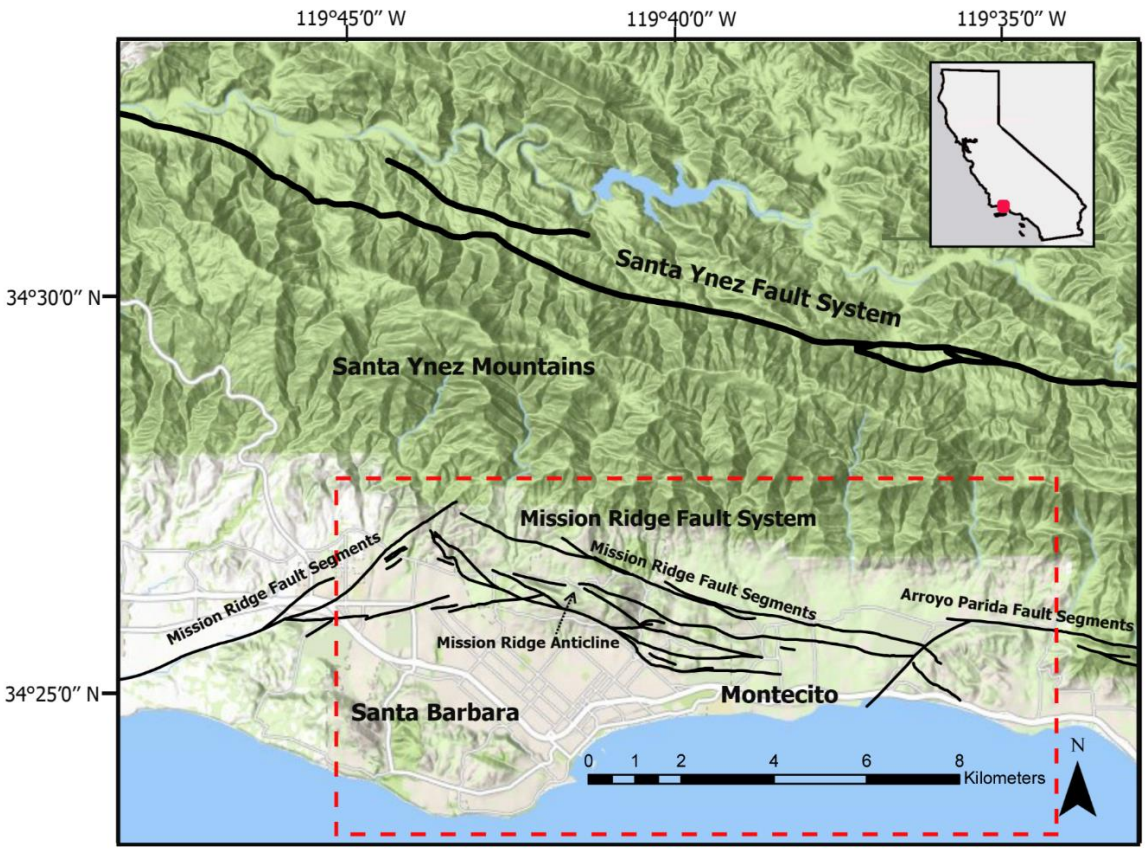

Figure 4: Seismic sources of the Santa Barbara Fold Belt. The Mission Ridge Fault System is subdivided into the 3 segments, here showing the middle and eastern segments, the Mission Ridge Fault and the Arroyo Parida Fault, both of which are reverse faults. The Santa Ynez strike-slip fault is shown to the north. The study area of this project is outlined in the red dashed box. Relief basemap from Esri. Fault lines from United States Geological Survey and California Geological Survey.

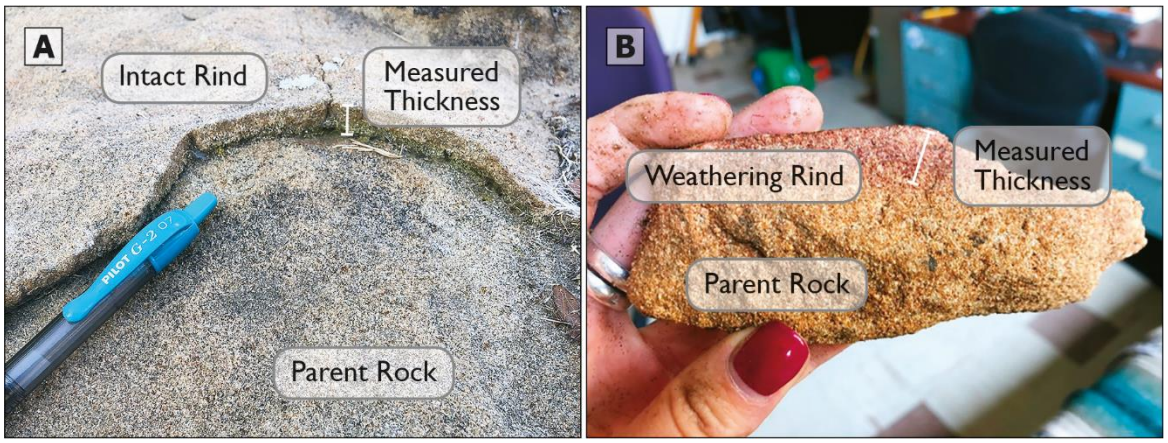

Figure 5: Photo A illustrates the predominant method used to measure the weathering rind thicknesses on the boulders using the edge of where pieces of rind have broken off. Photo B illustrates the alternative method of deciphering weathering rind thickness using color difference.

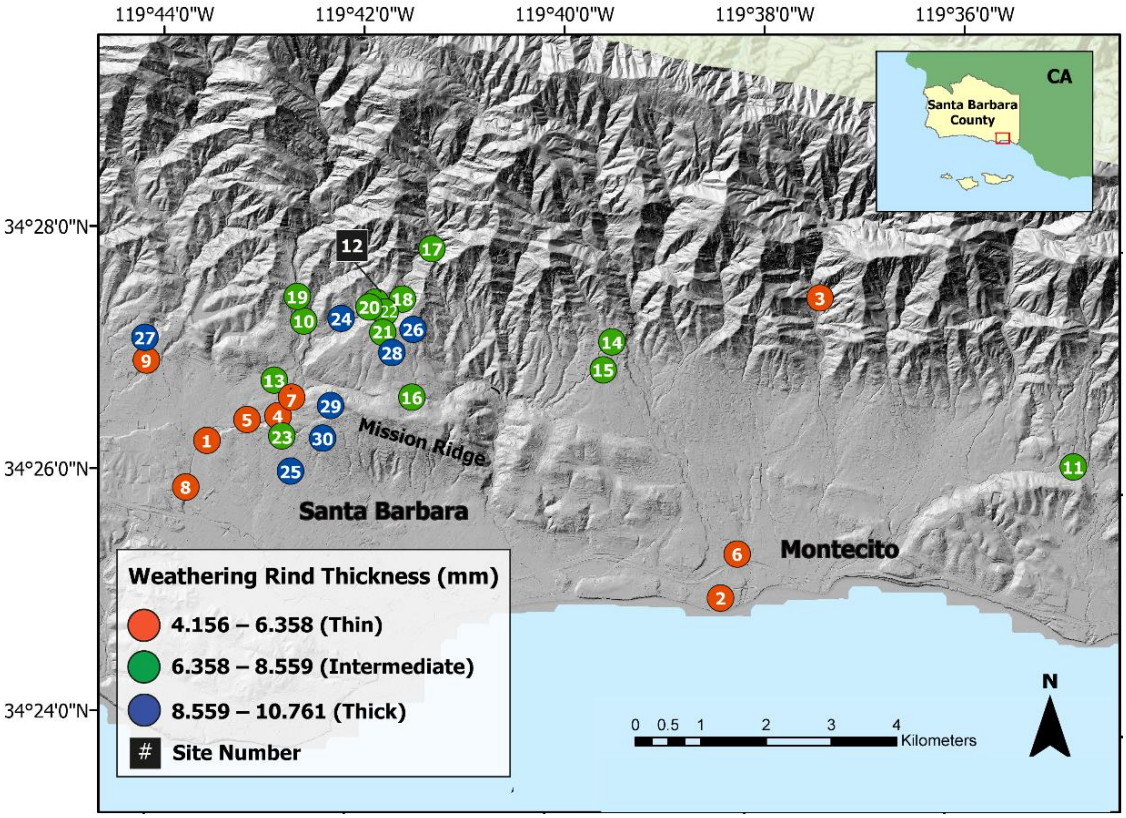

Figure 6: Map of where all weathering indicators measurements were made. Each circle represents a site. The color of circles indicates the average weathering thickness for that site. Relief basemap created using a 2018 airborne LiDAR bare-earth DEM of the Santa Barbara coastal plain (DOC/NOAA/NOS/OCM, 2018).

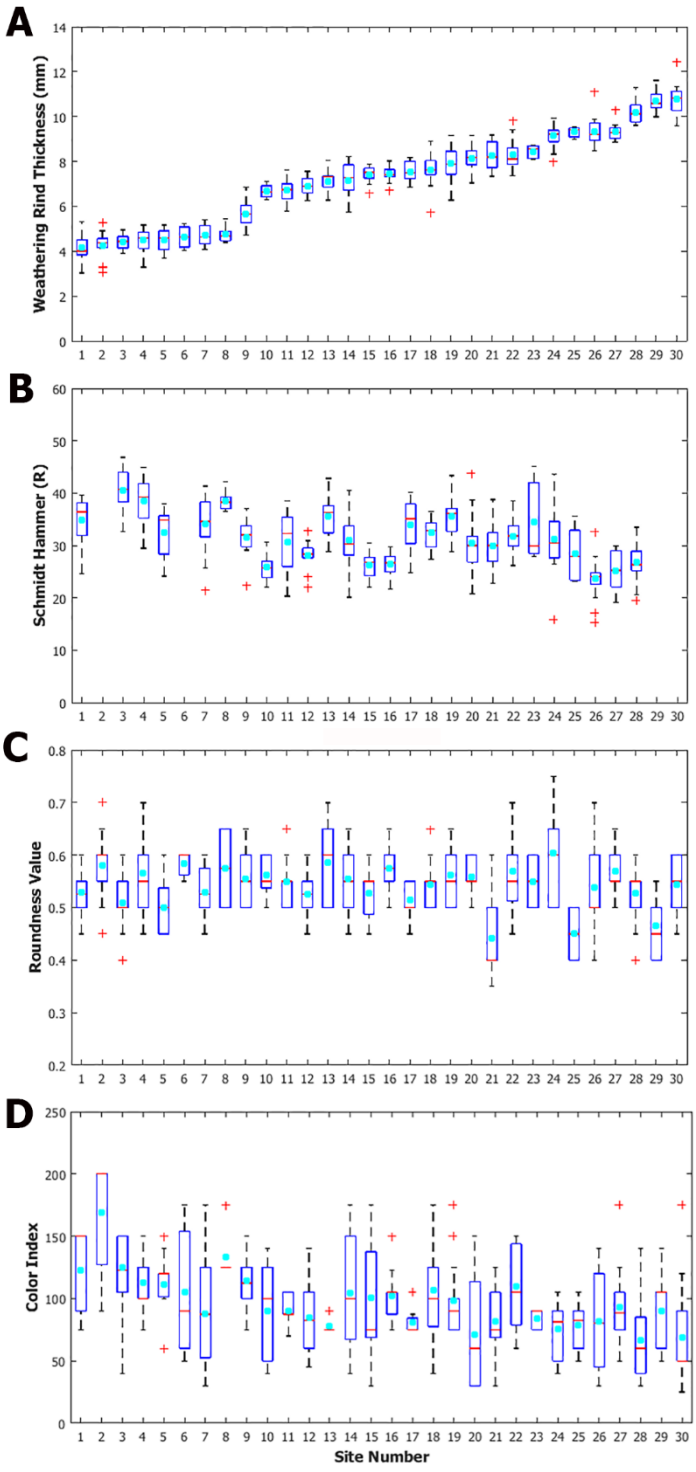

Figure 7: Box plots of data for all weathering indicators for each site. The blue box is the interquartile range of the data for that site. The red line is the median for the site. The whiskers are the minimum and maximum values. The bright blue dot is the overall mean for the site. A, B, C, D are the weathering rind thickness, Schmidt Hammer rebound values, roundness values, and color index data, respectively, for each site. (See **Fig. 6** for site locations).

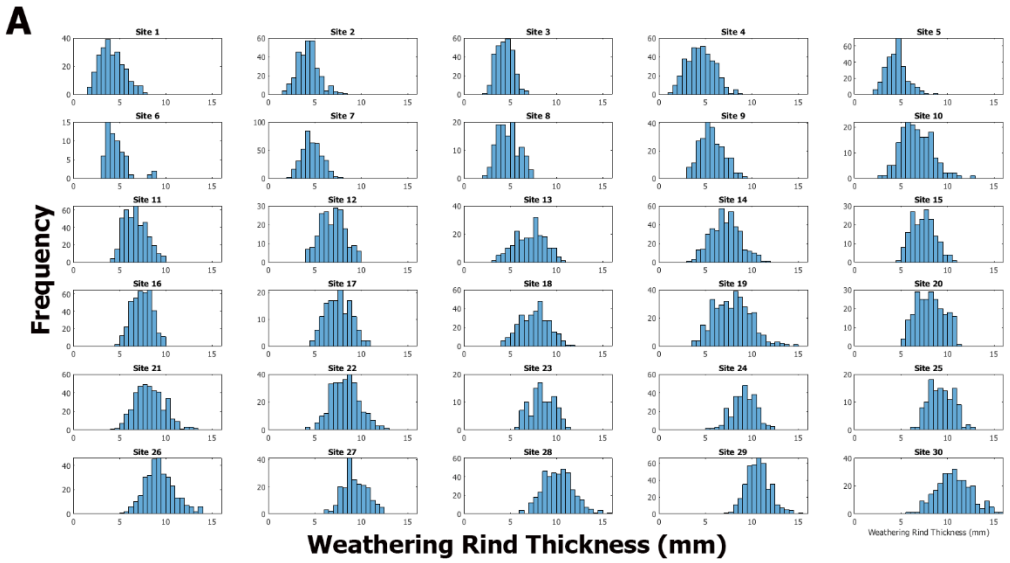
A
Site 1
Site 2
Site 3
Site 4
Site 5
Site 6
Site 7
Site 8
Site 9
Site 10
Site 11
Site 12
Site 13
Site 14
Site 15
Site 16
Site 17
Site 18
Site 19
Site 20
Site 21
Site 22
Site 23
Site 24
Site 25
Site 26
Site 27
Site 28
Site 29
Site 30
Frequency
Weathering Rind Thickness (mm)

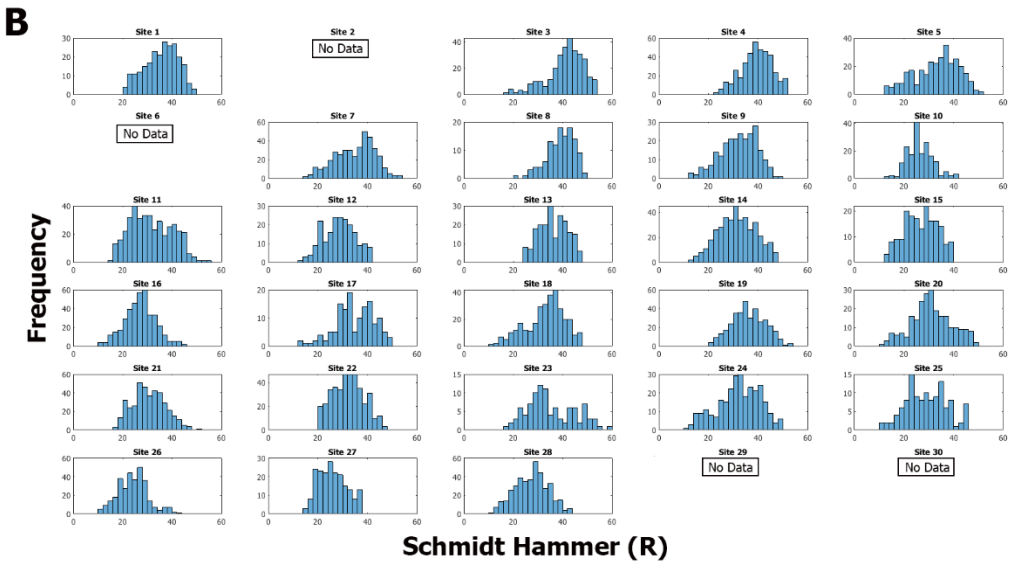
B
Site 1
Site 2
No Data
Site 3
Site 4
Site 5
Site 6
No Data
Site 7
Site 8
Site 9
Site 10
Site 11
Site 12
Site 13
Site 14
Site 15
Site 16
Site 17
Site 18
Site 19
Site 20
Site 21
Site 22
Site 23
Site 24
Site 25
Site 26
Site 27
Site 28
Site 29
No Data
Site 30
No Data
Frequency
Schmidt Hammer (R)

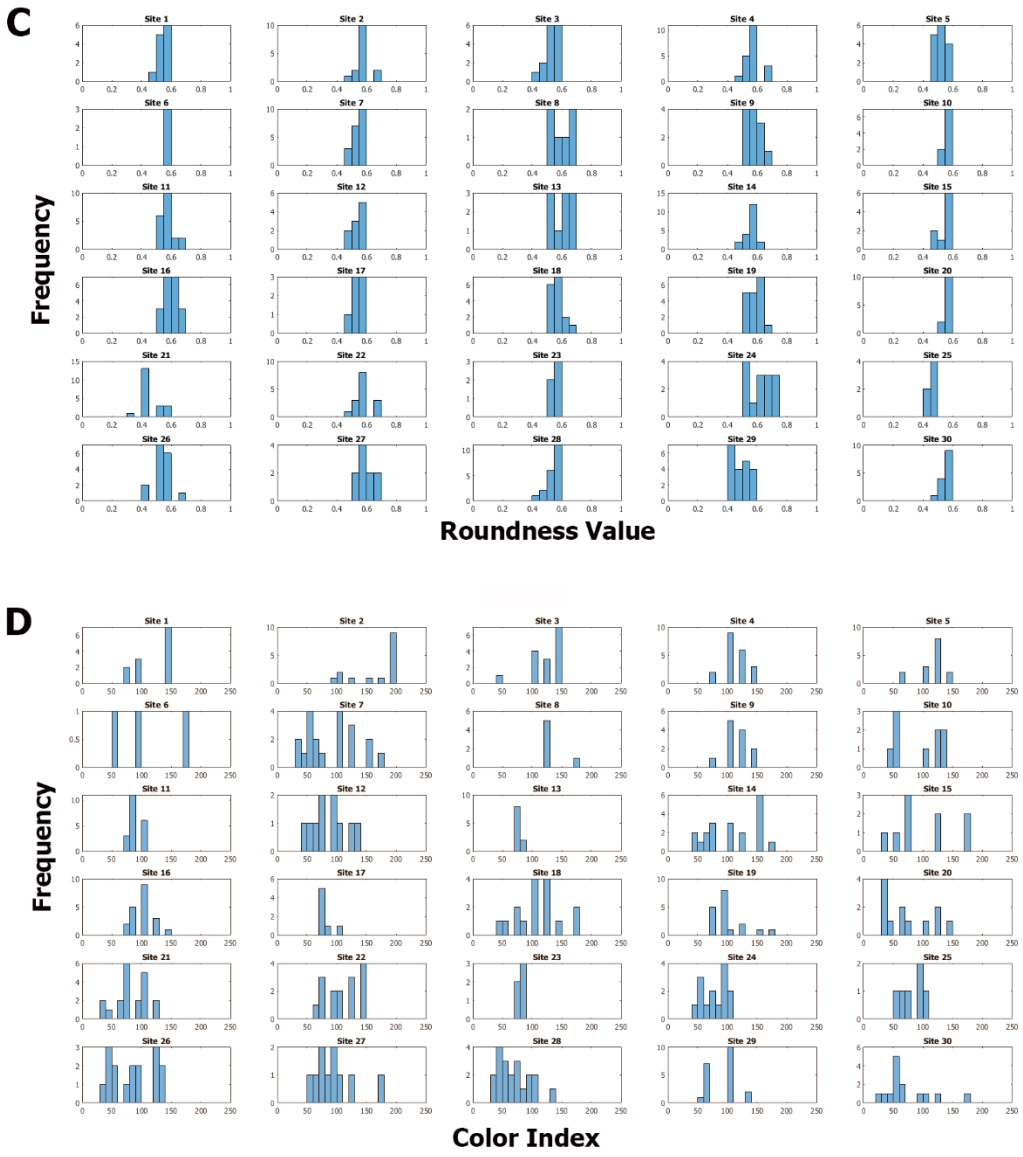

Figure 8: Histograms of the data for each weathering indicator per site. Individual histograms show the general distribution of the data for each site. A, B, C, D are the weathering rind thickness, Schmidt Hammer rebound values, roundness values, and color index data, respectively, for each site.

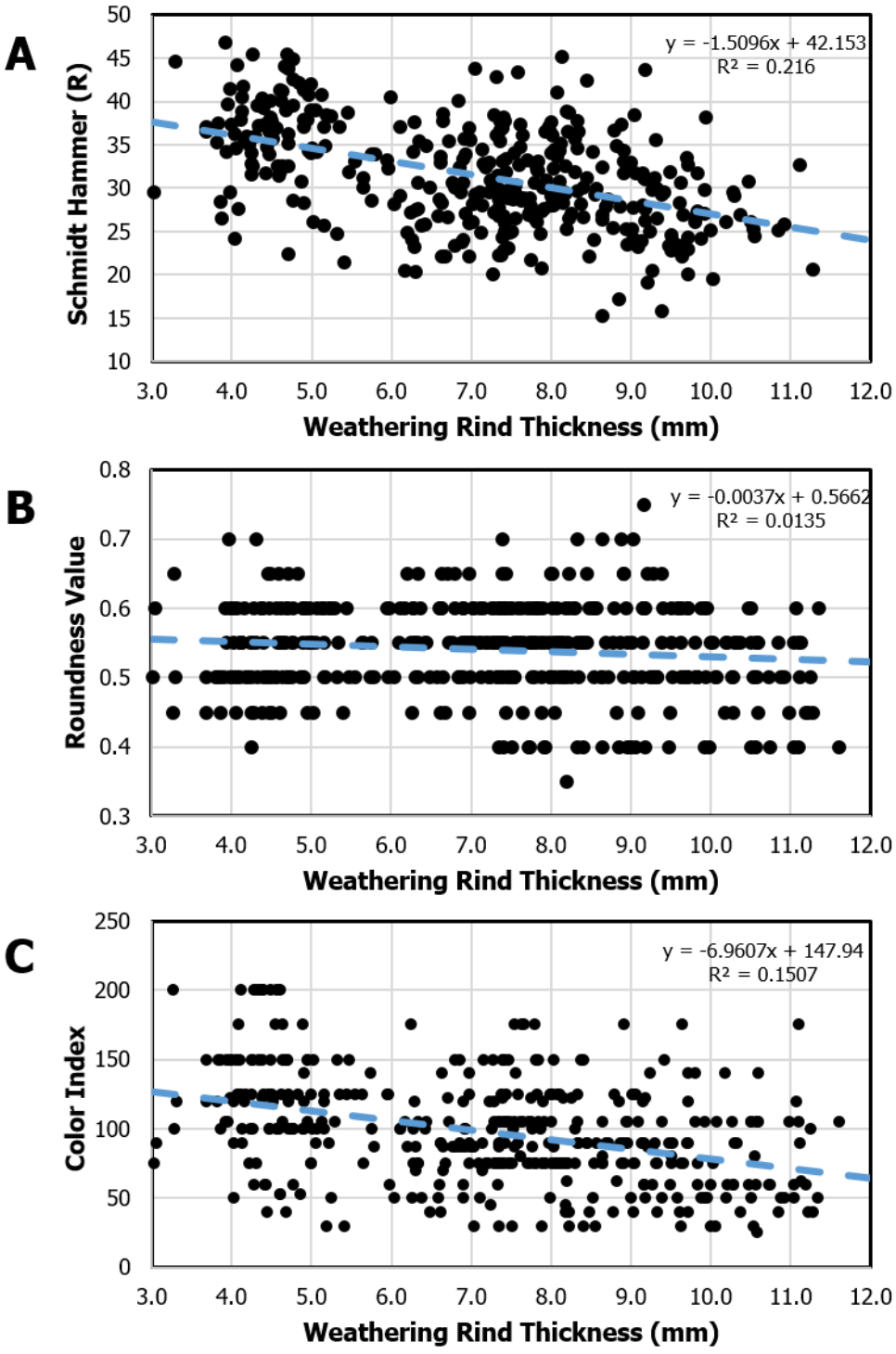

Figure 9: Plots of relationships between each weathering indicator and weathering rind thickness. Each point in every graph represents the average weathering rind thickness for a given boulder vs the average of the respective weathering indicator for that boulder. Subplots A, B, and C are the weathering rind thickness data matched with Schmidt Hammer rebound values, roundness values, and color index data, respectively.

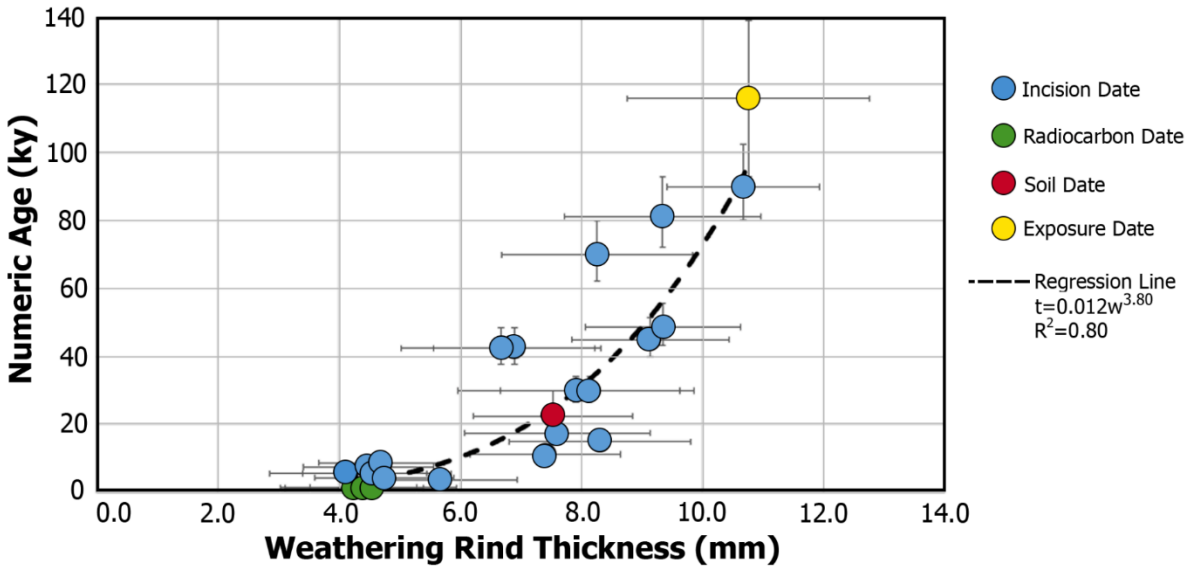

Figure 10: Calibration curve of average weathering rind thickness of the boulders where each numeric age was estimated vs that numeric age estimation. The color of data points indicates the type of numeric age. Horizontal error bars are +/- 1 standard deviation of the weathering rind thicknesses of each site. Vertical error bars represent age control for each type of numeric dating method. The regression line estimates the rate of weathering rind development such that $t=0.012(w^{3.80})$, where t is the predicted age in thousands of years and w is mean the weathering rind thickness in millimeters. The data used to construct this graph can be found in **Table 4**.

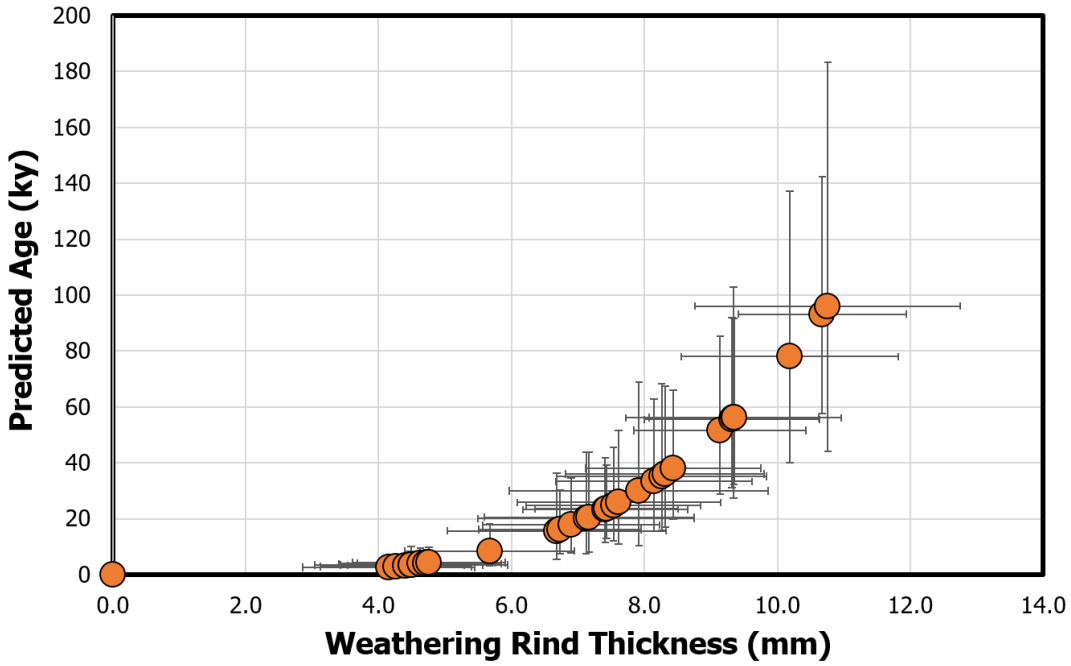

Figure 11: Predicted ages were calculated using the regression line equation from the calibration curve, (**Fig. 10**), $t=0.012w^{3.80}$, and the average weathering rind thickness for each of the 30 sites. This plot represents all 30 of those predicted ages. Horizontal error bars are +/- 1 standard deviation of the weathering rind thicknesses of each site. Vertical error bars are the upper and lower age bounds for a given site, deemed by calculating the predicted age for the average weathering rind thickness minus 1 standard deviation and calculating the predicted age for the average weathering rind thickness plus 1 standard deviation. Values of predicated ages, as well as upper and lower age bounds can be found in **Table 5**.

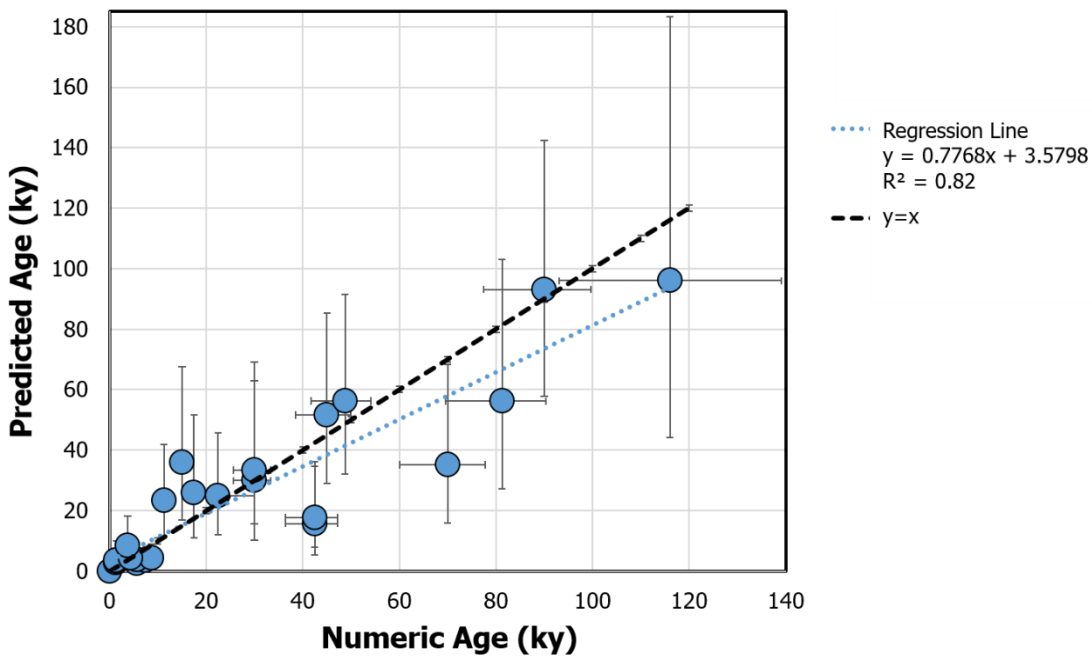

Figure 12: Plot of predicted ages deemed from calibration curve equation vs respective numeric age (^{14}C, exposure, soil, and incision dates). Horizontal error bars indicate the age control for that particular numeric age method. Vertical error bars indicate the calculated range of the predicted age.

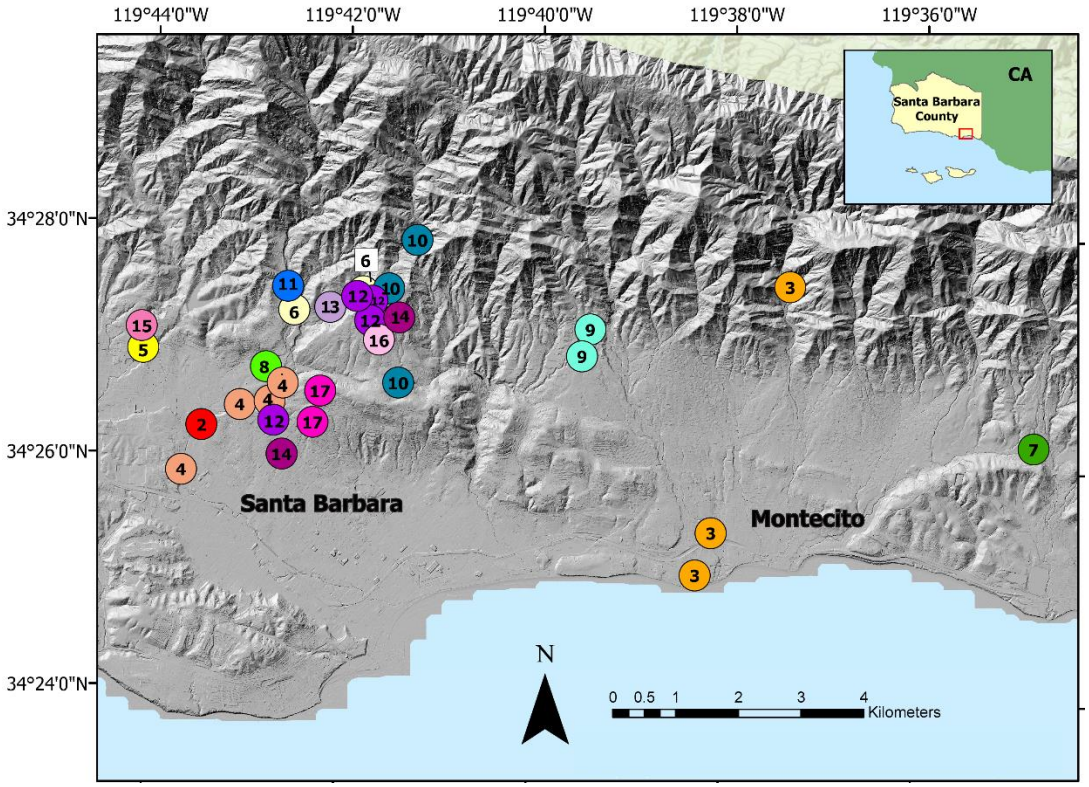

Figure 13: Map of sites with the color of points representing the distinct event in which that deposit occurred. The number on points also indicates the event number (2018 event being event #1, not shown); more information about distinct events can be found in **Table 5**. Relief basemap created using a 2018 airborne LiDAR bare-earth DEM of the Santa Barbara coastal plain (DOC/NOAA/NOS/OCM, 2018).

Figure 14: Photo of multiple generations of weathering rind development, taken at site 18.

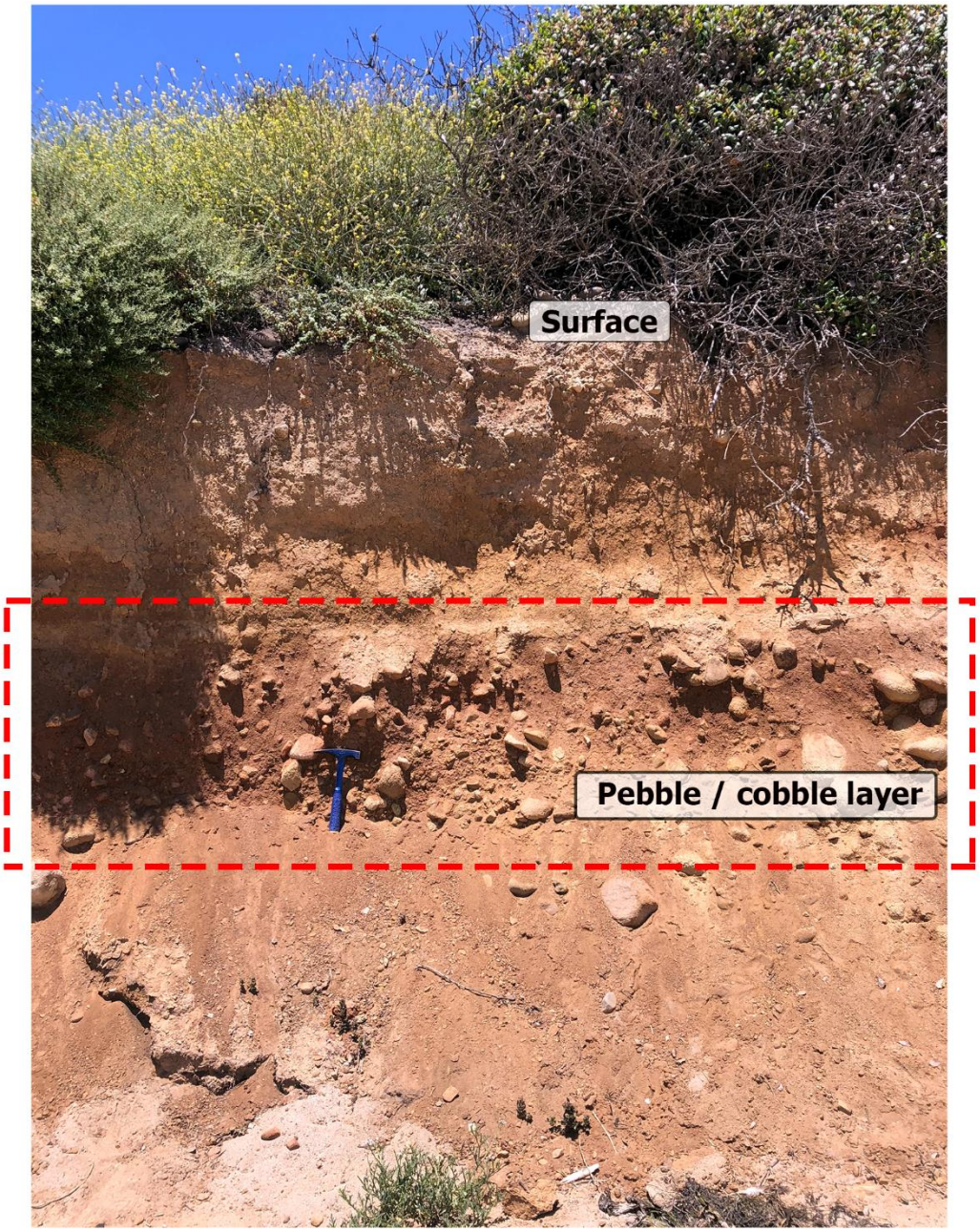

Figure 15: Uplifted marine terrace near site 2 with a matrix-supported layer of large cobbles and pebbles, hypothesized to be a debris flow deposit that is not represented at the surface. Rock hammer for scale. See Keller et al., 2020 for more information on this site.

Table 1: Means, standard deviations, and coefficients of variation for each site for each of the dating methods applied. Site locations can be found in **Fig. 6**. Site numbers highlighted in the orange, green, or blue boxes represent the relative thin, intermediate, and thick subgroups in which they fall, respectively.

	Weathering Rind Thickness (mm)				Schmidt Hammer (R) Values				Roundness Value				Color Index			
Site #	Mean	Std. Dev.	CV	n	Mean	Std. Dev.	CV	n	Mean	Std. Dev.	CV	n	Mean	Std. Dev.	CV	n
1	4.156	1.296	31.19	240	34.8	6.8	19.4	0	0.53	0.04	8.14	12	122.5	32.9	26.8	12
2	4.261	1.141	26.78	300	-	-		300	0.58	0.06	10.34	15	169.3	42.1	24.8	15
3	4.406	0.877	19.90	300	40.4	7.3	18.0	300	0.51	0.05	9.61	15	124.8	29.9	24.0	15
4	4.488	1.452	32.35	400	38.6	6.2	16.2	400	0.57	0.06	10.87	20	112.5	21.7	19.2	20
5	4.491	1.071	23.85	300	32.5	8.9	27.2	300	0.50	0.04	8.94	15	111.7	23.8	21.3	15
6	4.627	1.224	26.46	60	-	-		0	0.58	0.02	4.04	3	105.0	52.1	49.6	3
7	4.711	1.035	21.96	400	34.2	8.0	23.4	400	0.53	0.05	9.62	20	87.9	42.5	48.3	20
8	4.757	1.147	24.12	120	38.6	5.6	14.5	120	0.58	0.06	10.94	6	133.3	18.6	14.0	6
9	5.673	1.277	22.51	240	31.5	6.3	20.0	240	0.55	0.05	8.61	12	114.6	21.6	18.8	12
10	6.677	1.646	24.65	180	25.8	5.1	19.9	180	0.56	0.04	7.00	9	90.0	39.7	44.1	9
11	6.730	1.218	18.10	400	30.7	8.4	27.5	400	0.55	0.04	8.13	20	90.1	11.4	12.7	20
12	6.900	1.330	19.27	200	28.1	6.4	22.9	200	0.53	0.05	9.76	10	85.0	28.9	34.0	10
13	7.123	1.630	22.88	200	35.5	5.8	16.2	200	0.59	0.07	11.50	10	78.0	6.0	7.7	10
14	7.167	1.577	22.00	400	31.0	7.7	24.7	400	0.56	0.06	10.23	20	104.8	42.4	40.5	20
15	7.408	1.240	16.74	180	26.2	6.7	25.5	180	0.53	0.05	9.06	9	100.6	49.2	48.9	9
16	7.430	1.072	14.43	400	26.4	6.3	24.0	400	0.58	0.05	8.02	20	102.5	17.5	17.1	20
17	7.536	1.311	17.40	140	33.9	7.9	23.3	140	0.51	0.03	6.80	7	81.1	10.7	13.2	7
18	7.613	1.531	20.11	320	32.4	7.9	24.5	320	0.54	0.04	7.88	16	106.6	37.2	34.9	16
19	7.916	1.949	24.62	360	35.5	6.8	19.1	360	0.56	0.05	8.16	18	98.3	27.1	27.6	18
20	8.144	1.480	18.17	240	30.4	8.2	26.9	240	0.56	0.03	6.15	12	71.3	41.5	58.2	12
21	8.262	1.576	19.08	400	29.9	6.7	22.2	400	0.41	0.01	2.49	20	81.6	26.5	32.5	20
22	8.310	1.495	17.99	300	31.7	6.3	20.0	300	0.57	0.07	11.46	15	109.7	30.7	28.0	15
23	8.434	1.317	15.61	100	34.5	9.7	28.2	100	0.55	0.04	8.13	5	84.0	7.3	8.7	5
24	9.139	1.296	14.18	280	31.3	8.6	27.5	280	0.60	0.08	13.45	14	75.5	21.0	27.8	14
25	9.315	1.321	14.19	120	28.5	8.4	29.6	120	0.45	0.04	9.07	6	78.3	18.9	24.1	6
26	9.343	1.617	17.31	320	23.6	6.1	26.0	320	0.54	0.08	14.52	16	81.6	36.5	44.7	16
27	9.347	1.279	13.68	200	25.1	5.8	23.1	200	0.57	0.05	8.95	10	93.3	33.9	36.4	10
28	10.188	1.633	16.03	400	26.8	6.8	25.3	400	0.53	0.05	10.15	20	66.3	28.5	43.0	20
29	10.676	1.262	11.82	400	-	-		0	0.47	0.06	12.31	20	89.8	27.4	30.5	20
30	10.761	1.996	18.55	280	-	-		0	0.54	0.05	8.43	14	68.4	39.5	57.7	14

Table 2: R^2 values of each relative dating method correlated to numeric age. Data used for these correlations are of average weathering indicator of the boulders where each numeric age was estimated vs that numeric age estimation. This table also indicates the average standard deviation (Std. Dev.) and coefficient of variation (CV) for each of the relative dating methods.

	R^2 with Absolute Age	**Avg Std. Dev.**	**Avg CV (%)**
Weathering Rind Thickness (mm)	0.80	1.377	20.2
Schmidt Hammer Rebound Value	0.56	7.106	22.9
Roundness Value	0.11	0.049	9.1
Color Index	0.70	28.903	30.6

Table 3: Results of Kolmogorov-Smirnov test for normality. A p-value greater than 0.05 indicates that the null hypothesis that the distribution of the data for that site is normal is accepted. The Y's and N's indicate which sites have accepted or rejected the null hypothesis, respectively; C indicates the null hypothesis is conditionally accepted, meaning a p-value between 0.01 and 0.05.

Kolmogorov-Smirnov Test		
Site	**p-value**	**Normal?**
1	0.028	C
2	0.062	Y
3	0.094	Y
4	>0.15	Y
5	<0.01	N
6	0.041	C
7	<0.01	N
8	0.03	C
9	>0.15	Y
10	0.074	Y
11	<0.01	N
12	0.142	Y
13	0.062	Y
14	>0.15	Y
15	0.08	Y
16	>0.15	Y
17	>0.15	Y
18	>0.15	Y
19	>0.15	Y
20	0.128	Y
21	0.069	Y
22	>0.15	Y
23	>0.15	Y
24	>0.15	Y
25	>0.15	Y
26	0.023	C
27	0.017	C
28	>0.15	Y
29	0.022	C
30	>0.15	Y

Table 4: All estimated numeric ages, the upper and lower range as deemed by the age control for that dating method, and the type of date for each site. These values were used to create the calibration curve of **Fig. 10** by correlating the age to the respective weathering rind thickness (WRT). The standard deviation was used to show the margin of error within the weathering rind thickness data.

Site #	Age (ky)	Age Lower Range (ky)	Age Upper Range (ky)	Type of Date	Avg WRT (mm)	WRT Std. Dev. (mm)
0	0.002	0	0	Historic (Montecito 2018 Event)	0	0
1	5.630	0.625	0.8036	Incision Rate, .8m/ky	4.156	1.296
2	1.343	0.029	0.014	Calibrated Radiocarbon	4.261	1.1409
3	1.529	0.009	0.0290	Calibrated Radiocarbon	4.406	0.877
4	1.420	0.070	0.070	Calibrated Radiocarbon (Urban, 2004)	4.488	1.4519
5	7.5	0.833	1.0714	Incision Rate, .8m/ky	4.491	1.0712
6	5.625	0.625	0.8036	Incision Rate, .8m/ky	4.627	1.2241
7	8.75	0.972	1.2500	Incision Rate, .8m/ky	4.711	1.0347
8	4.375	0.486	0.6250	Incision Rate, .8m/ky	4.757	1.1474
9	3.75	0.417	0.5357	Incision Rate, .8m/ky	5.673	1.2772
10	42.5	4.722	6.0714	Incision Rate, .8m/ky	6.677	1.6462
12	42.5	4.722	6.0714	Incision Rate, .8m/ky	6.900	1.3298
15	11.25	1.250	1.6071	Incision Rate, .8m/ky	7.408	1.2403
17	22.5	7.500	7.5000	Soil Date (Best, 1989)	7.536	1.311
18	17.5	1.944	2.5000	Incision Rate, .8m/ky	7.613	1.5308
19	30	3.333	4.2857	Incision Rate, .8m/ky	7.916	1.9485
20	30	3.333	4.2857	Incision Rate, .8m/ky	8.144	1.4795
21	70	7.778	10.0000	Incision Rate, .8m/ky	8.262	1.576
22	15	1.667	2.1429	Incision Rate, .8m/ky	8.310	1.4951
24	45	5.000	6.4286	Incision Rate, .8m/ky	9.139	1.296
26	81.25	9.028	11.6071	Incision Rate, .8m/ky	9.343	1.6174
27	48.75	5.417	6.9643	Incision Rate, .8m/ky	9.347	1.2786
29	90	9.722	12.5000	Incision Rate, .8m/ky	10.676	1.2618
30	116	23.000	23.0000	Exposure Age (Landis et al., 2002)	10.761	1.9959

Table 5: Predicted ages of all 30 measured sites, as well as the upper and lower age bounds, calculated using the equation $t=0.012w^{3.80}$ from the calibration curve in **Fig. 10**. The upper and lower predicted age bounds for a given site were calculated using the average weathering rind thickness (WRT) +/- 1 standard deviation This table also indicates the event number in which each site deposit occurred; location of these events can also be seen in **Fig. 13.**

Site #	WRT Avg. (mm)	WRT Std. Dev. (mm)	Predicted Age (ky)	Predicted Age Lower Bound (ky)	Predicated Age Upper Bound (ky)	Event Number
0	0	0.000	0.000	0.000	0.000	1
1	4.156	1.296	2.591	0.627	7.262	2
2	4.261	1.141	2.849	0.873	7.012	3
3	4.406	0.877	3.235	1.393	6.444	3
4	4.488	1.452	3.470	0.787	10.057	4
5	4.491	1.071	3.479	1.237	7.838	4
6	4.627	1.224	3.894	1.212	9.495	3
7	4.711	1.035	4.171	1.627	8.865	4
8	4.757	1.147	4.327	1.517	9.830	4
9	5.673	1.277	8.444	3.206	18.256	5
10	6.677	1.646	15.681	5.353	36.205	6
11	6.730	1.218	16.153	7.569	30.377	7
12	6.900	1.330	17.757	7.876	34.674	6
13	7.123	1.630	20.045	7.473	43.835	8
14	7.167	1.577	20.518	7.986	43.658	9
15	7.408	1.240	23.265	11.603	41.876	9
16	7.431	1.072	23.532	13.024	39.256	10
17	7.536	1.311	24.821	12.013	45.635	10
18	7.613	1.531	25.795	10.998	51.721	10
19	7.916	1.949	29.922	10.235	69.002	11
20	8.144	1.480	33.322	15.564	62.806	12
21	8.262	1.576	35.192	15.755	68.288	12
22	8.310	1.495	35.987	16.947	67.445	12
23	8.434	1.317	38.067	19.982	66.036	12
24	9.139	1.296	51.620	28.882	85.409	13
25	9.315	1.321	55.505	31.050	91.851	14
26	9.343	1.617	56.133	27.274	102.922	14
27	9.347	1.279	56.236	32.170	91.501	15
28	10.188	1.633	77.981	40.176	137.122	16
29	10.676	1.262	93.144	57.775	142.354	17
30	10.761	1.996	96.016	44.062	183.189	17

Table 6: Results of Student's t paired tests. An "A" in a green box indicates that the null hypothesis was accepted, there the sites are deemed statistically similar. An "A" in a yellow box is simply a site being compared to itself, therefore they must be statically similar. An "R" indicates the null hypothesis has been rejected.

Site #	1	2	3	4	5	6	7	8	9	10	11	12	13	14	15	16	17	18	19	20	21	22	23	24	25	26	27	28	29	30
1	A																													
2	A	A																												
3	R	A	A																											
4	R	R	A	A																										
5	R	R	A	A	A																									
6	R	R	A	A	A	A																								
7	R	R	R	R	R	A	A																							
8	R	R	R	R	R	A	A	A																						
9	R	R	R	R	R	R	R	R	A																					
10	R	R	R	R	R	R	R	R	R	A																				
11	R	R	R	R	R	R	R	R	R	A	A																			
12	R	R	R	R	R	R	R	R	R	A	A	A																		
13	R	R	R	R	R	R	R	R	R	R	R	A	A																	
14	R	R	R	R	R	R	R	R	R	R	R	R	A	A																
15	R	R	R	R	R	R	R	R	R	R	R	R	A	A	A															
16	R	R	R	R	R	R	R	R	R	R	R	R	R	R	A	A														
17	R	R	R	R	R	R	R	R	R	R	R	R	R	R	A	A	A													
18	R	R	R	R	R	R	R	R	R	R	R	R	R	R	A	A	A	A												
19	R	R	R	R	R	R	R	R	R	R	R	R	R	R	R	R	R	R	A											
20	R	R	R	R	R	R	R	R	R	R	R	R	R	R	R	R	R	R	A	A										
21	R	R	R	R	R	R	R	R	R	R	R	R	R	R	R	R	R	R	R	A	A									
22	R	R	R	R	R	R	R	R	R	R	R	R	R	R	R	R	R	R	R	A	A	A								
23	R	R	R	R	R	R	R	R	R	R	R	R	R	R	R	R	R	R	R	A	A	A	A							
24	R	R	R	R	R	R	R	R	R	R	R	R	R	R	R	R	R	R	R	R	R	R	R	A						
25	R	R	R	R	R	R	R	R	R	R	R	R	R	R	R	R	R	R	R	R	R	R	R	A	A					
26	R	R	R	R	R	R	R	R	R	R	R	R	R	R	R	R	R	R	R	R	R	R	R	A	A	A				
27	R	R	R	R	R	R	R	R	R	R	R	R	R	R	R	R	R	R	R	R	R	R	R	A	A	A	A			
28	R	R	R	R	R	R	R	R	R	R	R	R	R	R	R	R	R	R	R	R	R	R	R	R	R	R	R	A		
29	R	R	R	R	R	R	R	R	R	R	R	R	R	R	R	R	R	R	R	R	R	R	R	R	R	R	R	R	A	
30	R	R	R	R	R	R	R	R	R	R	R	R	R	R	R	R	R	R	R	R	R	R	R	R	R	R	R	R	A	A

Table 7: Values used to estimate probability of another event happening within a particular time period. Calculations based on the Poisson Model described in Crovelli, 2000. The actual record represents the results of this study that indicated 5 events within 8400 years and the respective probabilities of another event happening in the future within different amounts of time. The hypothetical record shows how those probabilities change in the instance that the past record of events doubles.

	Record Time (t*)	Number of Events in Record Time (n)	Recurrence Interval ($\lambda = t^*/n$)	Time Period of Interest (t)	% Chance of Event Happening in Time Period of Interest ($P\{N(t) > 1\} = 1-e^{(-t/\lambda)}$)
Actual Record	8400	5	1680	1000	44.85
	8400	5	1680	100	5.78
	8400	5	1680	50	2.93
	8400	5	1680	10	0.59
	8400	5	1680	1	0.06
Hypothetical Record	8400	10	840	1000	69.59
	8400	10	840	100	11.22
	8400	10	840	50	5.77
	8400	10	840	10	1.18
	8400	10	840	1	0.11

8. References Cited

Addison, P., Oommen, T., and Sha, Q., 2019, Assessment of post-wildfire debris flow occurrence using classifier tree: Geomatics, Natural Hazards and Risk, v. 10, p. 505–518, doi:10.1080/19475705.2018.1530306.

Behl, R.J., and Kennett, J.P., 1996, Brief interstadial evets in the Santa Barbara basin, NE Pacific, during the past 60 kyr: Nature, v. 379, p. 243–246.

Best, D.W., 1989, Sediment Storage and Routing in a Steep Boulder-Bed Rock Controlled Channel Near Santa Barbara, California: Upublished M.A. Thesis, University of California, Santa Barbara.

Bierman, P.R., 1994, Using in situ produced cosmogenic isotopes to estimate rates of landscape evolution: a review from the geomorphic perspective: Journal of Geophysical Research, v. 99, doi:10.1029/94jb00459.

Bierman, P.R., Gillespie, A.R., and Caffee, M.W., 1995, Cosmogenic ages for earthquake recurrence intervals and debris flow fan deposition, Owens Valley, California: Science, v. 270, p. 447–450, doi:10.1126/science.270.5235.447.

Bierman, P., and Montgomery, D., 2014, Key Concepts in Geomorphology: W.H. Freeman and Company Publishers.

Boelhouwers, J.C., Jager, D.F., and De Joode, A., 1999, Application of relative-age dating methods to openwork debris flow deposits in the cederberg mountains, western cape, south africa: South African Geographical Journal, v. 81, p. 135–142,

doi:10.1080/03736245.1999.9713673.
Burbank, D., and Anderson, R., 2012, Tecontonic Geomorphology: Wiley-Blackwell, 46–47 p.
Cabré Cano, A., Aguilar Martorell, G., and Riquelme Salazar, R., 2017, Holocene evolution and geochronology of a semiarid fluvial system in the western slope of the Central Andes: AMS 14 C data in El Tránsito River Valley, Northern Chile: Quaternary International, v. 438, p. 20–32, doi:10.1016/j.quaint.2017.04.030.
Cannon, S.H., Gartner, J.E., Wilson, R.C., Bowers, J.C., and Laber, J.L., 2008, Storm rainfall conditions for floods and debris flows from recently burned areas in southwestern Colorado and southern California: Geomorphology, v. 96, p. 250–269, doi:10.1016/j.geomorph.2007.03.019.
Cerling, T.E., Webb, R.H., Poreda, R.J., Rigby, A.D., and Melis, T.S., 1999, Cosmogenic 3He ages and frequency of late Holocene debris flows from Prospect Canyon, Grand Canyon, USA: Geomorphology, v. 27, p. 93–111, doi:10.1016/S0169-555X(98)00092-0.
Chinn, T.J.H., 1981, Use of rock weathering-rind thickness for Holocene absolute age- dating in New Zealand.: Arctic & Alpine Research, v. 13, p. 33–45, doi:10.2307/1550624.
Colman, S.M., and Pierce, K.L., 1981, Weathering rinds on andesitic and basaltic stones as a Quaternary age indicator, western United States.: US Geological Survey, Professional Paper, v. 1210.
County of Santa Barbara, 2019, Rainfall Intensity Record:, http://www.countyofsb.org/pwd/water/downloads/hydro/234sdd.pdf (accessed April 2019).
County of Santa Barbara, 2018a, Santa Barbara County Climate:, https://www.countyofsb.org/pwd/climatology.sbc (accessed March 2020).
County of Santa Barbara, 2018b, Thomas Fire and 1/9 Debris Flow Recovery Strategic Plan, 5 June 2018:, https://www.scribd.com/document/381185041/Santa-Barbara-County-Recovery-Strategic-Plan.
Crovelli, R.A., 2000, Probability models for estimation of number and costs of landslides: U.S. Geology Survey Open File Report, v. 00, p. 23.
Day, M.J., 1980, Rock hardness: Field assessment and geomorphic importance: Professional Geographer, v. 32, p. 72–81, doi:10.1111/j.0033-0124.1980.00072.x.
Dennison, P.E., and Roberts, D.A., 2003, The effects of vegetation phenology on endmember selection and species mapping in southern California chaparral: Remote Sensing of Environment, v. 87, p. 295–309, doi:10.1016/j.rse.2003.07.001.
Dibblee, T.W., 1986a, Geologic map of the Carpenteria quadrangle, Santa Barbara County, California: Santa Barbara, Dibblee Geological Foundation Map DF-04, scale 1:24,000,.
Dibblee, T.W., 1986b, Geologic map of the Santa Barbara quadrangle, Santa Barbara County, California: Santa Barbara, Dibblee Geological Foundation Map DF-06, scale 1:24,000,.
Dibblee, T.W., 1966, Geology of the central Santa Ynez Mountains, Santa Barbara County, California: California Division of Mines and Geology, doi:978-1333155407.
DOC/NOAA/NOS/OCM, 2018, USGS Lidar: Southern CA Wildfires, produced by Department of Commerce (DOC), National Oceanic and Atmospheric Administration (NOAA), National Ocean Service (NOS), Office for Coastal Management (OCM): Charleston, SC, NOAA.:, https://coast.noaa.gov/dataviewer (accessed August 2019).

Dorn, R.I., and Jeong, A., 2018, Rock Coating and Weathering-Rind Development at the Edge of Retreating Glaciers: An Initial Study: Yearbook of the Association of Pacific Coast Geographers, v. 80, p. 66–96, doi:10.1353/pcg.2018.0004.
Dühnforth, M., Densmore, A.L., Ivy-Ochs, S., Allen, P.A., and Kubik, P.W., 2007, Timing and patterns of debris flow deposition on Shepherd and Symmes creek fans, Owens Vattey, California, deduced from cosmogenic 10Be: Journal of Geophysical Research: Earth Surface, v. 112, p. 1–11, doi:10.1029/2006JF000562.
Duvall, A., Kirby, E., and Burbank, D., 2004, Tectonic and lithologic controls on bedrock channel profiles and processes in coastal California: Journal of Geophysical Research, v. 109, p. 1–18, doi:10.1029/2003jf000086.
Ejarque, A., Anderson, R.S., Simms, A.R., and Gentry, B.J., 2015, Prehistoric fires and the shaping of colonial transported landscapes in southern California: A paleoenvironmental study at Dune Pond, Santa Barbara County: Quaternary Science Reviews, v. 112, p. 181–196, doi:10.1016/j.quascirev.2015.01.017.
Engel, J.M., Ma, L., Sak, P.B., Gaillardet, J., Ren, M., Engle, M.A., and Brantley, S.L., 2016, Quantifying chemical weathering rates along a precipitation gradient on Basse-Terre Island, French Guadeloupe: New insight from U-series isotopes in weathering rinds: Geochimica et Cosmochimica Acta, v. 195, p. 29–67, doi:10.1016/j.gca.2016.08.040.
Fath, J., Clague, J.J., and Friele, P., 2018, Influence of a large debris flow fan on the late Holocene evolution of Squamish River, southwest British Columbia, Canada: Canadian Journal of Earth Sciences, v. 55, p. 331–342, doi:10.1139/cjes-2017-0150.
Ffoulkes, C., and Harrison, S., 2014, Evaluating the schmidt hammer as a method for distinguishing the relative age of late holocene moraines: Svellnosbreen, Jotunheimen, Norway: Geografiska Annaler, Series A: Physical Geography, v. 96, p. 393–402, doi:10.1111/geoa.12055.
Finnegan, N.J., Hallet, B., Montgomery, D.R., Zeitler, P.K., Stone, J.O., Anders, A.M., and Yuping, L., 2008, Coupling of rock uplift and river incision in the Namche Barwa-Gyala Peri massif, Tibet: Bulletin of the Geological Society of America, v. 120, p. 142–155, doi:10.1130/B26224.1.
Florsheim, J.L., Keller, E.A., and Best, D.W., 1991, Fluvial sediment transport in response to moderate storm flows following chaparral wildfire, Ventura County, southern California: Geological Society of America Bulletin, v. 103, p. 504–511, doi:10.1130/0016-7606(1991)103<0504:FSTIRT>2.3.CO;2.
Gardner, T.W., Jorgensen, D.W., Shuman, C., and Lemieux, C.R., 1987, Geomorphic and tectonic process rates: effects of measured time interval.: Geology, v. 15, p. 259–261, doi:10.1130/0091-7613(1987)15<259:GATPRE>2.0.CO;2.
Gauthier, T.D., and Hawley, M.E., 2007, Statistical Methods: Introduction to Environmental Forensics, p. 129–183, doi:10.1016/b978-012369522-2/50006-3.
Gellatly, A.F., 1984, The use of rock weathering-rind thickness to redate moraines in Mount Cook National Park, New Zealand.: Arctic & Alpine Research, v. 16, p. 225–232.
Gordon, S.J., and Dorn, R.I., 2005, In situ weathering rind erosion: Geomorphology, v. 67, p. 97–113, doi:10.1016/j.geomorph.2004.06.011.
Gurrola, L., 2006, Active Tectonics and Earthquake Hazards of the Santa Barbara Fold Belt: Unpublished PhD Thesis. University of California, Santa Barbara.
Gurrola, L.D., Keller, E.A., Chen, J.H., Owen, L.A., and Spencer, J.Q., 2014, Tectonic geomorphology of marine terraces: Santa Barbara fold belt, California: Bulletin of the

Geological Society of America, v. 126, p. 219–233, doi:10.1130/B30211.1.
Gurrola, L.D., and Rogers, J.D., 2020, Flood History and Landslide Dam Hazard of the Montecito Watersheds, Santa Barbara County, California: Presentation at the Association of Environmental & Engineering Geologists 2020 Virtual Annual Meeting,.
Heusser, L.E., 1995, Pollen Stratigraphy and Paleoecologic Interpretation of the 160-k.y. Record from Santa Barbara Basin, Hole 893A: Proceedings of the Ocean Drilling Program, 146 Part 2 Scientific Results, v. 146, doi:10.2973/odp.proc.sr.146-2.279.1995.
Hunt, A.G., 2015, Predicting Rates of Weathering Rind Formation: Vadose Zone Journal, v. 14, p. 0, doi:10.2136/vzj2014.09.0123.
Hupp, C.R., Osterkamp, W.R., and Thornton, J.L., 1987, Dendrogeomorphic evidence and dating of recent debris flows on Mount Shasta, northern California: US Geological Survey Professional Paper, v. 1396 B, doi:10.3133/pp1396B.
Hurst, V.J., 1977, Visual estimation of iron in saprolite: Bulletin of the Geological Society of America, v. 88, p. 174–176, doi:10.1130/0016-7606(1977)88<174:VEOIIS>2.0.CO;2.
Kean, J.W., Staley, D.M., and Cannon, S.H., 2011, In situ measurements of post-fire debris flows in southern California: Comparisons of the timing and magnitude of 24 debris-flow events with rainfall and soil moisture conditions: Journal of Geophysical Research: Earth Surface, v. 116, p. 1–21, doi:10.1029/2011JF002005.
Kean, J.W., Staley, D.M., Lancaster, J.T., Rengers, F.K., Swanson, B.J., Coe, J.A., Hernandez, J.L., Sigman, A.J., Allstadt, K.E., and Lindsay, D.N., 2019, Inundation, flow dynamics, and damage in the 9 January 2018 Montecito debris-flow event, California, USA: Opportunities and challenges for post-wildfire risk assessment: Geosphere, v. 15, p. 1140–1163, doi:10.1130/ges02048.1.
Keaton, J.R., Anderson, L.R., and Mathewaon, C.C., 1988, Assessing debris flow hazards on alluvial fans in Davis County, Utah: in Fragaszy, R.J., ed., Twenty-Fourth Annual Symposium on Engineering Geology and Soils Engineering: Pullman, Washington, Washington State University, p. 98–108.
Keller, E., Adamaitis, C., Alessio, P., Anderson, S., Goto, E., Gray, S., Gurrola, L., and Morell, K., 2019, Applications in geomorphology: Geomorphology, doi:10.1016/j.geomorph.2019.04.001.
Keller, E., Adamaitis, C., Alessio, P., Goto, E., and Gray, S., 2020, Montecito debris flows of 9 January 2018: Physical processes and social implications: in Heermance, R.V., and Schwartz, J.J., From the Islands to the Mountains: A 2020 View of Geologic Excursions in Southern California: Geological Society of America Field Guide 59, v. 0059, p. 95–114, doi:10.1130/2020.0059(03).
Keller, E.A., Bean, G., and Best, D., 2015, Fluvial geomorphology of a boulder-bed, debris-flow - Dominated channel in an active tectonic environment: Geomorphology, v. 243, p. 14–26, doi:10.1016/j.geomorph.2015.04.012.
Keller, E.A., and DeVecchio, D.E., 2013, Tectonic Geomorphology of Active Folding and Development of Transverse Drainages: Elsevier Ltd., v. 5, 129–147 p., doi:10.1016/B978-0-12-374739-6.00088-9.
Keller, E.A., and Gurrola, L.D., 2000, U.S.G.S. National Earthquake Hazard Final report, July 2000, Earthquake hazard of the Santa Barbara Fold Belt, California:
Keller, E.A., Gurrola, L., and Tierney, T.E., 1999, Geomorphic criteria to determine direction of lateral propagation of reverse faulting and folding: Geology, v. 27, p. 515–518, doi:10.1130/0091-7613(1999)027<0515:GCTDDO>2.3.CO;2.

Keller, E.A., Valentine, D.W., and Gibbs, D.R., 1997, Hydrological Response of Small Watersheds Following the Southern California Painted Cave Fire of June 1990: Hydrological Processes, v. 11, p. 401–414, doi:10.1002/(sici)1099-1085(19970330)11:4<401::aid-hyp447>3.3.co;2-g.

Knuepfer, P.L.K., 1988, Estimating ages of late Quaternary stream terraces from analysis of weathering rinds and soils: Geological Society of America Bulletin, v. 100, p. 1224–1236, doi:10.1130/0016-7606(1988)100<1224:EAOLQS>2.3.CO;2.

Krumbein, W.C., 1941, Measurement and Geological Significance of Shape and Roundness of Sedimentary Particles: v. 11, p. 64–72.

Landis, G.P., Gurrola, L.D., Selting, A.J., and Mills-Herring, L., 2002, Evaluation of Cosmogenic 21Ne Surface Exposure Ages from a Mid-Late Pleistocene Alluvial Fan and Holocene Debris Flow, Santa Barbara, CA: Geological Society of America Abstracts with Programs, v. 34, p. 124.

Larsen, I.J., and Montgomery, D.R., 2012, Landslide erosion coupled to tectonics and river incision: Nature Geoscience, v. 5, doi:10.1038/NGEO1479.

Lavé, J., and Avouac, J.P., 2001, Fluvial incision and tectonic uplift across the Himalayas of central Nepal: Journal of Geophysical Research: Solid Earth, v. 106, p. 26561–26591, doi:10.1029/2001jb000359.

Lavé, J., and Burbank, D., 2004, Denudation processes and rates in the Transverse Ranges, southern California: Erosional response of a transitional landscape to external and anthropogenic forcing: Journal of Geophysical Research: Earth Surface, v. 109, doi:10.1029/2003jf000023.

Liebens, J., and Schaetzl, R.J., 1997, Relative-age relationships of debris flow deposits in the Southern Blue Ridge, North Carolina: Geomorphology, v. 21, p. 53–67, doi:10.1016/S0169-555X(97)00036-6.

Link, M.H., 1975, Matilija Sandstone; a transition from deep-water turbidite to shallow-marine deposition in the Eocene of California: Journal of Sedimentary Research, v. 45, p. 63–78, doi:10.1306/212f6cc6-2b24-11d7-8648000102c1865d.

Matthews, J.A., and Shakesby, R.A., 1984, The status of the 'Little Ice Age' in southern Norway: relative-age dating of Neoglacial moraines with Schmidt hammer and lichenometry: Boreas, v. 13, p. 333–346, doi:10.1111/j.1502-3885.1984.tb01128.x.

May, C.L., and Gresswell, R.E., 2004, Spatial and temporal patterns of debris-flow deposition in the Oregon Coast Range, USA: Geomorphology, v. 57, p. 135–149, doi:10.1016/S0169-555X(03)00086-2.

McGuire, L.A., Rengers, F.K., Kean, J.W., and Staley, D.M., 2017, Debris flow initiation by runoff in a recently burned basin: Is grain-by-grain sediment bulking or en masse failure to blame? Geophysical Research Letters, v. 44, p. 7310–7319, doi:10.1002/2017GL074243.

McKeever, S.W.S., 2015, Optically stimulated luminescence dosimetry: An introduction: Solid State Phenomena, v. 238, p. 161–173, doi:10.4028/www.scientific.net/SSP.238.161.

Melosh, B.L., and Keller, E.A., 2013, Effects of active folding and reverse faulting on stream channel evolution, Santa Barbara Fold Belt, California: Geomorphology, v. 186, p. 119–135, doi:10.1016/j.geomorph.2012.12.027.

Mensing, S.A., 1998, 560 Years of Vegetation Change in the Region of Santa Barbara, California: Madroño, v. 45, p. 1–11.

Mensing, S., 2015, The Paleohistory of California Oaks: In: Standiford, Richard B.; Purcell, Kathryn L., tech. cords. Proceedings of the seventh California oak symposium: managing oak woodlands in a dynamic world. Gen. Tech. Rep. PSW-GTR-251. Berkeley, CA: U.S. Department of Agriculture, Forest Service, Pacifi, p. 35–47.

Mensing, S.A., Michaelsen, J., and Byrne, R., 1999, A 560-year record of Santa Ana fires reconstructed from charcoal deposited in the Santa Barbara Basin, California: Quaternary Research, v. 51, p. 295–305, doi:10.1006/qres.1999.2035.

Minor, S., Kellogg, K., Stanley, R., Gurrola, L., Keller, E., and Brandt, T., 2009, Geologic map of the Santa Barbara coastal plain area, Santa Barbara County, California: U.S. Geological Survey Scientific Investigations Map 3001, scale 1:25,000, p. 38.

Norris, R., 2003, The Geology and Landscape of Santa Barbara County, CA and its Offshore Islands: Santa Barbara Museum of Natural History.

North, M.A., 2009, A method for implementing a statistically significant number of data classes in the Jenks algorithm: 6th International Conference on Fuzzy Systems and Knowledge Discovery, FSKD 2009, v. 1, p. 35–38, doi:10.1109/FSKD.2009.319.

Oguchi, C.T., 2013, Weathering Rinds: Formation Processes and Weathering Rates: Elsevier Ltd., v. 4, 98–110 p., doi:10.1016/B978-0-12-374739-6.00067-1.

Pazzaglia, F.J., and Brandon, M.T., 2001, A fluvial record of long-term steady state uplift and erosion across the Cascadia forearc high, western Washington State: American Journal of Science, v. 301, p. 385–431.

Reeves, D., and Rothman, D.H., 2014, Diffusion and kinetic control of weathering layer development: Geofluids, v. 14, p. 128–142, doi:10.1111/gfl.12056.

Reimer, P. et al., 2013, IntCal13 and Marine13 Radiocarbon Age Calibration Curves 0-50,000 years cal BP: Radiocarbon, v. 55, p. 1869–1887, doi:10.2458/rc.v51i4.3569.

Ricker, K.E., Chinn, T.J., and McSaveney, M.J., 1993, A late Quaternary moraine sequence dated by rock weathering rinds, Craigieburn Range, New Zealand: Canadian Journal of Earth Sciences, v. 30, p. 1861–1869, doi:10.1139/e93-164.

Rockwell, T.K., Keller, E.A., Clark, M.N., and Johnson, D.L., 1984, Chronology and rates of faulting of Ventura River terraces, California: Geological Society of America Bulletin, v. 95, p. 1466–1474.

Rodriguez, J.M., Edeskär, T., and Knutsson, S., 2013, Particle shape quantities and measurement techniques-A review: Electronic Journal of Geotechnical Engineering, v. 18 A, p. 169–198.

Sak, P.B., Fisher, D.M., Gardner, T.W., Murphy, K., and Brantley, S.L., 2004, Rates of weathering rind formation on Costa Rican basalt: Geochimica et Cosmochimica Acta, v. 68, p. 1453–1472, doi:10.1016/j.gca.2003.09.007.

Santa Barbara County, 1969, 1969 Flood Reports: Flood Control and Water Conservation District,.

Santi, P.M., deWolfe, V.G., Higgins, J.D., Cannon, S.H., and Gartner, J.E., 2008, Sources of debris flow material in burned areas: Geomorphology, v. 96, p. 310–321, doi:10.1016/j.geomorph.2007.02.022.

SCEC (Southern California Earthquake Center), 1995, Seismic hazards in southern California: probable earthquakes, 1994 to 2024: v. 85, 379–439 p., doi:10.1016/0148-9062(96)83795-8.

Schwarcz, H.., and Shane, K.., 1969, Measurement of Particle Shape By Fourier Analysis: Sedimentology, v. 13, p. 213–231, doi:10.1111/j.1365-3091.1969.tb00170.x.

Simms, A., Reynolds, L.C., Bentz, M., Roman, A., Rockwell, T., and Peters, R., 2016, Tectonic Subsidence of California Estuaries Increases Forecasts of Relative Sea-Level Rise: Estuaries and Coasts, v. 39, p. 1571–1581, doi:10.1007/s12237-016-0105-1.
Staley, D.M., Kean, J.W., Cannon, S.H., Schmidt, K.M., and Laber, J.L., 2013, Objective definition of rainfall intensity-duration thresholds for the initiation of post-fire debris flows in southern California: Landslides, v. 10, p. 547–562, doi:10.1007/s10346-012-0341-9.
Staley, D.M., Negri, J.A., Kean, J.W., Laber, J.L., Tillery, A.C., and Youberg, A.M., 2017, Prediction of spatially explicit rainfall intensity–duration thresholds for post-fire debris-flow generation in the western United States: Geomorphology, v. 278, doi:10.1016/j.geomorph.2016.10.019.
Staley, D.M., Wasklewicz, T.A., and Kean, J.W., 2014, Characterizing the primary material sources and dominant erosional processes for post-fire debris-flow initiation in a headwater basin using multi-temporal terrestrial laser scanning data: Geomorphology, v. 214, p. 324–338, doi:10.1016/j.geomorph.2014.02.015.
State of California, 2013, California's Flood Future: Recommendations for Managing the State's Flood Risk; Appendices A through F,.
Stauffer, P.H., 1967, Grain-Flow Deposits and their Implications, Santa Ynez Mountains, California: SEPM Journal of Sedimentary Research, v. Vol. 37, doi:10.1306/74d716f9-2b21-11d7-8648000102c1865d.
Stuiver, M., and Reimer, P.J., 1993, Radiocarbon: v. 35, p. 215–230.
Stuiver, M., Reimer, P.J., and Reimer, R.W., 2017, CALIB 7.1 [www program]:, http://calib.org (accessed February 2020).
United States Geological Survey (USGS), 2016, Debris - Flow Hazards in the United States:, http://pubs.usgs.gov/fs/fs-176-97/fs-176-97.html.
United States Geological Survey and California Geological Survey Quaternary fault and fold database for the United States:, https://www.usgs.gov/natural-hazards/earthquake-hazards/faults. (accessed July 2020).
Urban, R.J., 2004, The Mission Diamicton and Associated Geohazards Santa Barbara , California: Upublished MS Thesis. San Jose State University, http://scholarworks.sjsu.edu/etd_theses/2570.
US Army Corps of Engineers Los Angeles District, 1999, Santa Barbara County Streams, Lower Mission Creek Flood Control Feasibility Study:
Warrick, J.A., and Mertes, L.A.K., 2009, Sediment yield from the tectonically active semiarid Western Transverse Ranges of California: Bulletin of the Geological Society of America, v. 121, p. 1054–1070, doi:10.1130/B26452.1.
Warrick, J.A., Mertes, L.A.K., Washburn, L., and Siegel, D.A., 2004, A conceptual model for river water and sediment dispersal in the Santa Barbara Channel, California: Continental Shelf Research, v. 24, p. 2029–2043, doi:10.1016/j.csr.2004.07.010.
Winchester, V., and Harrison, S., 1994, A development of the lichenometric method applied to the dating of glacially influenced debris flows in southern chile: Earth Surface Processes and Landforms, v. 19, p. 137–151, doi:10.1002/esp.3290190205.
Yoshida, H., Metcalfe, R., Nishimoto, S., Yamamoto, H., and Katsuta, N., 2011, Weathering rind formation in buried terrace cobbles during periods of up to 300ka: Applied Geochemistry, v. 26, p. 1706–1721, doi:10.1016/j.apgeochem.2011.04.027.
Youberg, A.M., Webb, R.H., Fenton, C.R., and Pearthree, P.A., 2014, Latest Pleistocene-

Holocene debris flow activity, Santa Catalina Mountains, Arizona; Implications for modern debris-flow hazards under a changing climate: Geomorphology, v. 219, p. 87–102, doi:10.1016/j.geomorph.2014.04.034.

9. Appendix

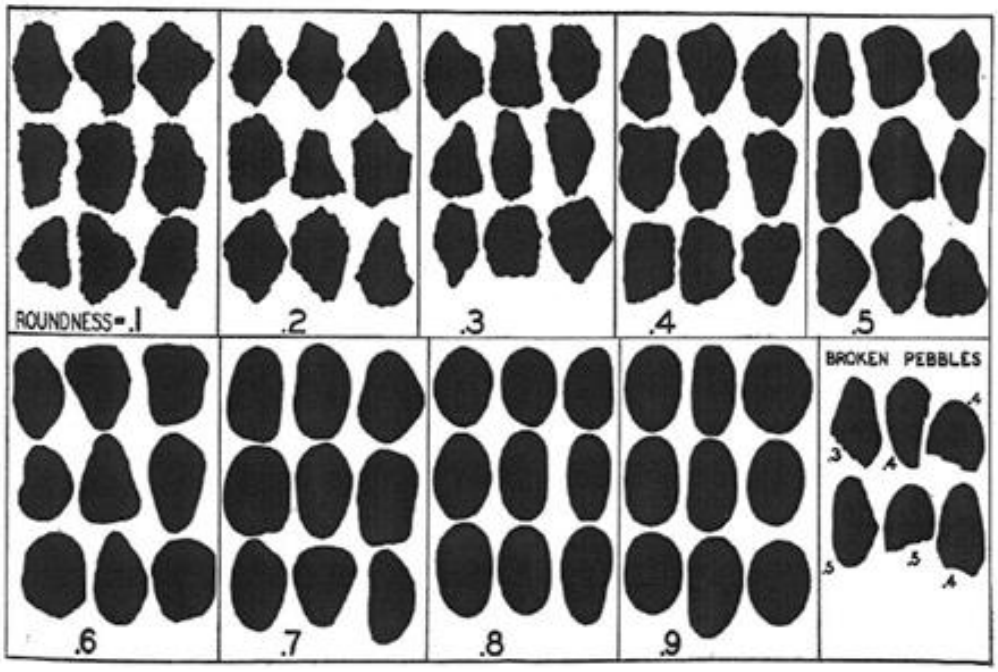

Figure A1: Krumbein (1941) comparison chart used to assign relative roundness values to boulders of debris flow deposits.

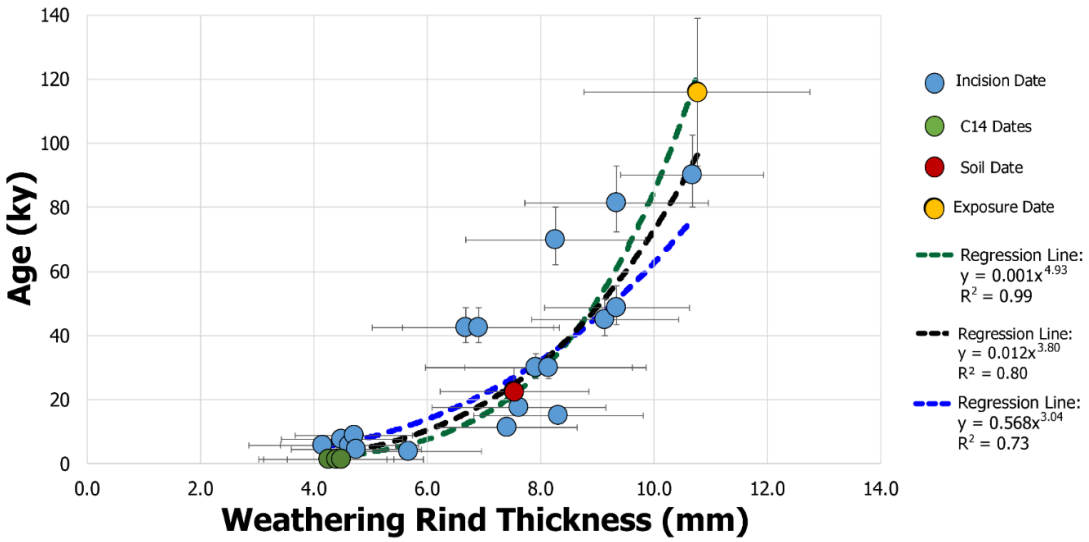

Figure A2: Calibration curves of average weathering rind thickness of the boulders where each numeric age was estimated vs numeric age. Three different regression lines are shown, which correlate weathering rind thickness to ages found using just radiocarbon, soil and exposure analysis (green dashed line); all forms of dating (black dashed line); and just the dates found using incision rates (blue dashed line). Color of data point indicates the type of numeric age. Horizontal error bars are +/- 1 standard deviation of the weathering rind thicknesses of each site. Vertical error bars represent age control for each type of numeric dating method found using the black regression line – the one ultimately used for the analysis of this study. This graph aims to show the suitability of using incision rates to assign ages.

Table A1: Radiocarbon information for samples collected at sites 2 and 3.

		Fraction of Modern		Radiocarbon Age		Calib 7	
Sample	Location	pMC	1sigma error	BP	1 sigma error	Cal BP	Peak Probability
C-5	Site 2	83.41	0.12	1457	21	1314-1357	1343
C-15	Site 3	81.68	0.29	1626	29	1520-1560	1529

Table A2: Raw data per boulder for each site. Table gives information on weathering rind thickness (WRT), Schmidt Hammer rebound value (SH (R)), roundness value, values that calculate the color index (hue, value, and chroma), elevation above sea level, and the coordinates for each measured boulder.

Site #	Boul-der #	Avg WRT (mm)	Avg SH (R)	Round-ness Value	Hue	Value	Chroma	H*	Color Index	Elevation Above Sea Level (m)	Easting (m)	Northing (m)
Site 1	1	3.026	29.6	0.50	5YR	5	8	15	75.0	63.3	249690.5	3813998.6
	2	3.828	37.5	0.50	5Y	6	2	25	150.0	63.5	249695.2	3813996.2
	3	3.861	28.4	0.45	5Y	6	2	25	150.0	63.4	249694.3	3813995.1
	4	5.319	24.7	0.50	5Y	6	2	25	150.0	63.2	249694.8	3813991.1
	5	3.934	34.3	0.60	5Y	6	2	25	150.0	63.4	249692.6	3813998.9
	6	3.685	36.6	0.50	5Y	6	2	25	150.0	63.4	249689.5	3814002.4
	7	5.051	39.0	0.55	5YR	6	6	15	90.0	64.0	249668.2	3814036.5
	8	4.125	38.8	0.55	5YR	6	6	15	90.0	65.0	249672.3	3814073.0
	9	4.034	36.2	0.55	5YR	6	6	15	90.0	65.2	249674.4	3814076.6
	10	4.314	39.6	0.55	5YR	5	4	15	75.0	65.2	249673.5	3814079.3
	11	4.702	36.3	0.60	5Y	6	2	25	150.0	65.7	249675.8	3814062.3
	12	3.993	37.4	0.50	5Y	6	2	25	150.0	65.8	249673.8	3814060.0
Site 2	1	3.055		0.60	5YR	6	6	15	90.0	6.4	257575.1	3811467.5
	2	5.290		0.60	5YR	7	6	15	105.0	6.1	257567.9	3811559.5
	3	4.320		0.70	5Y	8	3	25	200.0	7.2	257588.1	3811571.7
	4	4.376		0.60	5Y	8	4	25	200.0	10.5	257600.2	3811629.9
	5	3.307		0.50	5YR	8	3	15	120.0	10.2	257605.5	3811626.7
	6	4.382		0.60	5Y	6	3	25	150.0	12.6	257605.5	3811637.8
	7	4.903		0.60	5Y	4	1	25	100.0	12.2	257604.4	3811643.1
	8	4.287		0.60	5Y	8	3	25	200.0	11.0	257590.6	3811654.7
	9	4.568		0.60	5Y	8	2	25	200.0	13.1	257615.7	3811664.4
	10	4.607		0.55	5Y	8	4	25	200.0	12.8	257618.6	3811658.4
	11	4.395		0.60	5Y	8	3	25	200.0	13.6	257620.4	3811663.6
	12	4.490		0.65	5Y	8	3	25	200.0	14.1	257623.8	3811669.1
	13	4.548		0.50	5Y	7	2	25	175.0	8.8	257560.2	3811629.1
	14	3.271		0.45	5Y	8	2	25	200.0	7.5	257535.7	3811630.8
	15	4.120		0.55	5Y	8	2	25	200.0	8.0	257556.7	3811601.7
Site 3	1	4.441	34.8	0.50	10R	4	3	10	40.0	286.0	259054.7	3816222.5
	2	4.269	32.6	0.55	5Y	6	1	25	150.0	286.9	259062.1	3816213.0
	3	3.946	39.7	0.55	5YR	7	2	15	105.0	286.9	259046.2	3816238.6
	4	3.982	41.5	0.60	7.5YR	7	4	17.5	122.5	284.2	259046.1	3816219.0
	5	4.716	43.8	0.50	7.5YR	7	4	17.5	122.5	284.2	259047.1	3816213.6
	6	4.385	40.3	0.45	7.5YR	7	4	17.5	122.5	281.9	259056.3	3816172.1
	7	4.957	40.7	0.55	5Y	6	1	25	150.0	278.6	259069.7	3816152.7
	8	4.108	37.9	0.50	5Y	6	1	25	150.0	293.7	259045.4	3816290.9
	9	4.481	40.1	0.45	5Y	6	2	25	150.0	291.7	259030.1	3816284.1

	10	4.693	45.4	0.50	5Y	6	2	25	150.0	291.3	259029.7	3816281.6
	11	4.636	41.2	0.50	5YR	7	1	15	105.0	289.1	259025.4	3816277.6
	12	3.919	46.8	0.50	5YR	7	1	15	105.0	288.4	259025.5	3816275.1
	13	4.631	32.6	0.55	5Y	6	2	25	150.0	288.2	259026.3	3816273.3
	14	4.260	45.5	0.40	5Y	4	1	25	100.0	290.5	259032.8	3816272.1
	15	4.668	44.0	0.55	5Y	6	2	25	150.0	290.4	259036.6	3816267.2
Site 4	1	4.566	37.0	0.50	5Y	4	1	25	100.0	103.5	250765.0	3814407.6
	2	4.626	40.1	0.60	5Y	5	1	25	125.0	103.6	250770.9	3814406.1
	3	4.769	42.6	0.60	5Y	4	1	25	100.0	103.9	250771.5	3814416.0
	4	4.058	34.6	0.45	5Y	6	2	25	150.0	103.9	250767.3	3814425.5
	5	3.978	29.5	0.70	5Y	6	2	25	150.0	104.3	250765.5	3814433.4
	6	4.136	41.7	0.55	5Y	4	2	25	100.0	103.8	250762.2	3814432.0
	7	4.997	34.0	0.55	5Y	3	1	25	75.0	103.7	250765.7	3814421.6
	8	3.289	44.6	0.65	5Y	4	1	25	100.0	103.5	250765.1	3814415.8
	9	4.122	40.6	0.55	5Y	5	1	25	125.0	103.3	250760.0	3814419.4
	10	4.592	31.5	0.65	5Y	4	1	25	100.0	103.2	250758.9	3814415.1
	11	4.074	44.3	0.60	5Y	5	4	25	125.0	102.9	250757.4	3814412.6
	12	4.764	39.5	0.50	5Y	4	1	25	100.0	103.5	250759.3	3814424.3
	13	4.897	41.3	0.60	5Y	4	1	25	100.0	103.4	250757.2	3814427.4
	14	4.996	42.0	0.55	5Y	5	3	25	125.0	103.2	250751.2	3814426.6
	15	4.183	36.0	0.50	5Y	5	4	25	125.0	103.4	250757.2	3814432.1
	16	4.335	37.3	0.50	5Y	6	1	25	150.0	103.8	250762.6	3814428.3
	17	5.159	37.0	0.60	5Y	5	1	25	125.0	103.7	250761.0	3814434.5
	18	4.991	39.0	0.60	5Y	3	1	25	75.0	105.0	250782.8	3814430.5
	19	4.762	44.9	0.55	5Y	4	1	25	100.0	105.0	250779.9	3814433.5
	20	4.471	34.0	0.50	5Y	4	1	25	100.0	105.4	250782.9	3814436.0
Site 5	1	4.576	32.5	0.55	10YR	5	2	20	100.0	85.7	250289.7	3814339.6
	2	4.285	36.0	0.45	10YR	3	1	20	60.0	85.9	250293.5	3814339.2
	3	3.814	35.3	0.50	10YR	6	1	20	120.0	86.2	250294.8	3814341.8
	4	3.868	26.6	0.50	10YR	5	2	20	100.0	86.1	250295.1	3814343.0
	5	4.515	35.8	0.45	10YR	6	1	20	120.0	85.9	250288.8	3814344.5
	6	4.034	24.2	0.50	10YR	6	3	20	120.0	85.7	250281.0	3814341.3
	7	4.957	34.4	0.45	5YR	7	2	15	105.0	85.7	250280.2	3814341.3
	8	4.712	35.2	0.50	10YR	6	2	20	120.0	85.6	250270.8	3814350.5
	9	4.773	28.6	0.55	10YR	3	1	20	60.0	86.0	250282.5	3814357.8
	10	5.165	34.8	0.55	10YR	6	3	20	120.0	86.1	250281.3	3814359.1
	11	4.163	35.6	0.60	10YR	6	3	20	120.0	86.3	250290.4	3814365.6
	12	4.899	38.0	0.50	10YR	7	4	20	140.0	86.3	250289.8	3814375.5
	13	4.905	28.3	0.50	10YR	6	1	20	120.0	86.5	250291.3	3814378.4
	14	3.682	37.0	0.45	10YR	6	1	20	120.0	85.9	250286.8	3814380.9
	15	5.026	26.1	0.45	5Y	6	2	25	150.0	85.7	250283.2	3814387.5
Site 6	1	5.220		0.60	5YR	6	6	15	90.0	20.6	257791.1	3812272.2

	2	4.030		0.60	10R	5	6	10	50.0	20.7	257782.2	3812277.2
	3	4.630		0.55	5Y	7	4	25	175.0	21.2	257788.4	3812301.7
Site 7	1	4.606	41.4	0.45	7.5YR	3	0	17.5	52.5	103.7	250771.7	3814408.2
	2	4.249	31.6	0.45	5Y	5	1	25	125.0	104.2	250768.5	3814426.8
	3	4.865	30.8	0.50	7.5YR	3	0	17.5	52.5	105.1	250778.6	3814439.3
	4	4.432	31.8	0.50	5YR	4	3	15	60.0	105.3	250782.9	3814434.2
	5	4.707	32.6	0.60	5Y	5	1	25	125.0	106.1	250793.3	3814459.2
	6	5.160	25.7	0.50	5Y	4	1	25	100.0	106.7	250798.7	3814487.0
	7	4.081	27.6	0.50	5Y	7	1	25	175.0	107.5	250802.3	3814505.7
	8	4.250	34.1	0.50	5Y	6	3	25	150.0	108.0	250806.8	3814511.4
	9	4.214	35.1	0.50	5Y	3	0	25	75.0	111.6	250835.9	3814601.8
	10	4.608	31.9	0.55	7.5YR	3	0	17.5	52.5	111.6	250839.7	3814603.5
	11	4.480	38.2	0.60	5Y	4	1	25	100.0	115.5	250899.5	3814651.9
	12	5.244	38.4	0.60	10R	5	2	10	50.0	117.2	250932.8	3814675.5
	13	5.129	40.7	0.60	7.5YR	6	6	17.5	105.0	119.6	250967.0	3814699.6
	14	4.944	38.0	0.60	5Y	6	2	25	150.0	120.3	250979.7	3814748.5
	15	5.347	37.1	0.55	5Y	5	1	25	125.0	124.5	250972.6	3814816.8
	16	5.182	38.4	0.50	10R	3	1	10	30.0	123.8	251024.2	3814761.4
	17	4.242	32.8	0.55	5Y	4	1	25	100.0	121.8	251021.0	3814725.6
	18	5.404	21.5	0.45	10R	3	2	10	30.0	118.8	250977.6	3814684.6
	19	4.410	37.4	0.55	10R	6	3	10	60.0	119.0	250975.4	3814688.2
	20	4.675	39.0	0.55	10R	4	2	10	40.0	118.4	250969.5	3814678.7
Site 8	1	4.397	39.3	0.50	5Y	5	1	25	125.0	47.3	249347.5	3813326.7
	2	5.447	38.7	0.60	5Y	5	1	25	125.0	47.2	249340.9	3813320.8
	3	4.466	36.5	0.65	5Y	5	1	25	125.0	47.0	249331.0	3813311.5
	4	4.499	37.8	0.50	5Y	5	1	25	125.0	47.0	249331.0	3813308.1
	5	4.838	42.2	0.65	5Y	5	1	25	125.0	44.1	249328.2	3813262.8
	6	4.897	37.0	0.55	5Y	7	1	25	175.0	48.2	249389.3	3813368.5
Site 9	1	6.862	29.5	0.50	5Y	6	2	25	150.0	85.3	248740.0	3815263.1
	2	5.469	31.8	0.50	5Y	6	2	25	150.0	85.1	248738.5	3815257.0
	3	6.105	29.1	0.55	5Y	4	2	25	100.0	84.6	248746.1	3815252.5
	4	5.646	30.1	0.55	5Y	3	1	25	75.0	84.6	248745.4	3815250.4
	5	6.113	37.1	0.60	5Y	4	1	25	100.0	84.4	248743.1	3815245.6
	6	5.944	33.3	0.60	5Y	5	1	25	125.0	84.9	248736.5	3815251.2
	7	5.003	34.6	0.55	5Y	4	1	25	100.0	82.8	248738.7	3815210.0
	8	5.549	33.2	0.50	5Y	5	4	25	125.0	83.7	248747.7	3815221.8
	9	4.712	22.4	0.65	5Y	4	1	25	100.0	84.6	248749.4	3815252.3
	10	5.066	34.2	0.60	5Y	4	1	25	100.0	82.6	248753.9	3815263.9
	11	5.642	31.1	0.55	5Y	5	3	25	125.0	84.5	248747.4	3815276.2
	12	5.966	32.2	0.50	5Y	5	4	25	125.0	86.8	248736.7	3815287.4
Site 10	1	6.633	22.1	0.60	10YR	7	6	20	140.0	221.4	251158.8	3815899.8
	2	6.975	26.0	0.55	10YR	7	6	20	140.0	221.2	251156.7	3815893.6

	3	6.287	23.2	0.55	10YR	6	6	20	120.0	221.2	251160.2	3815883.8
	4	6.488	30.1	0.50	10R	4	4	10	40.0	216.0	251163.1	3815856.9
	5	6.374	25.7	0.60	10R	5	3	10	50.0	210.1	251176.3	3815833.7
	6	6.429	25.8	0.55	10YR	5	4	20	100.0	210.2	251178.2	3815834.9
	7	6.898	30.6	0.60	10R	5	3	10	50.0	216.7	251144.6	3815889.3
	8	7.115	24.8	0.60	10R	5	3	10	50.0	216.2	251144.6	3815878.3
	9	6.897	24.1	0.50	10YR	6	3	20	120.0	215.3	251151.0	3815864.0
Site 11	1	6.649	37.8	0.50	7.5YR	4	0	17.5	70.0	164.7	262955.8	3813694.5
	2	6.435	34.9	0.55	7.5YR	6	0	17.5	105.0	164.2	262950.9	3813689.8
	3	7.536	34.1	0.50	7.5YR	5	0	17.5	87.5	158.6	262891.0	3813630.1
	4	7.131	34.5	0.50	7.5YR	4	0	17.5	70.0	158.3	262886.8	3813629.0
	5	7.620	37.4	0.55	7.5YR	6	0	17.5	105.0	156.4	262887.6	3813605.5
	6	6.993	35.6	0.50	7.5YR	5	0	17.5	87.5	157.4	262932.8	3813591.1
	7	6.642	38.6	0.65	7.5YR	5	0	17.5	87.5	159.5	262944.5	3813610.1
	8	6.719	35.5	0.55	7.5YR	6	0	17.5	105.0	159.6	262939.5	3813611.0
	9	6.927	27.1	0.55	7.5YR	5	0	17.5	87.5	159.0	262937.0	3813607.4
	10	6.205	24.9	0.65	7.5YR	5	0	17.5	87.5	158.9	262929.0	3813608.1
	11	6.172	20.5	0.60	7.5YR	6	0	17.5	105.0	160.9	262941.7	3813629.8
	12	6.882	23.8	0.55	7.5YR	5	0	17.5	87.5	164.6	262921.6	3813708.7
	13	6.768	30.7	0.55	7.5YR	5	0	17.5	87.5	166.1	262905.7	3813727.7
	14	6.342	35.5	0.55	7.5YR	6	0	17.5	105.0	165.5	262929.4	3813714.9
	15	5.790	33.9	0.50	7.5YR	5	0	17.5	87.5	168.9	262951.1	3813738.4
	16	7.362	29.8	0.55	7.5YR	6	0	17.5	105.0	169.2	262950.4	3813741.3
	17	7.015	28.2	0.55	7.5YR	5	0	17.5	87.5	169.6	262950.1	3813743.4
	18	6.303	27.4	0.55	7.5YR	4	0	17.5	70.0	170.1	262958.6	3813742.7
	19	6.309	20.3	0.50	7.5YR	5	0	17.5	87.5	173.2	262960.4	3813784.4
	20	6.796	23.4	0.60	7.5YR	5	0	17.5	87.5	174.0	262965.4	3813790.4
Site 12	1	6.605	28.7	0.60	10R	6	2	10	60.0	262.4	252256.3	3816156.6
	2	7.555	29.4	0.55	10YR	7	6	20	140.0	262.1	252262.3	3816154.8
	3	7.236	30.9	0.50	5YR	3	1	15	45.0	262.4	252262.8	3816159.2
	4	7.349	27.7	0.55	5YR	7	4	15	105.0	265.5	252265.6	3816162.0
	5	6.679	22.1	0.45	5YR	5	2	15	75.0	265.4	252263.3	3816166.8
	6	7.131	28.0	0.55	5YR	6	4	15	90.0	265.4	252266.3	3816160.3
	7	6.614	32.9	0.60	5YR	6	2	15	90.0	265.4	252268.2	3816157.7
	8	6.338	27.7	0.50	5YR	5	2	15	75.0	263.7	252266.1	3816155.4
	9	7.229	29.5	0.50	10YR	6	3	20	120.0	260.9	252261.5	3816150.1
	10	6.262	24.0	0.45	10R	5	2	10	50.0	260.5	252248.9	3816144.7
Site 13	1	6.282	37.6	0.60	5YR	5	4	15	75.0	121.7	250693.9	3814980.6
	2	7.320	36.1	0.50	5YR	5	4	15	75.0	121.7	250699.1	3814973.9
	3	7.309	42.8	0.55	5YR	5	4	15	75.0	121.2	250701.2	3814959.9
	4	7.362	37.7	0.60	5YR	6	6	15	90.0	121.2	250694.8	3814970.4
	5	7.358	36.6	0.60	5YR	5	4	15	75.0	121.5	250698.6	3814966.7

	6	6.339	30.6	0.65	5YR	5	4	15	75.0	120.6	250685.0	3814973.8
	7	7.387	37.0	0.70	5YR	5	4	15	75.0	121.8	250701.0	3814970.1
	8	8.052	28.9	0.50	5YR	5	4	15	75.0	122.4	250702.5	3814982.6
	9	6.858	32.4	0.50	5YR	6	6	15	90.0	121.0	250684.8	3814985.8
	10	6.970	35.7	0.65	5YR	5	4	15	75.0	122.0	250694.9	3814987.7
Site 14	1	8.007	37.6	0.50	5YR	5	4	15	75.0	215.2	255860.0	3815479.5
	2	7.994	34.1	0.50	5Y	5	2	25	125.0	214.8	255859.7	3815475.2
	3	8.049	34.5	0.45	5YR	5	4	15	75.0	214.8	255860.7	3815474.6
	4	7.183	32.5	0.55	5Y	3	2	25	75.0	213.7	255863.0	3815465.1
	5	7.294	30.4	0.60	10YR	6	3	20	120.0	211.2	255861.2	3815453.2
	6	7.863	24.7	0.55	10YR	5	6	20	100.0	211.4	255864.9	3815454.4
	7	8.220	26.5	0.65	10R	4	2	10	40.0	211.8	255862.9	3815455.9
	8	6.901	33.4	0.60	10R	6	6	10	60.0	210.5	255846.1	3815455.0
	9	7.275	30.3	0.55	5Y	6	2	25	150.0	215.0	255854.2	3815489.5
	10	6.625	28.3	0.45	10R	4	3	10	40.0	215.0	255855.6	3815489.6
	11	6.245	27.2	0.55	5Y	7	3	25	175.0	214.6	255857.4	3815488.2
	12	5.751	28.5	0.55	10YR	5	3	20	100.0	216.0	255862.1	3815499.5
	13	7.265	20.1	0.60	10YR	5	2	20	100.0	223.8	255873.2	3815543.7
	14	6.793	30.0	0.65	5Y	6	2	25	150.0	222.1	255893.7	3815530.5
	15	7.835	33.1	0.60	5Y	6	2	25	150.0	222.4	255898.7	3815527.6
	16	5.983	40.5	0.60	10R	6	2	10	60.0	222.6	255899.4	3815529.4
	17	6.039	28.2	0.50	10R	5	4	10	50.0	222.5	255900.7	3815528.1
	18	7.468	28.9	0.50	5Y	6	2	25	150.0	219.9	255898.6	3815509.9
	19	7.149	32.8	0.60	5Y	6	2	25	150.0	219.0	255901.4	3815505.8
	20	7.410	38.1	0.55	5Y	6	2	25	150.0	218.7	255900.4	3815503.3
Site 15	1	7.889	27.3	0.45	5Y	3	1	25	75.0	185.9	255763.4	3815085.9
	2	7.345	26.8	0.55	10R	3	1	10	30.0	186.6	255760.5	3815099.6
	3	6.581	26.8	0.50	10R	5	2	10	50.0	187.6	255745.3	3815110.1
	4	7.548	30.4	0.55	5Y	7	2	25	175.0	188.2	255745.0	3815120.9
	5	7.657	28.9	0.55	5Y	7	2	25	175.0	188.2	255742.4	3815117.3
	6	6.980	22.1	0.45	5Y	5	3	25	125.0	187.9	255745.7	3815114.1
	7	7.795	26.5	0.55	5Y	3	1	25	75.0	186.8	255746.6	3815093.5
	8	7.376	22.2	0.55	5Y	5	1	25	125.0	186.2	255754.4	3815091.2
	9	7.507	25.0	0.60	5YR	5	4	15	75.0	185.7	255766.1	3815085.3
Site 16	1	7.547	26.5	0.50	7.5YR	6	0	17.5	105.0	202.0	252783.0	3814673.4
	2	7.767	27.0	0.55	7.5YR	5	0	17.5	87.5	200.2	252784.4	3814686.7
	3	7.017	26.1	0.60	7.5YR	5	0	17.5	87.5	198.6	252798.9	3814687.5
	4	7.352	28.7	0.50	7.5YR	5	0	17.5	87.5	197.4	252802.8	3814693.0
	5	7.743	27.9	0.60	7.5YR	7	0	17.5	122.5	200.6	252805.2	3814671.6
	6	7.394	24.3	0.65	7.5YR	7	0	17.5	122.5	200.2	252811.5	3814679.3
	7	6.705	26.7	0.65	7.5YR	7	0	17.5	122.5	200.6	252817.2	3814677.7
	8	7.749	21.7	0.55	7.5YR	6	2	17.5	105.0	200.3	252820.7	3814679.7

	9	7.344	22.3	0.60	7.5YR	6	2	17.5	105.0	197.8	252837.9	3814689.4
	10	7.417	26.0	0.60	7.5YR	6	2	17.5	105.0	197.3	252833.3	3814693.1
	11	7.287	27.2	0.55	5YR	7	3	15	105.0	201.9	252831.3	3814669.7
	12	7.478	29.8	0.60	5YR	7	3	15	105.0	203.1	252831.1	3814663.5
	13	7.440	25.0	0.65	7.5YR	6	4	17.5	105.0	205.0	252833.1	3814653.6
	14	7.915	27.6	0.55	7.5YR	6	4	17.5	105.0	195.0	252817.7	3814708.5
	15	7.100	29.5	0.55	5YR	5	1	15	75.0	195.6	252817.4	3814705.3
	16	7.464	23.1	0.50	5YR	5	2	15	75.0	196.5	252814.2	3814700.3
	17	7.423	25.0	0.60	7.5YR	6	4	17.5	105.0	197.3	252811.3	3814695.8
	18	8.029	28.0	0.55	7.5YR	5	4	17.5	87.5	198.7	252782.4	3814699.5
	19	7.041	29.3	0.60	7.5YR	5	4	17.5	87.5	198.9	252784.6	3814696.1
	20	7.405	26.8	0.55	5Y	6	2	25	150.0	199.1	252776.9	3814701.8
Site 17	1	8.120	35.1	0.55	5YR	5	6	15	75.0	363.3	253097.0	3816938.4
	2	8.160	29.5	0.50	5YR	5	6	15	75.0	366.7	253096.0	3816944.2
	3	7.640	36.2	0.45	7.5YR	6	0	17.5	105.0	363.3	253101.9	3816946.3
	4	7.290	38.5	0.55	5YR	5	3	15	75.0	369.2	253114.7	3816966.2
	5	7.480	24.8	0.50	5YR	5	3	15	75.0	370.6	253107.5	3816964.8
	6	7.220	33.0	0.55	5YR	5	3	15	75.0	367.5	253104.8	3816954.2
	7	6.840	40.2	0.50	7.5YR	5	0	17.5	87.5	365.8	253103.8	3816951.5
Site 18	1	7.901	30.0	0.60	10YR	6	6	20	120.0	272.8	252657.4	3816200.5
	2	6.932	33.9	0.55	10YR	5	3	20	100.0	276.6	252660.7	3816202.6
	3	7.611	34.7	0.55	10YR	4	1	20	80.0	273.7	252666.0	3816199.7
	4	7.992	36.5	0.50	10R	5	3	10	50.0	272.8	252659.5	3816191.2
	5	7.436	31.9	0.55	5Y	5	3	25	125.0	272.6	252655.6	3816191.2
	6	8.075	33.7	0.55	5Y	5	3	25	125.0	275.8	252653.1	3816191.7
	7	7.592	32.7	0.55	5Y	5	3	25	125.0	274.1	252654.9	3816190.6
	8	8.173	29.4	0.50	10R	4	2	10	40.0	276.4	252645.4	3816189.9
	9	7.521	28.7	0.50	10YR	5	2	20	100.0	275.1	252642.0	3816185.5
	10	6.915	35.7	0.55	5Y	4	1	25	100.0	277.0	252640.5	3816189.6
	11	8.913	31.7	0.65	5Y	7	3	25	175.0	278.5	252645.6	3816195.1
	12	7.632	28.6	0.60	5Y	7	3	25	175.0	278.7	252642.0	3816195.4
	13	7.766	27.4	0.50	5Y	4	1	25	100.0	277.4	252636.1	3816189.0
	14	5.746	33.9	0.50	10YR	7	3	20	140.0	274.3	252637.3	3816182.2
	15	8.205	36.6	0.55	5YR	5	4	15	75.0	272.8	252640.8	3816177.4
	16	7.395	33.1	0.50	5YR	5	4	15	75.0	272.6	252653.8	3816186.4
Site 19	1	8.351	36.5	0.50	5YR	6	3	15	90.0	231.3	251051.8	3816276.5
	2	7.426	37.7	0.60	5YR	6	4	15	90.0	231.0	251053.5	3816271.9
	3	6.274	34.2	0.60	5Y	4	1	25	100.0	230.1	251055.4	3816262.2
	4	8.334	37.7	0.55	5Y	5	2	25	125.0	229.9	251055.7	3816254.4
	5	8.796	36.6	0.60	5Y	5	2	25	125.0	229.5	251056.0	3816247.4
	6	7.793	30.6	0.50	5Y	7	3	25	175.0	228.9	251058.8	3816242.5
	7	6.979	37.0	0.55	5YR	6	4	15	90.0	229.2	251055.7	3816237.8

	8	7.731	28.9	0.55	5YR	5	4	15	75.0	228.8	251054.1	3816232.6
	9	8.635	32.4	0.50	5YR	5	4	15	75.0	227.7	251063.2	3816232.5
	10	8.298	35.7	0.60	5YR	5	4	15	75.0	227.3	251063.1	3816225.3
	11	9.143	31.8	0.55	5YR	6	3	15	90.0	226.8	251055.0	3816216.0
	12	7.801	32.7	0.60	5YR	5	3	15	75.0	225.3	251056.2	3816198.7
	13	8.911	34.4	0.50	5YR	5	3	15	75.0	223.0	251048.6	3816212.9
	14	6.621	33.6	0.60	5YR	6	6	15	90.0	223.1	251046.7	3816217.9
	15	7.583	43.4	0.60	5YR	6	6	15	90.0	223.2	251046.4	3816219.0
	16	8.447	42.4	0.65	5YR	6	6	15	90.0	221.8	251042.2	3816229.5
	17	7.393	37.0	0.50	5Y	6	4	25	150.0	220.5	251036.0	3816242.3
	18	7.976	37.1	0.55	5YR	6	4	15	90.0	222.8	251031.6	3816269.1
Site 20	1	8.775	25.4	0.55	10R	4	2	10	40.0	243.3	252158.6	3816087.1
	2	7.041	43.9	0.55	10R	3	2	10	30.0	243.4	252156.4	3816086.4
	3	9.170	31.2	0.60	10R	6	2	10	60.0	243.0	252160.4	3816085.2
	4	7.880	20.8	0.50	10R	3	2	10	30.0	243.2	252157.3	3816085.1
	5	8.551	29.3	0.60	10R	3	2	10	30.0	242.6	252155.4	3816079.5
	6	7.330	31.5	0.55	10R	6	2	10	60.0	242.2	252154.5	3816077.5
	7	8.147	28.4	0.55	7.5YR	7	4	17.5	122.5	242.3	252152.5	3816077.8
	8	7.835	32.0	0.60	7.5YR	6	4	17.5	105.0	241.6	252162.9	3816074.2
	9	8.409	26.7	0.55	5Y	6	1	25	150.0	242.5	252163.7	3816083.0
	10	8.260	27.0	0.50	7.5YR	7	3	17.5	122.5	242.2	252161.1	3816079.5
	11	8.229	38.7	0.60	10R	3	2	10	30.0	246.5	252165.4	3816113.0
	12	8.099	30.8	0.55	5YR	5	1	15	75.0	246.2	252168.8	3816117.4
Site 21	1	8.950	23.5	0.55	5YR	7	6	15	105.0	283.8	252319.6	3815686.0
	2	9.176	31.1	0.40	7.5YR	7	6	17.5	122.5	283.9	252317.9	3815688.2
	3	9.035	27.8	0.50	5YR	5	6	15	75.0	285.1	252331.9	3815690.4
	4	9.056	31.7	0.40	5Y	5	4	25	125.0	285.4	252333.4	3815692.6
	5	8.200	38.8	0.50	5Y	2.5	1	25	62.5	285.6	252335.2	3815694.8
	6	8.958	32.3	0.40	5YR	6	3	15	90.0	287.3	252323.3	3815712.4
	7	8.816	34.9	0.45	5Y	2.5	1	25	62.5	287.8	252338.6	3815710.9
	8	8.407	30.0	0.40	10R	3	6	10	30.0	287.5	252344.5	3815699.5
	9	7.934	31.0	0.40	5YR	5	2	15	75.0	286.7	252342.9	3815696.3
	10	7.704	33.2	0.60	5YR	5	1	15	75.0	286.4	252343.9	3815694.5
	11	7.919	36.5	0.40	5YR	5	1	15	75.0	287.3	252349.6	3815695.1
	12	7.512	30.0	0.40	10R	3	6	10	30.0	286.5	252351.1	3815688.3
	13	8.329	29.6	0.40	5YR	7	6	15	105.0	288.2	252361.6	3815693.6
	14	8.647	27.0	0.50	5YR	7	4	15	105.0	287.9	252361.8	3815689.2
	15	7.732	27.3	0.40	5YR	7	4	15	105.0	287.3	252361.6	3815687.0
	16	8.201	25.2	0.35	5YR	5	1	15	75.0	290.6	252374.6	3815699.2
	17	7.404	22.8	0.40	5YR	5	1	15	75.0	290.9	252374.4	3815700.8
	18	8.186	32.6	0.60	5YR	3	1	15	45.0	290.8	252373.1	3815701.4
	19	7.343	27.0	0.40	5YR	6	4	15	90.0	285.9	252347.7	3815684.7

	20	7.725	27.0	0.40	5YR	7	4	15	105.0	284.7	252334.1	3815685.3
Site 22	1	9.839	31.8	0.50	5YR	4	4	15	60.0	248.7	252399.6	3816004.4
	2	9.409	29.6	0.60	5Y	6	1	25	150.0	248.7	252399.0	3816004.5
	3	7.824	26.2	0.60	5Y	5	4	25	125.0	248.8	252398.9	3816002.2
	4	7.437	33.4	0.45	5YR	7	1	15	105.0	248.8	252398.8	3816000.8
	5	8.642	26.3	0.70	5YR	5	4	15	75.0	248.4	252398.4	3815998.8
	6	8.452	31.2	0.55	5YR	6	6	15	90.0	248.3	252395.3	3816004.8
	7	7.815	32.1	0.55	5Y	6	1	25	150.0	248.2	252395.6	3816000.4
	8	8.008	28.1	0.65	5YR	6	2	15	90.0	247.9	252393.9	3816000.6
	9	8.379	28.1	0.55	5Y	6	2	25	150.0	247.4	252392.8	3815998.9
	10	8.026	32.3	0.65	5Y	6	1	25	150.0	246.7	252389.6	3815999.4
	11	8.020	36.1	0.60	5Y	5	1	25	125.0	247.2	252390.8	3816000.0
	12	9.045	38.5	0.50	5YR	5	4	15	75.0	247.9	252392.9	3816004.0
	13	8.292	31.9	0.60	5Y	4	1	25	100.0	247.7	252391.0	3816007.1
	14	7.366	35.5	0.55	5YR	5	4	15	75.0	247.4	252388.1	3816004.1
	15	8.105	34.3	0.50	5Y	5	1	25	125.0	246.8	252381.4	3816005.8
Site 23	1	8.565	30.0	0.60	5YR	6	6	15	90.0	98.7	250940.6	3814072.4
	2	8.685	27.9	0.55	5YR	6	6	15	90.0	98.6	250942.6	3814065.1
	3	8.712	28.7	0.50	5YR	6	6	15	90.0	98.5	250942.3	3814064.0
	4	8.081	41.0	0.60	5YR	5	6	15	75.0	104.0	250780.7	3814227.3
	5	8.130	45.2	0.50	5YR	5	6	15	75.0	97.2	250818.9	3814104.4
Site 24	1	9.290	31.1	0.65	5YR	6	6	15	90.0	234.5	251720.2	3815887.4
	2	8.330	34.6	0.70	5YR	6	6	15	90.0	238.3	251695.2	3815902.9
	3	9.170	27.6	0.60	10R	6	6	10	60.0	239.9	251715.5	3815919.1
	4	8.880	37.3	0.70	5YR	5	6	15	75.0	228.8	251749.0	3815903.2
	5	9.840	27.3	0.50	5YR	5	6	15	75.0	238.3	251737.8	3815933.3
	6	9.930	38.1	0.50	10R	5	6	10	50.0	223.8	251744.1	3815874.8
	7	9.390	15.8	0.55	7.5YR	6	6	17.5	105.0	235.9	251731.2	3815911.2
	8	9.270	29.8	0.50	7.5YR	5	6	17.5	87.5	231.6	251749.0	3815920.6
	9	8.520	34.2	0.60	10R	5	6	10	50.0	237.3	251717.3	3815902.9
	10	8.000	29.1	0.65	7.5YR	6	6	17.5	105.0	238.3	251738.6	3815887.8
	11	8.910	33.2	0.65	5YR	6	6	15	90.0	240.2	251726.3	3815929.3
	12	9.320	26.5	0.50	10R	4	8	10	40.0	234.3	251727.6	3815901.3
	13	9.920	29.8	0.60	10R	5	6	10	50.0	230.9	251739.6	3815900.2
	14	9.170	43.6	0.75	5YR	6	6	15	90.0	237.0	251737.6	3815926.2
Site 25	1	9.478	23.4	0.40	5YR	6	6	15	90.0	68.6	250940.1	3813561.7
	2	9.085	23.2	0.45	5YR	7	3	15	105.0	68.4	250941.2	3813560.9
	3	9.523	24.0	0.50	5YR	6	3	15	90.0	69.4	250943.3	3813568.0
	4	8.999	32.9	0.40	10R	5	3	10	50.0	69.3	250945.2	3813568.4
	5	9.319	35.6	0.50	5YR	5	6	15	75.0	69.1	250944.4	3813566.5
	6	9.486	31.8	0.45	10R	6	3	10	60.0	69.4	250957.2	3813571.0
Site 26	1	11.110	32.7	0.50	5YR	6	8	15	90.0	312.5	252773.2	3815722.2

	2	9.872	24.2	0.60	10R	5	4	10	50.0	312.1	252771.8	3815720.4
	3	9.130	24.0	0.50	5YR	6	4	15	90.0	313.4	252768.5	3815729.4
	4	8.643	15.2	0.40	10YR	4	4	20	80.0	312.7	252793.6	3815720.8
	5	9.174	26.2	0.60	10R	5	4	10	50.0	312.8	252793.1	3815720.9
	6	9.707	20.1	0.50	10R	4	4	10	40.0	313.8	252812.0	3815724.5
	7	9.714	23.0	0.60	10YR	7	6	20	140.0	316.5	252821.2	3815738.0
	8	8.540	24.0	0.50	5YR	5	6	15	75.0	315.8	252825.0	3815735.5
	9	8.483	22.2	0.60	10R	4	4	10	40.0	315.8	252829.0	3815736.4
	10	9.024	24.1	0.70	10R	4	4	10	40.0	318.1	252838.6	3815759.7
	11	9.718	24.4	0.50	10YR	6	4	20	120.0	319.1	252834.8	3815764.9
	12	8.848	17.2	0.40	10YR	6	4	20	120.0	319.3	252836.2	3815769.7
	13	9.143	28.0	0.60	10YR	6	6	20	120.0	320.4	252831.2	3815773.5
	14	9.512	24.6	0.60	10YR	4	3	20	80.0	319.4	252840.2	3815777.1
	15	9.630	23.4	0.50	10R	3	3	10	30.0	321.2	252843.5	3815797.6
	16	9.236	25.0	0.50	10YR	7	6	20	140.0	322.4	252842.3	3815805.0
Site 27	1	9.020	25.3	0.55	5Y	5	3	25	125.0	132.7	248722.8	3815612.7
	2	9.324	29.9	0.50	5YR	5	6	15	75.0	132.9	248718.4	3815610.6
	3	9.268	20.5	0.50	5YR	4	4	15	60.0	132.4	248719.5	3815609.0
	4	8.940	25.3	0.60	7.5YR	6	6	17.5	105.0	131.6	248725.8	3815609.6
	5	9.215	19.1	0.65	7.5YR	5	6	17.5	87.5	129.7	248722.4	3815598.6
	6	9.511	22.9	0.55	5YR	5	6	15	75.0	126.0	248719.3	3815578.8
	7	9.388	29.2	0.65	10R	5	2	10	50.0	128.9	248704.6	3815587.4
	8	9.636	22.1	0.60	5Y	7	4	25	175.0	128.8	248706.3	3815587.5
	9	8.870	27.9	0.55	5YR	6	3	15	90.0	128.4	248710.7	3815584.9
	10	10.300	29.1	0.55	5YR	6	6	15	90.0	132.0	248681.8	3815605.6
Site 28	1	11.283	20.6	0.45	10R	4	3	10	40.0	249.9	252494.1	3815355.5
	2	10.843	25.2	0.55	10R	4	3	10	40.0	250.0	252491.3	3815355.1
	3	10.503	26.1	0.60	10R	5	2	10	50.0	249.7	252488.7	3815353.5
	4	10.193	26.1	0.55	10R	5	2	10	50.0	248.4	252492.4	3815347.3
	5	9.991	25.1	0.55	10R	3	2	10	30.0	248.4	252489.4	3815346.5
	6	9.603	28.3	0.60	10R	4	2	10	40.0	248.0	252497.0	3815346.3
	7	10.030	19.5	0.55	5YR	5	3	15	75.0	247.9	252500.8	3815345.8
	8	9.800	26.6	0.50	10YR	7	6	20	140.0	249.2	252498.7	3815353.0
	9	9.802	26.1	0.55	5YR	7	3	15	105.0	250.0	252503.6	3815356.8
	10	9.710	32.7	0.60	5YR	6	3	15	90.0	249.6	252506.5	3815355.0
	11	10.526	25.2	0.50	10R	3	2	10	30.0	250.1	252510.4	3815358.7
	12	9.622	30.7	0.55	5YR	5	6	15	75.0	250.8	252504.1	3815360.3
	13	10.917	25.8	0.50	10R	5	6	10	50.0	253.1	252497.4	3815372.5
	14	9.925	27.0	0.40	5YR	7	6	15	105.0	254.1	252493.7	3815377.6
	15	9.694	33.5	0.50	5YR	6	4	15	90.0	255.4	252501.0	3815381.7
	16	9.653	26.9	0.50	5YR	5	3	15	75.0	254.0	252464.6	3815371.3
	17	10.543	24.5	0.50	10YR	4	1	20	80.0	254.8	252461.2	3815375.2

	18	10.374	26.9	0.55	10R	4	2	10	40.0	254.8	252451.8	3815380.1
	19	10.274	29.5	0.45	10R	6	4	10	60.0	250.6	252454.2	3815349.7
	20	10.469	30.8	0.60	10R	6	4	10	60.0	249.7	252447.8	3815347.1
Site 29	1	11.032		0.40	10R	6	4	10	60.0	186.6	251583.7	3814507.6
	2	10.556		0.40	10R	6	4	10	60.0	193.1	251601.0	3814529.7
	3	9.989		0.40	10R	6	2	10	60.0	193.9	251602.4	3814532.9
	4	10.064		0.50	5YR	7	6	15	105.0	196.9	251615.6	3814539.2
	5	10.979		0.45	5YR	7	3	15	105.0	206.7	251609.2	3814577.7
	6	10.503		0.55	5YR	7	2	15	105.0	206.3	251612.4	3814575.2
	7	10.589		0.45	10YR	7	3	20	140.0	205.7	251614.4	3814572.5
	8	10.506		0.40	5YR	7	6	15	105.0	204.9	251617.5	3814569.4
	9	10.183		0.45	10YR	7	4	20	140.0	208.0	251624.2	3814574.9
	10	10.588		0.55	5YR	7	2	15	105.0	208.6	251620.1	3814577.9
	11	11.606		0.40	5YR	7	2	15	105.0	209.8	251611.1	3814584.9
	12	11.252		0.50	10YR	5	4	20	100.0	190.0	251537.3	3814555.6
	13	10.719		0.50	10R	6	2	10	60.0	190.3	251532.9	3814560.2
	14	10.735		0.40	10R	6	2	10	60.0	192.1	251534.9	3814568.4
	15	10.202		0.55	10R	6	2	10	60.0	191.8	251527.1	3814572.8
	16	10.265		0.50	5YR	7	4	15	105.0	191.9	251524.4	3814575.4
	17	10.580		0.55	5YR	7	4	15	105.0	195.7	251543.7	3814578.0
	18	11.192		0.45	10R	6	2	10	60.0	199.6	251542.8	3814601.2
	19	11.096		0.40	5YR	7	4	15	105.0	195.9	251549.7	3814572.9
	20	10.879		0.50	10R	5	3	10	50.0	196.3	251561.7	3814570.4
Site 30	1	12.430		0.50	10R	5	6	10	50.0	138.9	251410.9	3814070.0
	2	11.344		0.60	10R	5	4	10	50.0	139.6	251418.6	3814070.0
	3	11.223		0.45	10R	4	4	10	40.0	138.7	251420.5	3814064.4
	4	9.956		0.60	10R	5	3	10	50.0	139.5	251425.2	3814068.3
	5	10.055		0.50	10R	3	3	10	30.0	138.5	251424.8	3814062.4
	6	10.579		0.55	5YR	7	6	15	105.0	140.5	251440.0	3814073.1
	7	10.317		0.55	5YR	6	4	15	90.0	141.7	251520.8	3814069.0
	8	11.045		0.55	10R	5	4	10	50.0	141.6	251532.3	3814070.7
	9	9.579		0.60	10R	5	3	10	50.0	141.5	251543.0	3814071.3
	10	10.274		0.50	10R	6	3	10	60.0	134.8	251569.0	3814040.4
	11	11.125		0.55	5Y	2.5	2	25	62.5	127.4	251355.9	3814014.4
	12	11.094		0.55	5Y	7	3	25	175.0	128.0	251367.4	3814018.4
	13	10.579		0.50	10R	2.5	1	10	25.0	129.4	251375.4	3814017.5
	14	11.063		0.60	10YR	6	6	20	120.0	130.0	251378.4	3814019.3